THE FATES OF BINARY COMPANIONS IN TYPE IA SUPERNOVAE WITHIN THE SINGLE-DEGENERATE SCENARIO

BY

KUO-CHUAN PAN

DISSERTATION

Submitted in partial fulfillment of the requirements
for the degree of Doctor of Philosophy in Astronomy
in the Graduate College of the
University of Illinois at Urbana-Champaign, 2013

Urbana, Illinois

Doctoral Committee:

Associate Professor Paul M. Ricker, Chair
Professor Emeritus Ronald E. Taam
Professor Emeritus Ronald F. Webbink
Professor You-Hua Chu
Professor Charles F. Gammie
Associate Professor Susan A. Lamb

Abstract

Type Ia supernovae (SNe Ia) are thought to be caused by thermonuclear explosions of carbon-oxygen white dwarfs in close binary systems. However, the nature of the progenitor systems is still uncertain. In the single-degenerate scenario (SDS), the companion star is non-degenerate and can be significantly affected by the explosion. We explore this interaction by means of multi-dimensional adaptive mesh refinement simulations using the FLASH code. We consider several different companion types, including main-sequence-like stars, red giants, and helium stars. In addition, we include the symmetry-breaking effects of orbital motion, rotation of the non-degenerate star, and Roche-lobe overflow.

We find that the relationship between the unbound stellar mass and the initial binary separation can be fitted by a power law. The power-law index is found to be about -3.5 to -3.7 for the main-sequence star, -2.9 to -3.4 for the helium star, and -4.0 to -4.2 for the red giant. After the explosion, the companion receives a kick from the supernova ejecta. It is found that the kick velocity is also related to the binary separation by a power law, except for the red giant companion, due to the large numerical uncertainty created by the small kick in this case. The power-law index is found to be about -1.7 to -1.9 for the main-sequence star and -2.6 to -2.8 for the helium star. By using tracer particles in FLASH, the process leading to the unbinding of matter can be determined by analyzing the fluid elements in a time sequence. It is found that the process is dominated by ablation, which has usually been neglected in past analytical studies. The level of Ni/Fe contamination of the companion that results from the passage of the supernova ejecta is found to be $\sim 10^{-5} M_{\odot}$ for the main-sequence star, $\sim 10^{-4} M_{\odot}$ for the He star, and $\sim 10^{-8} M_{\odot}$ for the red giant, suggesting that the ratio of nickel/iron to hydrogen plus helium abundance in the remnant should be found to be larger than the solar ratio if the contamination is mixed only in the companion's envelope. A hole in the ejecta shadowed by the companion star is also found in the simulation, which is a possible source of the variation in SN Ia light curves. The spinning main-sequence companion star loses about 48% of its initial angular momentum during the impact, causing the rotational velocity to drop to 23% of the original rotational velocity.

One way to distinguish between the single- and double-degenerate scenarios is to search for the post-

impact remnant star expected in the SDS. We explore the evolution of the post-impact remnants in our simulations for main sequence-like and helium-rich star binary companions using the stellar evolution code MESA. Our results show that the energy deposited in a main sequence companion's outer layers by the SN causes the outermost $\sim 5\%$ of the star to expand on the local thermal timescale ($\sim 300 - 1000$ yr), making the star brighten to $\sim 10 - 100 L_{\odot}$. In most cases the effective temperature also increases significantly. As this excess energy is radiated away, the outer layers slowly recollapse. The time evolution is sensitive not only to the amount of SN energy deposited but also the depth to which it penetrates. For Tycho G, the proposed remnant of Tycho's SN, we find that main sequence companions can match the observed effective temperature and rotation speed (assuming conservation of specific angular momentum post-impact), but they are typically $\sim 2\times$ too bright.

We have also examined helium star models for both normal SNe Ia and the newly classified subluminous "Type Iax" SNe and find that these cases follow very different Hertzsprung-Russell (H-R) diagram tracks than do main sequence models. Helium star companions brighten to $\sim 10^4 L_{\odot}$ within a decade, becoming hot blue subdwarfs (sdOs) and contracting over $> 10^6$ yr to become helium red giants. Because helium star companions start in more compact systems, their kick velocities and rotation speeds can be much higher than for main sequence companions.

Our results show that, given the age of a supernova remnant, we can test the plausibility of candidate observed remnant companions, and based on such comparisons we can draw conclusions about the nature of the companions, if the SDS is valid. Moreover, the luminosity enhancements due to SN impact can be sufficient to make remnant companion stars detectable in the Magellanic Clouds or other nearby galaxies with distances $\lesssim 4$ Mpc.

To Mom and Dad,

for their love, support, and encouragement

Acknowledgments

This project would not have been possible without the support of many people.

First and foremost, I would like to express my sincere gratitude to my advisor Professor Paul Ricker for his kindness, patience, encouragement and guidance. It was he who pointed me toward this interesting research area and guided me to complete this project. I would also like to thank my collaborator Professor Ronald Taam. He is like my second advisor. He has inspired me tremendously, not only in this project, but also with his way of doing research. I cannot thank him enough.

Many thanks to the members of my committee— Professor Ronald Webbink, Professor You-Hua Chu, Professor Charles Gammie, and Professor Susan Lamb — for their service and insight. Also many thanks to Professors Paul Ricker, Ronald Taam, and Ronald Webbink for writing so many recommendation letters for me. Thanks to Professor You-Hua Chu for taking care of my life in Champaign. She always has endless tasty snacks in her office and feeds poor graduate students like me.

I would also like to thank my undergraduate advisor, Professor Chi Yuan, when I was a research assistant in the Academia Sinica Institute of Astronomy and Astrophysics (ASIAA) in Taiwan. It was because of him that I started to work on astrophysical fluid dynamics, and it was because of him that I decided to pursue my life in computational astrophysics. At the end of 2006, while I was applying to graduate schools, a tumor was found in his brain. At that tough time, he still worried about my graduate school applications and wrote me recommendation letters in the hospital. Without him, I would not have had the chance to study at the University of Illinois.

Thanks very much to my friends in the UIUC Astronomy Department, including (in no particular order) Hotaka Shiokawa, Katherine Lee, Nachiketa Chakraborty, David Rebolledo Lara, Yiran Wang, Yu-Ting Wu, Karen Yang, Amy Lien, Hsin-Fang Chiang, Nick Hakobian, Ian Stephens and Gary Foreman, without whose support and brainstorming, I could not have finished this project.

Many thanks to my friends at UIUC, including Po-Yao Chang, Chia-Ling Hsu, Gazzy Weng, Wen-Pin Hsieh, Ching-Kai Chiu, Kuei Sun, Mao-Chuang Yeh, Po-Chao Wen, Kai-Pin Liao, Ray Liu, Yu-Ying Lee, Ting-Yin Lin, Hsuan-Ju Wang, Shen-Fu Tsai, Chih-Ting Kuo, Yu-Jen Hsu, and Chih-Wei Chang, for giving

me such a great, unforgettable memory of life in Champaign. I would also like to thank all my old friends who are studying at other universities in the US or in Taiwan for their encouragement, especially for Yi-Hsin Chiu, Hsin-Hua Lai, Cheng-Chien Chen, Yu Liu, Jing-Wu Dong, Yi-Hsin Chen, Chiao-Yu Tseng, Pei-Chun Hsu, Chien-Yu Lien, and Eola Don. And last, but not least, to my beloved parents, Hui-Jen Chien and Ching-Tsai Pan, and my brother Kuo-Chen Pan, for always encouraging me to purse my interests and always keeping my life interesting.

Thanks to the UIUC Astronomy Department and all the staff here, for providing me such a great environment to do research. Thanks for the support by the Computational Science and Engineering (CSE) Fellowship at the University of Illinois at Urbana-Champaign and the support through my advisor Professor Paul Ricker and collaborator Professor Ronald Taam: the NSF XSEDE Ranger system at the Texas Advanced Computing Center under allocation TG-AST040034N and NSF grant AST-0703950. The major simulation code used in this project is FLASH, which was developed largely by the DOE-supported ASC/Alliances Center for Astrophysical Thermonuclear Flashes at the University of Chicago. Part of the analysis of FLASH data was completed using the analysis toolkit `yt`.

Table of Contents

List of Tables

List of Figures

List of Abbreviations

AGB	Asymptotic giant branch
AMR	Adaptive mesh refinement
CO	Carbon-oxygen
DDS	Double-degenerate scenario
DTD	Delay time distribution
EOS	Equation of state
HVS	Hypervelocity star
HST	Hubble Space Telescope
Ia SNR	Type Ia supernova remnant
IMF	Initial mass function
LMC	Large Magellanic Cloud
MLT	Mixing-length theory
MS	Main sequence
PIRS	Post-impact remnant star
RLOF	Roche-lobe overflow
RG	Red giant
SDS	Single-degenerate scenario
sdB	subdwarf-B star
sdO	subdwarf-O star
SFH	Star formation history
SMC	Small Magellanic Cloud
SN	Supernova
SN Ia	Type Ia supernova
SNR	Supernova remnant
WD	White dwarf
ZAMS	Zero-age-main-sequence

List of Symbols

a	Radiation constant
c	Speed of light
G	Gravitational constant
k_B	Boltzmann constant
$L_\odot$	Solar luminosity
$M_\odot$	Solar mass
$M_{\rm ch}$	Chandrasekhar mass
N_A	Avogadro constant
$\sigma_{\rm SB}$	Stefan-Boltzmann constant

Chapter 1

Introduction

In this Chapter, I briefly summarize the history, general observational properties, and theoretical models of Type Ia supernovae (SNe Ia) based on reviews written by Filippenko (1997), Branch (1998), Hillebrandt & Niemeyer (2000), Wang & Han (2012), and Hillebrandt et al. (2013). The structure and outline of this dissertation are also described in the last section of this Chapter.

1.1 A brief history

The term *nova* means "new" in Latin, referring to a suddenly appearing "new star" in the sky, also known as a "guest star" in ancient China, since it fades away and disappears after a few weeks. The earliest historical record of these new stars was recorded in 352 BC by Chinese astronomers (Hellemans & Bunch, 1991). Many similar events have been recorded by different civilizations and countries over the past two thousand years.

"Super"-novae (SNe) are distinguished from novae because of their higher intrinsic brightness (Baade & Zwicky, 1934), and the fact that SNe could be associated with collapsed massive stars (Zwicky, 1938). Spectrograms of SNe were rare before 1930-1940, but the discovered SNe showed similar peak luminosities and post-maximum spectra, suggesting that SNe could be used as distance indicators (Wilson, 1939; Zwicky, 1939). By 1940, it became more clear that there are at least two distinctly different classes of SNe, which could be classified by the absence (Type I) or presence (Type II) of hydrogen Balmer lines near maximum light (Minkowski, 1941). However, what causes the difference between these two types was not clear at that time.

Hoyle & Fowler (1960) were the first to point out that nucleosynthesis through the r-process in degenerate stars may accompany thermonuclear explosions which could be the origin of Type I (more specifically, Type Ia; Wheeler & Harkness, 1990) SNe. Later on, Truran et al. (1967) found that the light curves of SNe Ia could be powered by the nuclear radioactive decay of nickel (^{56}Ni$\rightarrow^{56}$Co$\rightarrow^{56}$Fe). The combination of these two ideas became the basic scenario for Type Ia SNe and is still the dominant explanation.

A phenomenological relation between the absolute magnitudes of SNe Ia at maximum light and their

B-band decline rate $\Delta m_{15}(B)$ (the magnitude change from its B-band maximum to 15 days later) was discovered by Phillips (1993) and is known as the "Phillips relation". Subsequently, several updated methods have been adopted to improve the normalized peak magnitude, including a "stretch parameter" (Perlmutter et al., 1997) and a multi-parameter fit (Riess et al., 1996). With this correlation, SNe Ia can be treated as "standardizable" candles and are important as cosmological distance probes, helping to determine the values of key cosmological parameters and expansion rate of the Universe (Perlmutter et al., 1999; Riess et al., 1998; Schmidt et al., 1998). The discovery using SNe Ia of the accelerating expansion of the Universe was recognized with the Nobel Prize in Physics in 2011 to Saul Perlmutter, Adam Riess, and Brian Schmidt. However, cosmological applications using SNe Ia are based on the assumption that the homogeneity of low-redshift ($z < 0.15$) SNe Ia applies to high-redshift SNe Ia. This assumption is questionable until we fully understand the nature of the progenitors of SNe Ia.

1.2 Observations

1.2.1 General properties

SNe are among the most catastrophic and energetic events in the Universe. They are luminous stellar explosions whose peak luminosities can be as high as those of their host galaxies ($\sim 10^{42}$ to 10^{43} erg s^{-1}). Spectroscopically, SNe Ia lack H and He absorption lines in their spectra, but they show strong absorption at 615 nm produced by the blue-shifted Si II 635.5 nm line (Wheeler & Harkness, 1990). In general, the luminosity of a SN Ia rises to maximum within about two to three weeks, reaching

$$M_{\rm B} \sim M_{\rm V} \sim -19.30 \pm 0.03 + 5\log(H_0/60) \tag{1.1}$$

with a dispersion of $\sigma_M \lesssim 0.3$ (Hamuy et al., 1996), where H_0 (in units of km s^{-1} Mpc^{-1}) is the Hubble constant. After the maximum light, a rapid decline of about three magnitude per month occurs.

The broad and blueshifted Si lines of SNe Ia originate from the ejecta expanding in high velocities. It has been proposed that the spectral diversity or velocity evolution of the ejecta may originate in asymmetric explosions (Maeda et al., 2010; Maund et al., 2010). In addition to the Phillips relation, correlations between SN Ia ejecta speed, light curve shapes, and host galaxy properties have also been found (Branch, 1998). For example, SNe Ia in early-type galaxies show slower ejecta speeds and faster-declining light curves and are dimmer by ~ 0.2 to 0.3 mag than SNe Ia in late-type star-forming galaxies. Furthermore, the SN Ia rate per unit stellar mass is ~ 20 times higher in late-type galaxies than in early-type ones. However, no redshift

dependence of spectral evolution has been found so far, since high-redshift SNe Ia are difficult to explore spectroscopically.

1.2.2 Peculiar type Ia supernovae

The Philips relation, the correlation of peak luminosity with the decline time scale, can be formulated with at least one parameter, such as $\Delta m_{15}(B)$ or a stretch parameter. From the theoretical point of view, this parameter is associated with the explosion strength, or more specifically, the total mass of ^{56}Ni that is produced during a thermonuclear SN explosion. A weaker explosion is less luminous, is redder, and has a faster declining light curve and slower ejecta speed. This analytical expression is known as the "Arnett's rule" (Arnett, 1982). A typical mass of ^{56}Ni produced in SN Ia ejecta is about $0.3 - 0.9 M_{\odot}$. However, there are at least $\sim 15\%$ of SNe Ia that violate the Philips relation and the Arnett's rule. For instance, SN 1991bg, SN 1992K, SN 1991T, SN 1999by, and SN 2002cx are well-studied peculiar SNe Ia. These peculiar SNe Ia are sub-luminous or over-luminous at maximum light and have unusual ejecta speeds comparing to the "Branch-normal" SNe Ia. Li et al. (2011b) suggest the fraction represented by these peculiar SNe Ia could be as high as $\sim 30\%$. It is still unclear whether these peculiar SNe Ia are due to different explosion mechanisms or different progenitor systems as compared with normal SNe Ia.

SN 1991bg-like SNe Ia

SN 1991bg-like SNe Ia are sub-luminous SNe Ia with peak luminosities about one magnitude fainter than normal SNe Ia. Their V, I, and R-band light curves show an unusually fast decline rate. Furthermore, the total mass of ^{56}Ni produced in their ejecta is also unusually low ($\lesssim 0.1 M_{\odot}$). In contract to normal SNe Ia, some evidence of unburnt C and O has been found in their early spectra. This subclass of SNe Ia contributes about 15% (or more) of all SNe Ia (Li et al., 2011b).

SN 2002cx-like SNe Ia

Another subclass of sub-luminous SNe Ia, SN 2002cx-like SNe Ia, has been recently proposed by Foley et al. (2012a). These are also called Type Iax supernovae (SNe Iax). There are currently 25 members in this subclass, and they could contribute about 5% of all SNe Ia. SNe Iax show maximum-light velocities in the range $2,000 \lesssim v \lesssim 7,000$ km s^{-1} and lower peak magnitudes in the range $-14.2 \gtrsim M_V \gtrsim -18.9$ mag. The peak luminosity and decline timescale of SNe Iax are also correlated, but with a larger scatter than for normal SNe Ia. It is also found that most SNe Iax are observed in late-type galaxies, favoring short delay-time populations. (The delay time is the interval between a star's arrival on the zero-age main sequence

(MS) and its destruction in an SN Ia.) Surprisingly, two SNe in this subclass, SN 2007J and SN 2004cs, show strong He I lines, suggesting that there must be some helium in this subclass (Foley et al., 2012a).

SN 1991T-like SNe Ia

In contrast to sub-luminous SNe Ia, SN 1991T-like SNe Ia show strong, energetic, and broad light curves, and they are a subclass of over-luminous SNe Ia. Unlike normal SNe Ia, which show Si II and Ca II lines, their early spectra display high-excitation lines of Fe III, but they go back to normal after roughly a few months. Although they are brighter than normal SNe Ia, their ejecta velocities are lower than those of normal SNe Ia. The estimated mass of ^{56}Ni in this subclass is about $1.5 - 1.8 M_{\odot}$, which is higher than the Chandrasekhar mass, suggesting a scenario different from other subclasses of SNe Ia. At the current time, there are about 7 members in this subclass, and they may contribute up to $\sim 9\%$ of all SNe Ia (Li et al., 2011b).

1.3 Explosion models

1.3.1 Observational constraints

Based on the above discussed observational constraints, the explosion mechanisms of SNe Ia have to satisfy several requirements: First, they need to explain the homogeneity of normal SNe Ia but also need to have intrinsic variations that can produce peculiar SNe Ia. (However, some intrinsic variation can be achieved by having different progenitor channels.) Second, the ejecta compositions and velocities need to agree with observed spectra and light curves: the explosions need to produce enough ^{56}Ni and enough high-velocity intermediate mass elements in the outer layers. Third, the progenitor systems and explosion mechanisms need to be consistent with the observed delay-time distribution (DTD) and SN Ia rates.

1.3.2 Chandrasekhar mass explosion models

Thermonuclear explosions of CO WDs with masses close to a particular mass threshold, the Chandrasekhar mass ($M_{\rm ch} \sim 1.4 M_{\odot}$), have good agreement with the observed light curves and spectra, and their nucleosynthesis yields enough nickel to explain normal SNe Ia (Hoyle & Fowler, 1960). In addition, the fixed mass threshold naturally explains the homogeneity of SNe Ia. However, there is still not a consensus whether the ignition is supersonic (detonation), subsonic (deflagration) explosion, or some complicated combination (e.g. with some deflagration-detonation transition).

One of the most popular Chandrasekhar-mass models is the W7 model described by Nomoto et al. (1984), which corresponds to a carbon deflagration in an accreting CO WD. The initial carbon deflagration is assumed to develop in the central regions of the WD and is then followed by a detonation. This one-dimensional model provides a good fit to observed light curves.

1.3.3 Sub-Chandrasekhar mass models

Another explosion model that has recently received attention is the sub-Chandrasekhar mass model. In this scenario, the CO WD never reaches the Chandrasekhar mass before the explosion and might have an accumulated layer of helium (Iben et al., 1987). It is likely that the accumulated helium shell first detonates under the right physical conditions and then triggers a second detonation in the sub-Chandrasekhar mass WD, leading to a "double-detonation" SN Ia.

1.3.4 Super-Chandrasekhar mass models

Recent observations show that the progenitor of some exploding CO WDs might have super-Chandrasekhar mass (Howell et al., 2006). This scenario is possible if the CO WD were rapidly rotating before the SN explosion, making the critical mass ($\lesssim 2.8 M_{\odot}$) above the Chandrasekhar mass and leading to an over-luminous SN Ia. This situation could be achieved if the progenitor system were a close binary system. Depending on the progenitor system and the mass range of exploding WDs, the WD could explode immediately due to a secular instability if the WD mass exceeds $2.4 M_{\odot}$, or it may require some spinning-down time to ignite carbon (Hachisu et al., 2012).

1.4 Progenitor systems

Since a single CO WD is unconditionally stable, the CO WD have to interact with another star to produce a SN Ia explosion. It is therefore most likely that SNe Ia were produced in binary systems. Most works on progenitor models for SNe Ia have focused on two general scenarios: the single-degenerate scenario (SDS) and the double-degenerate scenario (DDS). Each scenario contains several different kinds of channels to produce SNe Ia. It is nevertheless unclear which progenitor channel(s) dominate(s). Based on current observational constraints, it is likely that multiple progenitor channels contribute SNe Ia.

1.4.1 Single-degenerate scenario

The single-degenerate scenario (SDS) involves a CO WD accreting matter from a non-degenerate stellar companion, eventually becoming unstable to explosive nuclear burning (Whelan & Iben, 1973; Nomoto, 1982). The non-degenerate companion could be a main-sequence (MS) star, a red giant (RGs), or a helium-rich star (He). However, single-degenerate models require that the rate of mass accretion be such that the WD avoid a nova explosion. For a high accumulation efficiency, stable burning on the WD is required, but this burning phase occurs in a fairly narrow range above 10^{-7} $M_{\odot}$ yr^{-1}. For rates greater than this range, a wind from the WD develops that limits the accretion efficiency (Nomoto, 1982; Hachisu et al., 1996; Ivanova & Taam, 2004), making it difficult to explain the observed low-redshift SN Ia rate of 3×10^{-5} Mpc^{-3} yr^{-1} (Mannucci et al., 2005) using single-degenerate progenitors alone. Furthermore, these non-degenerate companions are usually hydrogen- or helium-rich. The observational upper limit of stripped hydrogen after SN impact is $< 0.01 M_{\odot}$ (Leonard, 2007; Shappee et al., 2013b). Thus, the absence of the hydrogen that should appear in SN Ia spectra poses a problem for the SDS.

1.4.2 Double-degenerate scenario

On the other hand, the double-degenerate scenario involves the merger of two CO WDs whose orbital decay results from the loss of angular momentum due to gravitational wave emission (Iben & Tutukov, 1984; Webbink, 1984):

$$t_{\rm GW}({\rm yr}) = 8 \times 10^{7}({\rm yr}) \times \frac{(M_1 + M_2)^{1/3}}{M_1 M_2} P^{8/3}({\rm h}), \tag{1.2}$$

where $t_{\rm GW}$ is the merging time, P is the orbital period, and M_1 and M_2 are masses of WDs.

With the DDS, the lack of hydrogen spectral lines is easy to explain; however, the homogeneity of the explosion energy is difficult to account for since the total mass of the binary system varies from case to case. Furthermore, it is more likely that massive WD-WD mergers lead to the production of an ONeMg WD followed by accretion-induced collapse to a neutron star (Nomoto & Iben, 1985; Ivanova & Taam, 2004; Dessart et al., 2006; Wickramasinghe et al., 2009). Moreover, the wide range of total WD masses suggests that double-degenerate models should exhibit much more heterogeneity than is observed in SN Ia light curves (Goldhaber et al., 2001; Knop et al., 2003).

1.5 Outline

In this dissertation, the work is concentrated on the SN impact and post-impact evolution of non-degenerate companions in SNe Ia within the SDS via multi-dimensional hydrodynamics simulations and stellar evolution simulations. With this study, we can place better constraints on the SDS and potentially identify some progenitor systems of nearby SNe Ia remnants (Ia SNRs).

Chapter 2 and 3 provide a comprehensive study of the impact of SNe Ia ejecta on binary companions in the SDS. In the SDS, the companion star is non-degenerate and can be significantly affected by the explosion. We explore this interaction by means of multi-dimensional adaptive mesh refinement simulations using the FLASH code. In Chapter 2, we focus on the helium-rich companions (the He-WD channel) with two-dimensional simulations. Chapter 3 extends the study to three-dimension and considers more different SDS channels, including the MS-WD, RG-WD, and He-WD channels. In addition, the simulations included the symmetry-breaking effects of orbital motion, rotation of the non-degenerate star, and Roche-lobe overflow.

It is found that non-degenerate companions in the SDS should survive the SN impact and should be detectable. Chapter 4 presents a sophisticated scheme to combine multi-dimensional hydrodynamics simulations with one-dimensional stellar evolution simulations. We explore the evolution of the post-impact remnants in the MS-WD channel using the stellar evolution code MESA. We also examine the viability of the candidate star Tycho G as the possible remnant companion in Tycho's supernova by comparing it to the evolved post-impact remnant stars in our simulations.

In Chapter 5, we extend the study on post-impact evolution to helium-rich binary companions. We predict that a blue subdwarf-like (sdO-like) star should be detectable in the central regions of Ia SNRs within star-forming regions, if the SN Ia progenitors evolved via the helium-star channel in the SDS. These He-reich post-impact remnant stars are predicted to be rapidly rotating and to have high spatial velocities. Furthermore, we also point out additional sources of single sdO stars and/or hypervelocity stars.

Finally, in Chapter 6, we describe some possible candidates of post-impact remnant stars (PIRSs) in Ia SNRs in the Galaxy and the Magellanic Clouds, and discuss the possibility of searching PIRSs in nearby galaxies.

Chapter 2

Impact of Type Ia Supernova Ejecta on Helium-Star Binary Companions[†]

Abstract

The impact of Type Ia supernova ejecta on a helium-star companion is investigated via high-resolution, two-dimensional hydrodynamic simulations. For a range of helium-star models and initial binary separations it is found that the mass becoming unbound in the interaction, $\delta M_{\rm ub}$, is related to the initial binary separation, a, by a power law of the form $\delta M_{\rm ub} \propto a^m$. This power-law index is found to vary from -3.1 to -4.0, depending on the mass of the helium star. The small range of this index brackets values found previously for hydrogen-rich companions, suggesting that the dependence of the unbound mass on orbital separation is not strongly sensitive to the nature of the binary companion. The kick velocity is also related to the initial binary separation by a power law with an index in a range from -2.7 to -3.3, but the power-law index differs from those found in previous studies for hydrogen-rich companions. The space motion of the companion after the supernova explosion is dominated by its orbital velocity in the pre-supernova binary system. The level of Ni/Fe contamination of the companion resulting from the passage of the supernova ejecta is difficult to estimate, but an upper limit on the mass of bound nickel is found to be $\sim 5 \times 10^{-4}\ M_\odot$.

2.1 Introduction

Type Ia supernovae (SNe Ia) are among the most catastrophic and energetic events in the Universe. Because they are so luminous, and because their light-curve shapes and absolute magnitudes are correlated, SNe Ia can be used as "standardizable candles" in measuring the distances to remote galaxies, allowing constraints to be placed on key cosmological parameters (Branch & Tammann, 1992; Riess, 1996). SNe Ia also play a major role in galactic chemical evolution via their energy and metal input to the interstellar medium.

[†] Published as Kuo-Chuan Pan, Paul Ricker, and Ronald Taam 2010, ApJ, 715, 78

Thus, the nature of their progenitor systems and the physical origin of variations in their properties are fundamental problems of great interest (Domínguez et al., 2001; Howell et al., 2007).

Most work on progenitor models for SNe Ia has focused on two general classes of systems. The single-degenerate scenario involves a CO white dwarf (WD) accreting matter from a non-compact stellar binary companion, eventually becoming unstable to explosive nuclear burning (Whelan & Iben, 1973; Nomoto, 1982). On the other hand, the double-degenerate scenario involves the merger of two CO WDs whose orbital decay results from the loss of angular momentum due to gravitational wave emission (Iben & Tutukov, 1984; Webbink, 1984).

Single-degenerate models require that the rate of mass accretion be such that the WD avoid a nova explosion. For a high accumulation efficiency, stable burning on the WD is required, but this burning phase occurs in a fairly narrow range above $10^{-7}\ M_{\odot}\ \mathrm{yr}^{-1}$. For rates greater than this range, a wind from the WD develops that limits the accretion efficiency (Nomoto, 1982; Hachisu et al., 1996; Ivanova & Taam, 2004), making it difficult to explain the observed low-redshift SN Ia rate of $3 \times 10^{-5}\ \mathrm{Mpc}^{-3}\ \mathrm{yr}^{-1}$ (Mannucci, 2005) using single-degenerate progenitors alone. Although the predicted and observed numbers of double-degenerate systems are sufficient to explain the observed rate (Nelemans et al., 2001; Napiwotzki et al., 2001, 2002), it is more likely that massive WD-WD mergers lead to the production of an ONeMg WD followed by accretion-induced collapse to a neutron star (Nomoto & Iben, 1985; Ivanova & Taam, 2004; Dessart et al., 2006; Wickramasinghe et al., 2009). Moreover, the wide range of total WD masses suggests that double-degenerate models should exhibit much more heterogeneity than is observed in SN Ia light curves (Goldhaber et al., 2001; Knop et al., 2003).

Maoz (2008) analyzed the observed SN Ia rate for assumed initial mass functions (IMF) and concluded that almost all intermediate-mass close binary systems in the range $3-8\ M_{\odot}$ should evolve to the SN Ia stage. This result allows for a wide range of possibilities for SN Ia progenitor systems. Furthermore, observations of the SN Ia rate as a function of redshift suggest the need for a two-component model for the delay time distribution (DTD). (The delay time is the interval between a star's arrival on the zero-age main sequence and its destruction in an SN Ia.) Scannapieco & Bildsten (2005) and Mannucci et al. (2006) found that the observations can be fit with a short-delay-time population having delays of $\sim 10^8$ yr and a long-delay-time population having delays of $3 - 4$ Gyr.

To provide an explanation for the two populations suggested by the observed SN Ia rate, several pre-supernova progenitor models have been investigated. The long-delay-time population can be understood in terms of progenitor systems characterized by a main-sequence-like companion in the MS-WD channel (Hachisu et al., 2008b) and/or by a red giant in the RG-WD channel (Hachisu et al., 1996; Hachisu et al.,

1999; Hachisu et al., 1999; Hachisu et al., 2008a). In contrast, the short-delay-time population may consist of systems characterized by a massive MS star in the MS-WD channel or by a He star in the He-WD channel (Waldman et al., 2008; Wang et al., 2009; Wang et al., 2009; Wang & Han, 2009; Meng & Yang, 2010).

Numerically, Marietta et al. (2000) explored the influence of the supernova explosion on the companion star in the single-degenerate channel with hydrogen-rich stars consisting of red giants, subgiants, and main-sequence stars using two-dimensional Eulerian hydrodynamics simulations. They found that significant quantities of hydrogen would be unbound from the companion star in each case (15% of the envelope for main-sequence and subgiant cases, and 98% of the red giant envelope), in conflict with observational upper limits on the amount of hydrogen inferred from SN Ia spectra (Mattila et al., 2005; Leonard, 2007).

A more recent hydrodynamical study by Pakmor et al. (2008) reexamined the main-sequence simulation of Mattila et al. (2005) using a three-dimensional smoothed particle hydrodynamics (SPH) simulation. In contrast to Marietta et al., Pakmor et al. adopted the structure for the companion star based on the binary evolutionary models of Ivanova & Taam (2004), which yielded more compact main-sequence-like companions. As a consequence, Pakmor et al. found a tenfold reduction in the amount of unbound mass compared with Marietta et al., bringing the prediction of the amount of unbound hydrogen-rich material into agreement with the observational upper limits.

In a complementary analytical study, Kasen (2010) investigated the radiation emitted by the collision of SN Ia ejecta with a red giant, finding that the light curve should depend on the viewing angle. This result was attributed to the fact that the gas is more transparent in the region shadowed by the companion star. This suggests the possibility that the secondary star may be detectable in future observational studies.

These previous simulations of the effect of a supernova impact on a companion star have been carried out only for models applicable to the long-delay-time population of SN Ia. In contrast, Wang et al. (2009) suggest a progenitor binary model based upon a helium-star channel for the short-delay-time population. Using a binary evolution model, for this channel they find a SN Ia birthrate $\sim 3 \times 10^{-4}$ yr^{-1} and a corresponding delay time of $\sim 4.5 \times 10^{7}$ yr to $\sim 1.4 \times 10^{8}$ yr (Wang et al., 2009). The latter delay time is consistent with that estimated from observations for the short-delay-time population by Scannapieco & Bildsten (2005), Mannucci et al. (2006), and Aubourg et al. (2008).

In this paper we report the results of Eulerian hydrodynamics simulations of the impact of SN Ia ejecta on companion stars for the single-degenerate helium-star channel. In the next section, the assumptions underlying our study, the construction of the initial model, and the numerical method are described. Our numerical results for a range of helium-star models and orbital separations are reported in § 3 and their implications are discussed in § 4. In the final section, we summarize our results and make some concluding

Table 2.1: Helium-star models.

	Mass	Radius	Evolution time	$m_{ub}^{\dagger}$	$C_{ub}^{\dagger}$	$m_{kick}^{\ddagger}$	$C_{kick}^{\ddagger}$
He-WDa	0.697	0.63	9.2×10^6	-4.01	1.42	-3.28	4150
He-WDb	0.803	1.10	5.2×10^5	-3.13	0.70	-2.90	2413
He-WDc	1.007	1.35	2.2×10^5	-3.48	1.17	-3.18	2703
He-WDd	1.206	1.63	6.1×10^4	-3.51	1.35	-2.71	1729

† The entries for the power-law index, m_{ub}, and power-law constant, C_{ub}, refer to the power-law fit to unbound mass versus orbital separation described in eq. 2.1.

‡ The entries for the power-law index, m_{kick}, and power-law constant, C_{kick}, refer to the power-law fit to kick velocity versus orbital separation described in eq. 2.2.

remarks.

2.2 Numerical methods and models

2.2.1 Numerical codes

For our hydrodynamical simulations we used FLASH version 3 (Fryxell et al., 2000; Dubey et al., 2008). FLASH is a parallel, multi-dimensional hydrodynamics code based on block-structured adaptive mesh refinement (AMR). To solve the Euler equations on the AMR grid, we used the piecewise parabolic method (Colella & Woodward, 1984) with modifications to handle nonideal equations of state (Colella & Glaz, 1985). The equation of state used is interpolated from a precomputed table of the Helmholtz free energy. It includes contributions from radiation, completely ionized nuclei, and degenerate electrons and positrons (Timmes & Swesty, 2000) for an optically thick mixture of gas and radiation in local thermodynamic equilibrium.

The helium-star models used in our simulations were generated using a one-dimensional stellar evolution code (Eggleton, 1971, 1972, 1973). We simulated four helium-star models with initial masses equal to 1.25, 1.35, 1.4, and 1.8 $M_{\odot}$. To evolve the helium-star models to the onset of the supernova explosion, an artificial constant mass loss rate was adopted such that the evolution time and final helium star masses were consistent with the detailed binary evolutionary models of Wang et al. (2009). The resulting models are summarized in Table 2.1. The density profiles of the helium-star models at the onset of the supernova explosion are illustrated in Figure 2.1. It can be seen that the more massive models are characterized by larger radii and less compact cores.

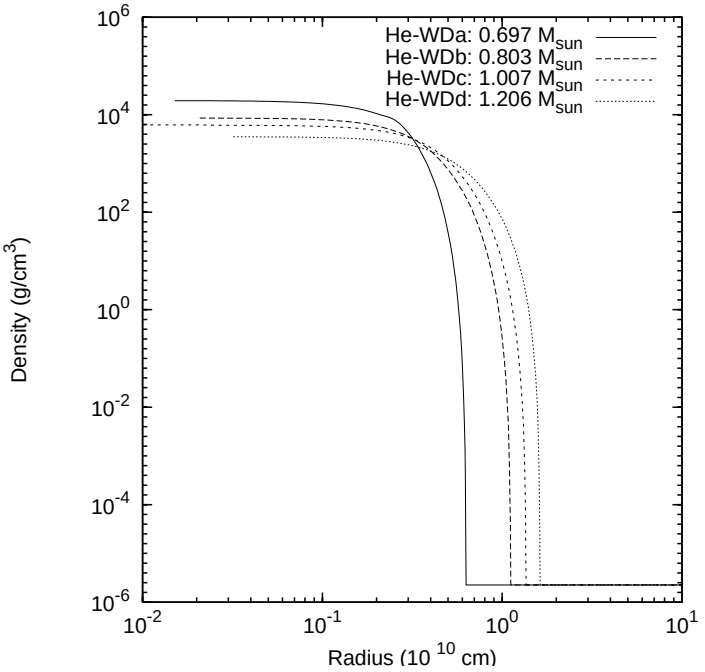

Figure 2.1: Density profiles of the helium-star models at the onset of the supernova explosion, as obtained using the one-dimensional stellar evolution code.

2.2.2 Initial setup

Since the speed of the ejecta in a SN Ia ($\lesssim 10^4$ km s^{-1}) is much higher than the orbital speed of the helium star ($\lesssim 10^3$ km s^{-1}) in a binary system, we ignore the orbital motion in the first approximation and consider a 2D axisymmetric geometry. The simulation domain is described using cylindrical coordinates (r, z), with the z-axis defined as the direction along the line connecting the centers of the white dwarf and the helium star. We consider a simulation domain with a size equal to fifteen times the radius of the helium star ($R_{\rm He}$) in the radial direction and 30 $R_{\rm He}$ in the axial direction. For convenience, the helium star is located at the origin of the coordinate grid.

To simplify the problem, the composition of the one-dimensional helium-star model was taken to be a uniform distribution of 98% helium and 2% carbon by mass when used in FLASH. This simplification leads to an error of $\lesssim 2\%$ in the composition and $\lesssim 4\%$ in the radius for the lowest-mass helium-star model. To initialize the two-dimensional FLASH simulations, we first interpolated the one-dimensional model onto the FLASH grid using up to twelve levels of refinement based on the magnitudes of the second derivatives of gas density and pressure. With each block containing 8×16 zones, the equivalent uniform-grid resolution is thus $16,384 \times 32,768$. For model He-WDc, the minimum zone spacing at this level of refinement corresponds to 1.22×10^7 cm. Within the helium star, a minimum of nine levels of refinement was used (corresponding

to a maximum zone spacing of 9.76×10^7 cm for model He-WDc). Because the surface of the helium star is characterized by a very steep density gradient, we established a sharp cutoff radius to avoid pressure errors at the surface. The cutoff radius was chosen such that each density drop of one order of magnitude is resolved by at least three zones in the surface region (we have more than 40 zones per order of magnitude in the core region). Outside the cutoff radius, the density was set to an ambient value of 2.25×10^{-6} g cm^{-3}, and the pressure was set to the value of the helium-star model pressure profile at the cutoff radius. The simulations, therefore, employed the same ambient density but somewhat different ambient pressures. The composition of the ambient gas in each case was taken to be pure hydrogen, in order to distinguish with composition between ambient gas with the companion gas.

The helium-star model was relaxed on the Eulerian grid by artificially damping the momentum for a period of time greater than about thirty times the average dynamical time scale. During this time the damping factor was smoothly increased from 0.7 to 0.99, ensuring that the Mach number in the helium-star interior was always smaller than 0.01. Once this process was complete, the damping was removed and the gas velocity was reset to zero. The supernova explosion was then introduced to the grid. During the subsequent evolution, we allowed second-derivative refinement up to seven levels everywhere except in two regions: within the helium star at any time, and in a region surrounding the supernova explosion for the first 150 seconds, we required nine levels of refinement (equivalent to a resolution of 2048×4096 for a uniform grid with a minimum zone spacing of 9.77×10^7 cm in model He-WDc). The extra refinement for the supernova region reduces the influence of grid artifacts on the developing explosion. The explosion itself was introduced by creating a spherical region of high-density and high-temperature gas with radius equal to twenty times the minimum zone spacing at nine levels of refinement. Each run used this "7/9" refinement pattern except for one model that was also run at 6/8, 8/10, 9/11, and 10/12 to study convergence (see § 2.3.3).

The Type Ia supernova model used is the W7 model described by Nomoto et al. (1984), which corresponds to a carbon deflagration in an accreting CO WD. The initial carbon deflagration is assumed to develop in the central regions of the white dwarf and is then followed by a detonation. This one-dimensional model provides a good fit to observed light curves and can be approximated by a white dwarf of mass $M_{\rm wd} = 1.378\ M_\odot$, total explosion energy $E_{\rm sn} = 1.233 \times 10^{51}$ erg, and average speed $v_{\rm sn} = 8.527 \times 10^3$ km s^{-1}. This mass is uniformly distributed within the spherical perturbation used to start the calculation. The velocity inside the perturbation is taken to be radially outward and uniform in magnitude; the internal energy is set using $v_{\rm sn}$ and $E_{\rm sn}$. We assume the ejecta to be entirely ^{56}Ni and use this fluid component as a tracer for the ejecta. The mass of the supernova ejecta creates a potential perturbation that changes the equilibrium state of the helium star. However, in all of our models the radius of the helium star is smaller than or equal to the Roche

lobe radius, and the timescale on which the equilibrium is upset by the supernova shock, $\sim a/v_{\rm sn}$ (a is the initial binary separation), is shorter than the average dynamical timescale in the helium star. Thus we expect that the altered pre-supernova potential should not have a significant effect on the structure of our models. However, because the orbital motion is ignored in this study, the gravitational force from the supernova material will attract the helium star and cause a small velocity perturbation toward the supernova material. This velocity perturbation can be comparable to the kick velocity of the helium star after supernova impact but is much smaller than the ejecta speed.

2.3 Results

In this section, we describe the numerical results for the standard case, model He-WDc, and explore the dependence of the system's evolution on the mass of the helium-star companion and the initial binary orbital separation a. To determine the sensitivity of the results to the numerical resolution, we also describe a convergence test.

2.3.1 Qualitative description of evolution

Immediately after the onset of the supernova explosion, a double shock structure is formed as the ejecta interact with the surrounding medium (label A in Figure 2.2; the figure illustrates the evolution of a simulation with initial binary separation of 4×10^{10} cm, $\sim 3\ R_{\rm He}$, and 9/11 levels of refinement). A forward shock expands outward into the ambient medium, and a reverse shock propagates inward (in Lagrangian coordinates). The two shocks are separated by a contact discontinuity (Dwarkadas & Chevalier, 1998). During this free expansion phase, the swept-up ambient medium has very little effect, except for the development of an instability at the contact discontinuity. This instability is unimportant in affecting the helium star, as it is seeded by a numerical grid effect and is Rayleigh-Taylor unstable (label A) (Dwarkadas, 2000). The expansion of the ejecta leaves behind an extremely low-density region at the center of the supernova (label a) that is prone to numerical grid effects which become visible due to the color scale; these are smoothed out later by the reflected shock (label C). The SN ejecta reach the companion at $t \sim a/v_{\rm sn} \sim 50$ seconds, at which time a bow shock forms at the leading surface of the companion, making an angle of $\sim 40^\circ$ with respect to the z-axis. This can be seen in the upper-left panel of Figure 2.2 (label B)[1]. As the bow shock propagates further, the shearing of gas in conjunction with the action of gravity due to the helium star causes distortions in the bow shock structure. After the impact of the ejecta on the helium star, ejecta material

[1]Movies are available at
`http://sipapu.astro.illinois.edu/foswiki/bin/view/Main/BinarySupernovae`

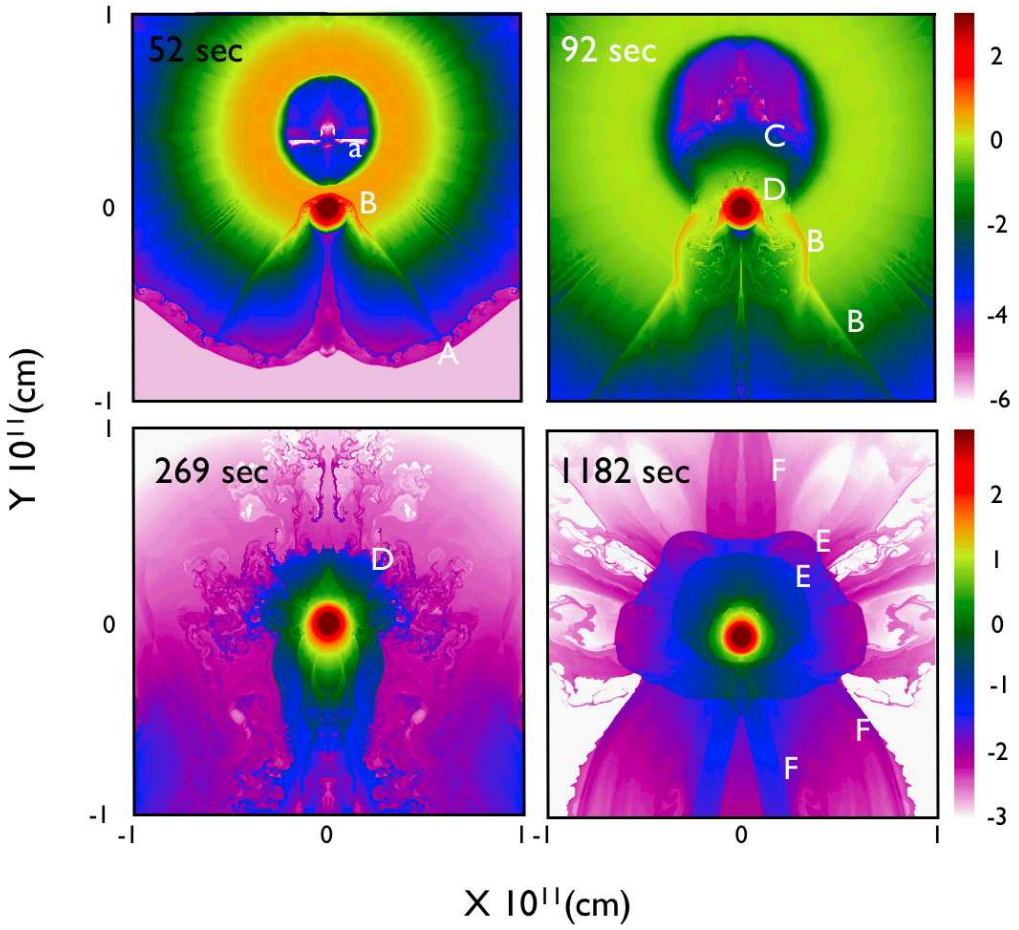

Figure 2.2: The density distribution for model He-WDc (see Table 2.1) with initial binary separation of 4×10^{10} cm. Each frame shows a portion of the domain spanning 10^{11} cm. Letters refer to features described in the text. The color scale indicates the logarithm of the gas density in g cm^{-3}.

begins to reflect and refill the central supernova region (label C in Figure 2.2). As a result of the mixing beginning at ~ 100 seconds associated with the Kelvin-Helmholtz and Rayleigh-Taylor instabilities in the envelope of the helium star (label D in Figure 2.2), the bow shock breaks up and is divided into a curved shock and a straight shock that makes an angle of $\sim 40^\circ$ with the z-axis (label B in the upper-right panel of Figure 2.2). The instabilities continue to develop between ~ 100 s and ~ 600 s as the mixing region moves away from the helium-star envelope (lower-left panel of Figure 2.2). At around 100 s, the shock propagates to the center of the helium star, leading to the pulsation of the helium star. Smooth shocks (label E in Figure 2.2) are continually generated by the oscillation of the helium star after ~ 600 s. Radial shocks (label F in Figure 2.2), which result from the interaction of shocks on the rear side of the helium star, sweep around the helium star (lower-right panel of Figure 2.2). As the helium star evolves further, its density profile becomes smoother, approaching a new equilibrium state. Qualitatively, our results are similar to results reported by Marietta et al. (2000) and Pakmor et al. (2008) for the main-sequence case, but with a more compact companion and smaller binary separation. As a result of the asymmetric interaction, a small kick velocity, $v_{\rm kick} \sim 85$ km s^{-1}, is imparted to the helium star.

2.3.2 Parameter survey

We conducted a parameter survey to explore the dependence of the numerical results on the binary progenitor's properties. Note that Wang et al. (2009) determined the orbital period, and thus the orbital separation, at the onset of the supernova explosion, for each choice of helium star and white dwarf. In our study we do not follow the binary evolution up to the explosion, so the Roche-lobe radii of Wang et al.'s models are actually larger than the radii of our helium-star models. Therefore, in addition to varying the mass of the helium star, we also vary the binary separation in order to determine the effect of this parameter.

Figure 2.3 shows the typical time evolution of the amount of mass removed from the helium star (defined as total unbound helium mass) by the SN ejecta. The first peak occurs at the initial impact (~ 30 s), but then some gas becomes bound again after the ejecta pass through the helium star. At $\sim 80 - 100$ seconds, a second peak develops which is associated with the effect of the reverse shock. Lastly, a third peak at ~ 500 seconds occurs when the compressed helium star relaxes and starts to oscillate. After 1,500 seconds, the amount of unbound mass reaches an approximately steady value. The final unbound mass is thus calculated for a given initial binary separation and helium-star model by averaging the unbound mass values computed for several time steps at this late stage.

Figures 2.4 and 2.5 show the final unbound mass and helium-star kick velocity (defined as the center-of-mass velocity of the final bound helium) as functions of the binary separation in our simulations. We include

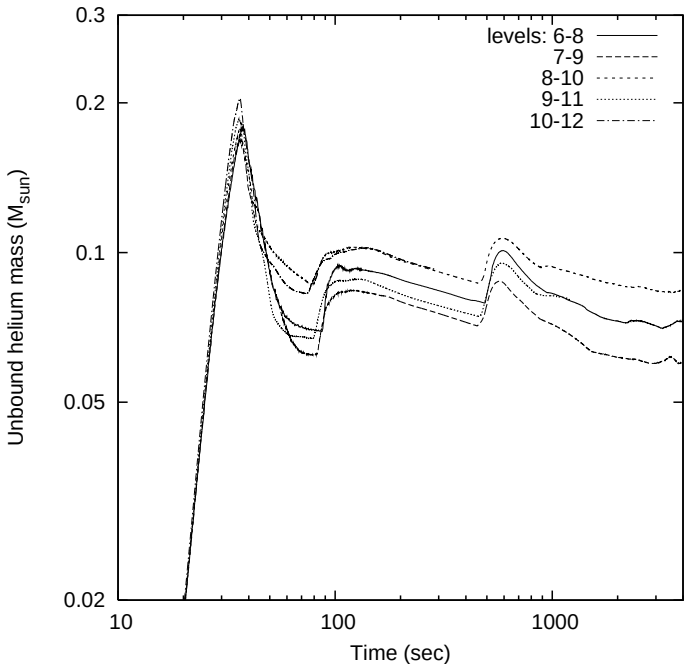

Figure 2.3: Unbound helium mass versus simulation time using different levels of refinement for the He-WDc model (see Table 2.1) with initial separation 3×10^{10} cm. (Note: the 10/12 run was very expensive and was carried out only up to 292 s.)

14% error bars in Figure 2.4 and Figure 2.5 based on the results of our convergence test (§ 2.3.3). We find that the unbound mass can be fit by the relation

$$\delta M_{\rm ub} = C_{\rm ub} a^{m_{\rm ub}} \ M_\odot \ , \tag{2.1}$$

where a is the orbital separation, $m_{\rm ub}$ is the power-law index, and the constant $C_{\rm ub}$ depends only on the helium-star model (see Table 2.1). For comparison, we also plot the power-law relation with index -3.49 found by Pakmor et al. (2008) and the data from Marietta et al. (2000) for main-sequence companions (consistent with an index of -3.14). The power-law indices for our helium-star companions vary in a small range and bracket their results, suggesting that the index may be insensitive to the evolutionary state of the companion. The normalization of the above relation does appear to be sensitive to the nature of the companion star.

The kick velocity of the helium star is calculated by differencing the center-of-mass positions in the z-direction at different timesteps. Alternatively, it can be determined by dividing the total bound helium star momentum by the total bound helium star mass. Both methods yield the same kick velocity. To smooth out short-term fluctuations, we average the center-of-mass positions for every ten steps, then determine the

kick velocity by numerical differentiation of these averaged values. The helium star is initially accelerated by the SN ejecta with an acceleration $\sim GM_{\rm wd}/a^2$ for a time $\sim a/v_{\rm sn}$, and then it is kicked by the SN ejecta during the initial impact. During the initial impact, the kick velocity varies dramatically. However, after $\sim 1,000$ seconds, these variations decay. Thus, we define the kick velocity by using the difference between the final averaged velocity and the maximum velocity just before the impact of the SN ejecta (the exact time range to average the final velocity varies from run to run and covers the entire period of "smooth" variation in the kick velocity). Figure 2.5 shows the kick velocity for the different helium-star models and initial binary separations. For initial binary separations larger than 4 $R_{\rm He}$ the kick velocity could not be adequately determined, because the perturbed velocity from the SN is larger than the kick velocity at larger separations. As obtained by Pakmor et al. (2008) and Meng et al. (2007), a power-law relation is also found in our simulation and can be fitted by the relation

$$v_{\rm kick} = C_{\rm kick} a^{m_{\rm kick}}, \tag{2.2}$$

where $v_{\rm kick}$ is the kick velocity, $m_{\rm kick}$ is the power-law index, and the constant $C_{\rm kick}$ depends only on the helium-star model (see Table 2.1). However, unlike the situation for the final unbound mass, the slope is very different from that found in the case of main-sequence companions ($m_{\rm kick} = -1.45$ in Pakmor et al. (2008), and $m_{\rm kick} = -1.26$ in Marietta et al. (2000)) (see §4.1).

2.3.3 Convergence test

In order to determine the robustness of our numerical results, we performed a convergence test for model He-WDc. We carried out simulations with the same initial binary separation ($a = 3 \times 10^{10}$ cm) but several different maximum AMR levels, computing the amount of unbound mass in each run as a function of time. The unbound mass is found by calculating the difference between the initial helium-star mass and the measured total bound helium mass at each step. The total bound helium mass is the sum of the helium masses in all zones for which the total energy is negative. The results, which are plotted in Figure 2.3, show that the final unbound mass lies in the range between the 8/10 and 10/12 runs. The unbound mass is sensitive to the level of turbulence that occurs near the surface of the helium star, particularly for resolutions higher than 8/10 (see Fig. 2.6), so rather than observing normal convergence behavior, we find that the unbound mass for runs with different resolutions fluctuates within a small range of values. Similar behavior is also found with other initial binary separations. Thus, the difference in unbound helium mass between the 8/10 and 9/11 calculations ($\sim 0.01\ M_\odot$) is used to estimate a relative error. Because the unbound helium mass

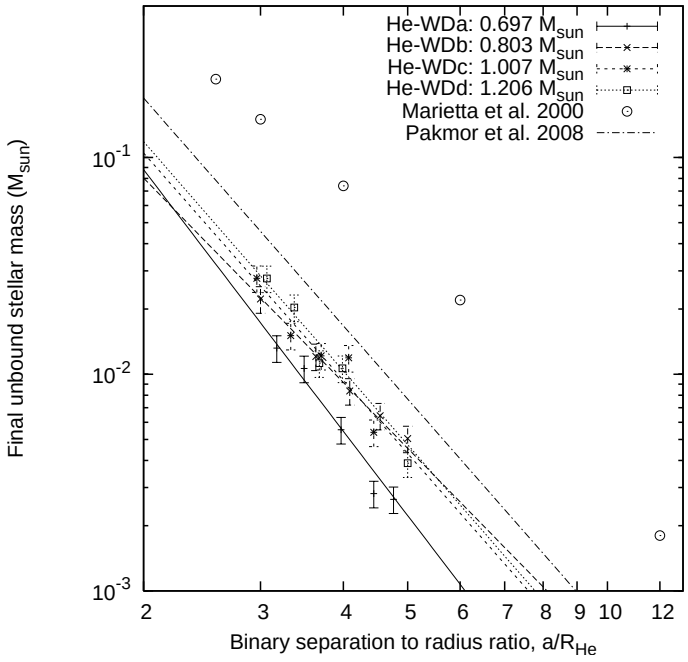

Figure 2.4: Final unbound stellar mass versus binary separation for different helium-star models. The separation is expressed in units of the helium-star radius. The lines show power-law relations from numerical simulations for different helium-star models (Table 2.1). Error bars are based on the 14% error determined in our convergence test. The dash-dot line is the fitted curve provided by Pakmor et al. (2008) and the circles are the data from Marietta et al. (2000).

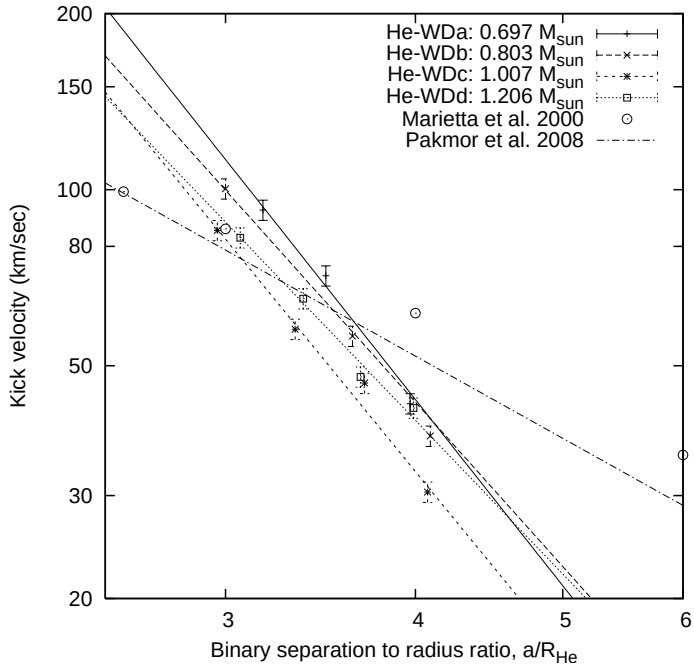

Figure 2.5: Similar to Figure 2.4 but for kick velocity versus binary separation for different helium-star models. Error bars are based on the 4% error determined in our convergence test.

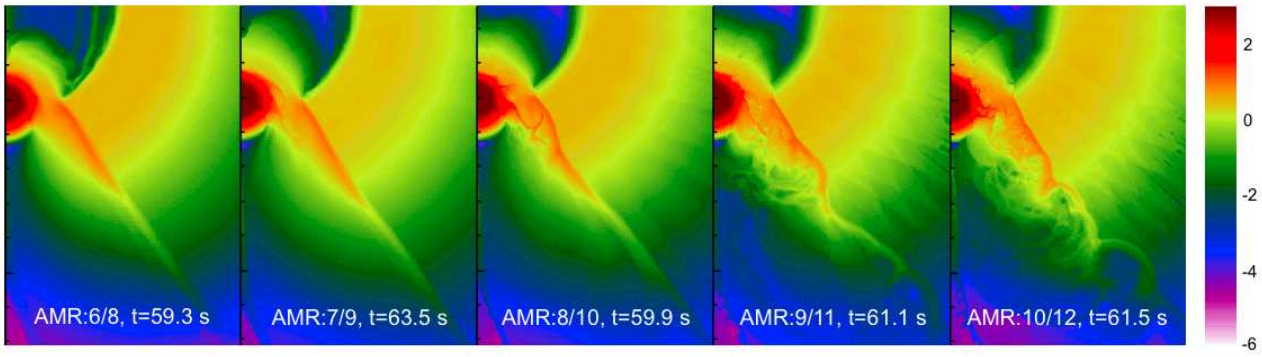

Figure 2.6: The density distribution for model He-WDc with initial binary separation 3×10^{10} cm. Each frame shows the evolution time at around one minute for different AMR levels. The color scale indicates the logarithm of the gas density in g cm^{-3}.

reaches an approximately steady value at late times, this difference suggests an estimate of about $\pm 14\%$ for the relative error in our runs, since it is not clear whether the 7/9 run is always the lower limit of unbound mass for different models or different separations. Similar analysis gives a $\pm 4\%$ relative error in kick velocity. To allow for a feasible parameter study, a resolution of 7/9 levels was chosen for the whole suite of twenty runs.

2.4 Discussion

2.4.1 Stripped and ablated mass

The impact of SN Ia ejecta on a helium-star companion is not as dramatic as for a main-sequence or red-giant companion like those considered by Marietta et al. (2000) because helium-star companions are more compact. This can be seen in Figure 2.7, which shows the gas pressure profile along the z-axis at several different times during the evolution of model He-WDc with an initial binary separation of 4×10^{10} cm. While the pressure immediately behind the ejecta shock front is initially $\sim 10^{21}$ dyne cm^{-2}, by the time the front reaches the helium star it has dropped to $\sim 10^{13}$ dyne cm^{-2}. The shock is considerably weakened by the time it reaches the deep interior of the star. As a result, the amount of unbound mass is much lower than in the case for main-sequence companions for a given ratio of separation to radius, $a/R \sim 3$, even though the helium-star channel is characterized by smaller binary separations.

If we assume that the WD accretion and subsequent explosion in our models are driven by Roche lobe overflow (RLOF), the physically appropriate initial binary separations for models a to d should be 3.11, 3.00, 2.84, and 2.72 times $R_{\rm He}$. The total unbound helium masses for these models at these radii (Figure 2.4) are $\sim 1-3\%$ of the initial helium-star masses, which is consistent with the suggested upper limit of $\sim 0.01\ M_\odot$

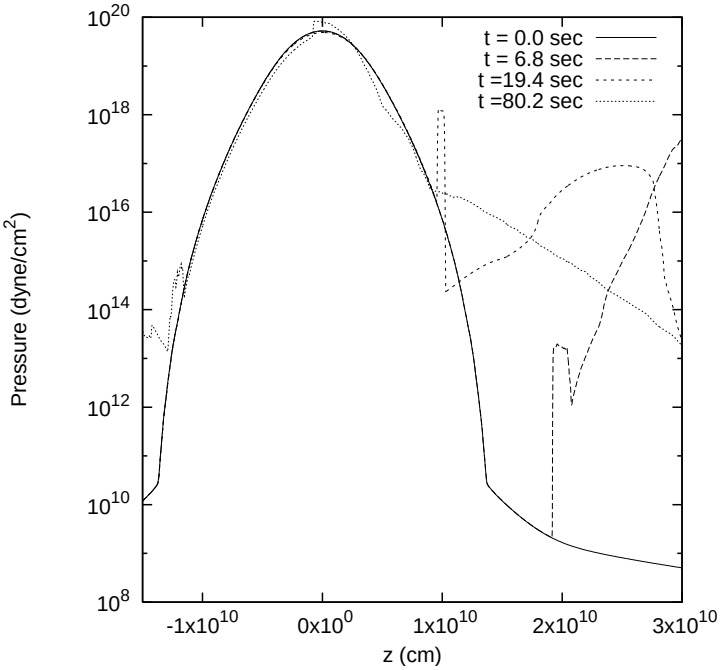

Figure 2.7: Pressure profile along the z-axis at different times for model He-WDc with an initial binary separation of 4×10^{10} cm and 9/11 levels of refinement. The solid line is the original pressure profile before the SN explosion.

determined by Leonard (2007) from observations.

The unbinding of mass from the helium star results either from ablation (heating) or from stripping (momentum transfer) by the ejecta. To estimate the relative contribution of these processes, we examined the mixing of nickel in the helium-star material. Because stripping involves the physical displacement of gas from the helium star by the ejecta, this process is associated with the contact discontinuity between the two fluids. This discontinuity is unstable, and the resulting instabilities lead to mixing, which while numerical in origin, nevertheless signals contact between the nickel-rich ejecta and helium-rich stellar envelope. In contrast, ablation proceeds through the shock heating of envelope material ahead of the contact discontinuity, and because the shock is more stable, much less mixing is expected where ablation is dominant. The averaged ablated and stripped mass after the initial impact for the different cases studied is shown in Figure 2.8.

We find that the ablated mass is comparable to the stripped mass for smaller binary separations, and the amount ablated is sensitive to the binary separation during the initial phase (less than 100 seconds for the case of model He-WDc). The final results suggest that in most cases the amount of stripped mass can be as much as an order of magnitude greater than the ablated mass, depending on the binary separation. The ratio cannot be determined accurately because we did not trace individual fluid elements in these simulations.

A simple analytical method has been used by Meng et al. (2007) to estimate the amount of unbound

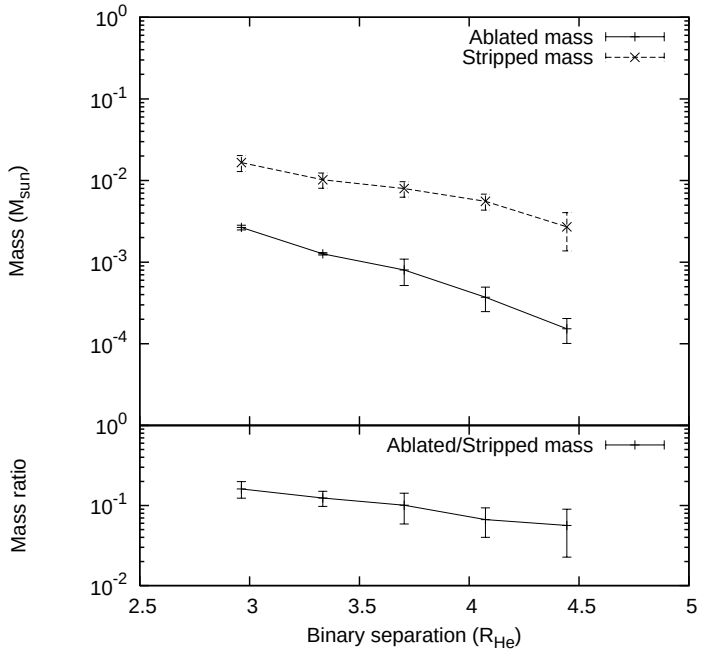

Figure 2.8: Comparison of averaged ablated and stripped helium mass after the initial supernova impact versus the binary separation for model He-WDc (upper panel). Error bars represent the standard deviation during the average time range. The lower panel shows the ratio of ablated to stripped helium mass.

matter based on conservation of momentum, ignoring the shock dynamics and the effect of ablation. This method yields a shallower power-law slope (-1.9) for unbound mass versus separation than the range that we observe (-3.1 to -4). However, the power-law slopes for unbound mass and kick velocity versus separation found by Meng et al. (2007) are similar to the slopes inferred from the hydrogen-rich stars studied by Marietta et al. (2000). Although the method adopted by Meng et al. (2007) is oversimplified, their result suggests that ablation in main-sequence binary companions may not be as important as for helium-star binary companions. Figure 2.8 shows that in our simulations the ablated mass corresponds to $\sim 1 - 20\%$ of the total unbound mass, with a greater fraction ablated for smaller orbital separations. Thus, the total momentum imparted to the helium star results from contributions by both direct impact of the SN ejecta and shock heating, whereas for hydrogen-rich companions the former effect is a more important contributor than the latter. The difference in the relative contribution of these two effects for different types of companion star may explain the difference in the power-law indices for kick velocity.

2.4.2 Nickel contamination

The companion star can be contaminated by the mixing of supernova ejecta with the helium-rich material in its envelope, perhaps resulting in a detectable enhanced iron abundance after the nickel radioactively decays. Since ^{56}Ni is used as a tracer in our model, we have determined the amount of nickel bound to the

remnant helium star. In general, there is a tendency for a higher level of contamination for more massive helium-star companions or for larger orbital separations. In the former case, a massive companion presents a larger cross section for capture of supernova ejecta, whereas in the latter case, the ram pressure from the ejecta is lower for larger binary separations, resulting in a reduction of the amount of contaminated matter that is stripped off. However, the level of contamination in our simulations is highly dependent on the development of small-scale fluid instabilities at multifluid interfaces. Although we find little evidence for a simple relationship between the amount of contamination and the nature of the helium-star companion or the orbital separation, we can estimate an upper limit on the nickel captured by the helium-rich companion by identifying the ejecta which cannot escape the gravitational potential. This limit is $\sim 5 \times 10^{-4}\ M_{\odot}$, somewhat smaller than the estimate by Marietta et al. ($\sim 1.5 \times 10^{-3}\ M_{\odot}$). If the mixing of nickel is only restricted to the envelope, the nickel to helium ratio can be estimated by using the upper limit of nickel contamination and the final envelope mass. We define the core mass for the initial helium-star models by finding the radius at which the second derivative of the density with respect to radius is a maximum; the envelope mass is then the total mass less the core mass. Using this definition, we find that the unbound helium-star material is taken entirely from the envelope. The final envelope mass can thus be obtained from the difference between the initial envelope mass and the final unbound mass in Figure 2.4 at the separation corresponding to RLOF. We find that the ratio of the upper limit on bound nickel mass to the final envelope helium mass is $\sim 9 - 50 \times 10^{-4}$ for the different helium-star models. This value is substantially higher than the solar ratio of iron abundance to that of hydrogen plus helium (5.1×10^{-4}) found by Anders & Grevesse (1989), suggesting that the abundance of nickel/iron in the remnant helium-star atmosphere should be enhanced relative to normal Population I stars if surface convection is not an important factor.

2.4.3 Detecting the remnant companion star

After the supernova, the companion star moves with a velocity $\vec{v} \sim \vec{v}_{\rm orb} + \vec{v}_{\rm kick}$. The orbital speeds corresponding to the range of binary separations in our simulations are $v_{\rm orb} \sim 350 - 800$ km s^{-1}, while the kick speed $v_{\rm kick} \sim 30 - 100$ km s^{-1}. Thus, the net velocity is primarily determined by the orbital motion for most binary separations. Figure 2.9 shows the ratio of kick speed to the total speed, assuming that the kick velocity is perpendicular to the orbital velocity. If the mass transfer in the binary system is via RLOF, then the kick contributes little to the total velocity. For very small orbital separations, the kick contributes at most $\sim\ 10 - 20\%$ of the total.

Based on these observations, we may expect that helium stars with high space motion found to be associated with Type Ia supernova remnants would be evidence for SNe Ia proceeding through the helium-

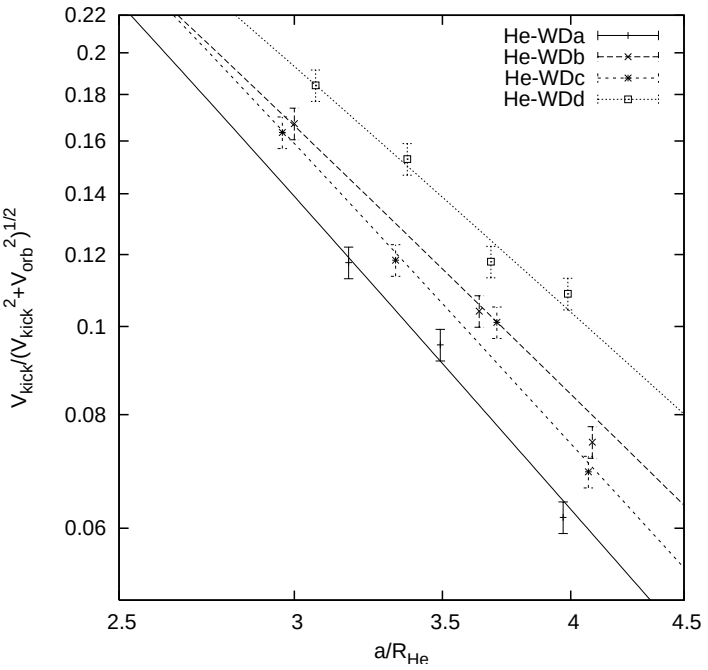

Figure 2.9: The ratio of kick speed to total speed for different helium-star models as a function of initial separation. Lines: from the fitted kick velocity. Data: from the calculated kick velocity. Error bars are based on the 4% error determined in our convergence test. We assume the kick velocity to be perpendicular to the orbital velocity.

star single-degenerate channel. If such objects are also found to have enhanced iron abundances relative to helium, this evidence would be considerably strengthened. In such cases the relative velocity between the helium star and the centroid of the supernova remnant would place a stronger constraint on the initial binary separation than on the initial helium star's mass or the white dwarf mass.

2.5 Conclusions

We have investigated the impact of SN Ia ejecta on a companion star in the single-degenerate helium-star channel for the short-delay-time population of SN Ia via two-dimensional hydrodynamical simulations using a range of helium-star models and binary orbital separations. Although the general behavior of the temporal evolution is similar to that in previous studies by Marietta et al. (2000) and Pakmor et al. (2008) for main-sequence and red-giant companions, the amount of matter unbound from the helium stars is less than for hydrogen-rich companions. Due to the shorter orbital periods of helium-star progenitor systems, the space motion of the companion star after the explosion is found to be higher. We find a power-law relation between the unbound mass and initial binary separation that is consistent with the previous studies, suggesting that the power-law behavior is not strongly sensitive to the nature of the companion. The kick velocity can

also fitted by a power-law and we conclude that the power-law index may reflect the relative importance of the effect of ablation. An upper limit on the amount of nickel captured by the helium star is found to be $\sim 5 \times 10^{-4}\ M_{\odot}$. The ratio of nickel to helium abundance may be useful as a diagnostic of such events in future observational studies of SN Ia stellar remnants.

Future work in this area will include relaxing the assumption of axisymmetry to model the mixing of ejecta with the helium star by including the binary orbital motion in three spatial dimensions. Additionally, including radiation transfer within these simulations will allow us to determine how much of the helium is ionized, allowing us to make direct contact with spectroscopic constraints on the presence of helium in these systems.

Chapter 3

Impact of Type Ia Supernova Ejecta on Binary Companions in the Single-Degenerate Scenario[†]

Abstract

Type Ia supernovae are thought to be caused by thermonuclear explosions of a carbon-oxygen white dwarf in close binary systems. In the single-degenerate scenario (SDS), the companion star is non-degenerate and can be significantly affected by the explosion. We explore this interaction by means of multi-dimensional adaptive mesh refinement simulations using the FLASH code. We consider several different companion types, including main-sequence-like stars MS, red giants (RG), and helium stars (He). In addition, we include the symmetry-breaking effects of orbital motion, rotation of the non-degenerate star, and Roche-lobe overflow. A detailed study of a sub-grid model for Type Ia supernovae is also presented.

We find that the dependence of the unbound stellar mass on the initial binary separation can be fitted by a power-law relation. The power-law index is found to be about -3.5 to -3.7 for the main-sequence star, -2.9 to -3.4 for the helium star, and -4.0 to -4.2 for the red giant. After the explosion, the companion receives a kick from the supernova ejecta. It is found that the kick velocity also is related to the binary separation by a power law, except for the red giant companion, due to the large numerical uncertainty created by the small kick in this case. The power-law index is found to be about -1.7 to -1.9 for the main-sequence star and -2.6 to -2.8 for the helium star. By using tracer particles in FLASH, the process leading to the unbinding of matter can be determined by analyzing the fluid elements in a time sequence. It is found that the process is dominated by ablation, which has usually been neglected in past analytical studies. The level of Ni/Fe contamination of the companion that results from the passage of the supernova ejecta is found to be $\sim 10^{-5} M_\odot$ for the MS star, $\sim 10^{-4} M_\odot$ for the He star, and $\sim 10^{-8} M_\odot$ for the RG, suggesting that the ratio of nickel/iron to hydrogen plus helium abundance in the remnant should be found to be larger than the solar ratio if the contamination is mixed only in the companion's envelope. A hole in the ejecta shadowed by the companion star also is found in the simulation, which is a possible source of the variation in SN Ia

[†] Published as Kuo-Chuan Pan, Paul Ricker, and Ronald Taam 2012, ApJ, 750, 151

light curves. The spinning MS companion star loses about 48% of its initial angular momentum during the impact, causing the rotational velocity to drop to 23% of the original rotational velocity, suggesting that the Tycho G star is a promising progenitor candidate in the SDS.

3.1 Introduction

Type Ia supernovae (SNe Ia) are considered to be "standardizable" candles when measuring the distance of distant objects (Phillips, 1993) and thus play an important role in cosmology, helping determine key cosmological parameters (Branch & Tammann, 1992; Riess et al., 1998; Schmidt et al., 1998; Perlmutter et al., 1999). Most cosmological applications using SNe Ia are based on an assumption that the homogeneity of SNe Ia applies to high-redshift SNe Ia. However, this assumption is questionable until we fully understand the nature of the progenitors of SNe Ia. According to recent studies, SNe Ia are believed to be thermonuclear explosions of carbon-oxygen (CO) white dwarfs (WDs), but the ignition mechanism and the progenitor systems are still unknown.

Current popular progenitor models are classified into two major scenarios, the single-degenerate scenario (SDS, Whelan & Iben (1973); Nomoto (1982)) and the double-degenerate scenario (DDS, Iben & Tutukov (1984); Webbink (1984)). The SDS involves a CO WD accreting matter from a non-degenerate binary companion, such as main-sequence (MS) stars, red giants (RG), or helium stars (He). The CO WD eventually becomes unstable and then, when the mass reaches the Chandrasekhar limit ($M \sim 1.4 M_{\odot}$), it explodes as a SN Ia. The DDS instead involves two CO WDs, with total mass larger than the Chandrasekhar mass, that merge together because of the emission of gravitational waves.

With the DDS, the lack of hydrogen spectral lines is easy to explain; however, the homogeneity of the explosion energy is difficult to account for since the total mass of the binary system varies from case to case. Furthermore, it is possible that WD-WD mergers end with the production of an ONeMg WD followed by accretion-induced collapse to a neutron star (Nomoto & Iben, 1985). Badenes & Maoz (2012) calculate the merger rate of binary WDs in the Galactic disk based on the observational data in the Sloan Digital Sky Survey. They conclude that the merger rate of binary WDs with super-Chandrasekhar masses would not significantly contribute to the SNe Ia rate. The SDS produces a relatively fixed explosion energy, which accounts for the homogeneity. The non-degenerate companions in the SDS, however, are usually hydrogen-rich which leads to the H/He contamination problem in the SDS (see Livio (2000) and Hillebrandt & Niemeyer (2000) for detailed descriptions of the advantages and weaknesses of the SDS and DDS).

Recent studies based on the delay time distribution (DTD) suggest the need for at least a two-component

model for the DTD. In particular, Scannapieco & Bildsten (2005), Mannucci et al. (2006) and Brandt et al. (2010) found that the observations can be fitted with a short-delay-time population ($\sim 10^8$ yr) and a long-delay-time population ($3 - 4$ Gyr).

The calculations of SN Ia rates and DTD using binary population synthesis can be matched with both the SDS (Han & Podsiadlowski, 2003; Hachisu et al., 2008b) and the DDS (Pritchet et al., 2008; Ruiter et al., 2009). The uncertainties in the observed DTD, however, are dominated by the uncertainties in galactic stellar populations and star formation histories (Maoz & Mannucci, 2011). Thus, it is still hard to distinguish between the viability of the SDS and the DDS progenitor models without more detailed observations.

With detailed binary calculations, the long-delay-time population can be understood in terms of progenitor systems characterized by a MS-like companion in the MS-WD channel (Ivanova & Taam, 2004; Wang et al., 2010; Wang & Han, 2010a) and/or by an RG in the RG-WD channel (Hachisu et al., 1999, 2008b). In contrast, the short-delay-time population may consist of systems with a massive MS star in the MS-WD channel (Hachisu et al., 2008b) or with a He-star in the He-WD channel (Wang et al., 2009). Therefore, the more likely explanation is that both SDS and DDS have contributed to SNe Ia.

Several detailed hydrodynamics simulations with the SDS have been studied in the past decade. Marietta et al. (2000) examined the impact of a SN Ia on a MS star, a sub-giant, and a RG using two-dimensional Eulerian hydrodynamics. Marietta et al. (2000) found that the MS star and sub-giant companions lose 15% of their mass after the explosion, and the RG companion loses about $96\% - 98\%$ of its envelope. They also found that the impact of SN ejecta with the companion star creates a hole with an opening angle of $\sim 30^\circ$ in the high-velocity ejecta and $\sim 40^\circ$ in the low-velocity ejecta. This hole corresponds to $7\% - 12\%$ of the ejecta's surface, making the supernova remnant (SNR) anisotropic and potentially affecting Si II spectral line shapes.

Pakmor et al. (2008) re-examined the MS-WD channel and updated these results by considering the pre-supernova binary evolution from Ivanova & Taam (2004) and using three-dimensional smoothed particle hydrodynamics (SPH) simulations. They found strong dependences of unbound mass and kick velocity on initial binary separation with power-law relations. Because of the relatively small number of particles in their SPH simulations, they were unable to reproduce the turbulence in Marietta et al. (2000). However, their comparison to Marietta et al. (2000) found that the unbound mass does not depend much on the numerical method used. Although the unbound mass is not sensitive to the turbulence around the MS star, other important physical quantities, e.g. contaminated SN ejecta on the companion star, may be sensitive to small-scale turbulence.

In contrast with Marietta et al. (2000), Pan et al. (2010) studied the He-WD channel from Wang et al. (2009) for the short-delay-time population, using two-dimensional Eulerian hydrodynamics simulations with adaptive mesh refinement. They also found the same power-law relations in unbound mass and kick velocity as Pakmor et al. (2008), but with different power-law indices. An upper limit of the ratio of Ni/Fe contamination to the helium abundance was found to be $\sim 9 - 50 \times 10^{-4}$, which is higher than the solar abundance ratio. This result suggests the possibility of detecting remnant helium stars in their SNR.

In this paper, we examine the SDS using the above discussed companion star models to determine whether the contamination problem of H/He in the companion envelope can be overcome. We revisit this problem using modern adaptive mesh refinement (AMR) and different companion models that incorporate the effects of binary evolution. We include the symmetry-breaking effects of orbital motion, rotation of the non-degenerate star, and Roche-lobe overflow (RLOF). In the next section, the numerical methods and the construction of initial setups are described. Our numerical results for different companion models are reported in Section 3. In Section 4 we present a parameter study made by varying significant physical quantities and then discuss the possible observational implications. In the final section, we summarize our results and conclude.

3.2 Numerical methods and models

3.2.1 Numerical codes

Two different codes are employed in this work. The first one is a stellar evolution code used to construct the non-degenerate stellar models. The second code is a multi-dimensional hydrodynamics code to simulate the impact of type Ia supernova ejecta.

The stellar evolution code used is MESA (Modules for Experiments in Stellar Astrophysics, Paxton et al. (2011)). MESA combines many sophisticated numerical methods to control time and space resolutions, and many state-of-the-art physical modules to solve the stellar structure. For a given initial stellar mass and metallicity, MESA evolves stars to a certain age and provides all the physical quantities we need for the hydrodynamics simulations.

For the SN Ia simulations, we use FLASH version 3 (Fryxell et al., 2000; Dubey et al., 2008). FLASH is a parallel, multi-dimensional hydrodynamics code based on block-structured adaptive mesh refinement (AMR). To solve the Euler equations, we use the split piecewise parabolic method (PPM) solver (Colella & Woodward, 1984) in FLASH. The equation of state (EOS) applied is the Helmholtz EOS (Timmes & Swesty, 2000), which is interpolated from a precomputed table of the Helmholtz free energy. It includes contributions from

Table 3.1: The non-degenerate companion models.

Model	M^{a} ($M_\odot$)	R_*^{b} (km)	ρ_c^{c} (g/cm^3)	P_c^{d} (dyne/cm^2)	T_c^{e} (K)	t_{dyn}^{f} (sec)
HCV'	1.027	6.76×10^5	112.3	1.90×10^{17}	1.48×10^7	1.54×10^3
MS-WD	1.17	5.51×10^5	68.9	1.33×10^{17}	1.44×10^7	1.06×10^3
RG-WD	0.98	2.15×10^7	$3.17 \times 10^{-3,\dagger}$	$5.50 \times 10^{11,\dagger}$	$1.88 \times 10^{6,\dagger}$	2.82×10^5
He-WDc	1.007	1.36×10^5	6.10×10^3	5.12×10^{19}	1.28×10^8	1.40×10^2

[a] Stellar mass, M
[b] Stellar radius, R_*
[c] Central density,ρ_c
[d] Central pressure, P_c
[e] Central Temperature, T_c
[f] The dynamical time scale, $t_{dyn} = 1/2(G\rho)^{-1/2}$
[†] For the RG-WD model, the central density, pressure and temperature are the central values of the envelope mapped in FLASH, not the core values in MESA.

radiation, completely ionized nuclei, and degenerate electrons and positrons for an optically thick mixture of gas and radiation in local thermodynamic equilibrium. Magnetic fields are ignored, but self-gravity is considered and solved using the multipole Poisson solver in 2D and using the multigrid Poisson Solver in 3D (Ricker, 2008). Particle modules in FLASH 3 have the ability to treat both active and passive particles. Active particles are massive particles that interact through gravity with other active particles and fluid elements. Passive particles are massless particles that only follow the motion of fluid elements in Lagrangian coordinates. We use active particles to represent the CO WD and the core of the RG companion and passive particles to monitor the motion of fluids.

3.2.2 Non-degenerate companion models

In order to compare our setup with previous work by Marietta et al. (2000) and Pakmor et al. (2008), we use MESA to create a MS star companion model similar to the HCV scenario in Marietta et al. (2000). The HCV scenario in Marietta et al. (2000) is a hydrogen cataclysmic variable system consisting of a MS star and a CO WD. We assume the binary system is in RLOF and has a binary separation $a = 3R_*$ at the onset of the SN Ia explosion. The MS star companion in the HCV scenario has a mass $M = 1.017$ $M_\odot$ and radius $R_* = 6.8 \times 10^5$ km. Because of the lack of certain physical data in the HCV scenario, we created a similar MS star model, named HCV', with $M = 1.027$ $M_\odot$, and $R_* = 6.76 \times 10^5$km.

For more realistic models, we use models of SN Ia progenitor candidates taken from detailed binary calculations. Based on current studies, we chose three possible stellar types of binary companions in the SDS: MS stars, RGs, and He stars.

Ivanova & Taam (2004) studied the evolution of binaries consisting of evolved MS stars with WDs. They

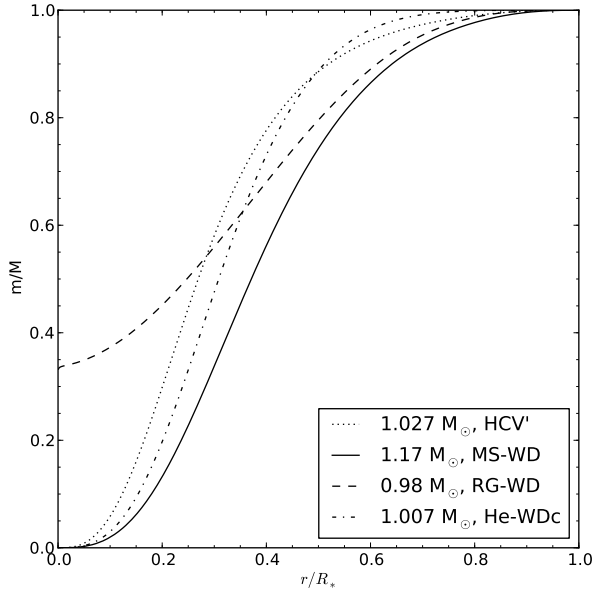

Figure 3.1: Mass vs. radius profiles for the main sequence, red giant, and helium star models. For the RG-WD scenario, only the envelope mass of the RG is plotted here.

also investigated possible channels that may eventually evolve to SNe Ia. We chose parameters from the case with final mass $M_{\rm d;f} = 1.17 M_\odot$ for the MS star and initial orbital period $P = 1$ day to construct a model of a MS-WD binary system (the system is denoted by MS-WD in our simulations).

Hachisu et al. (1999) have proposed an alternative binary channel consisting of a WD and a low-mass RG. The accreting WD in this model has a strong optically thick wind, which broadens the range of parameters leading to SNe Ia. We also adopt the case P1 in Hachisu et al. (1999) for our simulations (denoted by RG-WD here). This system consists of a one solar mass WD and a two solar mass RG with an initial orbital period $P_0 = 300$ days. The system ends with a SN Ia after 7.2×10^5 years; the mass of RG becomes $0.98 M_\odot$ at the onset of the SN Ia explosion.

For the helium star model, we rely on the model originally proposed by Wang et al. (2009) as well as the case where the binary system is in a stable He-shell burning phase at the onset of the SN explosion (Case 2 in Wang et al. (2009)). This model also is the He-WDc model applied in Pan et al. (2010), but with nonuniform chemical composition. The mass of this helium star model is $1.007 M_\odot$ (denoted by He-WDc).

In MESA, we do not follow full binary evolution but use the initial conditions with a constant mass-loss rate, estimated from the above references as an approximation. The mass-loss rate used is taken to be the ratio of the mass change to the evolution time in the above references. All models we created from MESA are summarized in Table 3.1, and the mass versus radius profiles are shown in Figure 3.1.

3.2.3 Initial setup

We conduct two- and three-dimensional hydrodynamics simulations to investigate the impact of SN Ia ejecta on the binary companions. In the three-dimensional calculations, we rely on Cartesian coordinates; the simulation box dimensions are set to a size equal to 30 times the radius of the non-degenerate companion star (R_*) in all directions. The companion star is located at the center of the simulation box for convenience. Two-dimensional models are calculated in cylindrical coordinates due to the axial symmetry if the orbital motion of the binary system is ignored. The simulation box dimensions are set to $15R_*$ in the radial (r) direction and $30R_*$ in the axial (z) direction. We interpolated the one-dimensional model onto the FLASH grids using up to 10 levels of refinement based on the magnitudes of the second derivatives of gas density and pressure. Each AMR block contains 8^3 zones in the three-dimensional box and 8×16 zones in the two-dimensional box. This corresponds to an effective uniform resolution of 4096^3 in three-dimension and 4096×8192 in two dimensions. To simplify the problem, the compositions from MESA are adjusted to hydrogen (^{1}H), helium (^{4}He) and carbon (^{12}C) only (companion material). We use outflow boundary conditions for fluids and isolated boundary conditions for the Poisson solver.

In an Eulerian hydrodynamics code like FLASH, physical properties are calculated at fixed spatial positions. It is difficult to trace fluid elements in a time sequence. However, FLASH has the ability to trace fluid elements using passive particles. Passive particles are massless particles that only follow the motion of fluid elements in Lagrangian coordinates without interacting with fluids. In our simulations, 10^6 passive particles are distributed with the gas density in order to study the history of shocked gas.

For the RG model, although we have AMR, the core of the RG still cannot be resolved with current computational resources. Thus, we use a rigid spherical particle cloud with 3×10^5 active particles to represent it. We artificially modify the physical quantities within the core region of the RG to increase linearly with the radius and then reconstruct the model on multi-dimensional grids in FLASH. Therefore, the mass difference between the real stellar model and the reconstructed model in FLASH is the core mass of the RG ($M_{\rm RG,c} = 0.311 M_\odot$). The radius of the particle cloud is set to three times the smallest zone spacing; the force on the cloud uses cloud in cell (CIC) interpolation. We utilize a particle cloud, instead of a single particle, to avoid the problem of force anisotropy in CIC (Ricker & Taam, 2008).

In order to validate our models in hydrostatic equilibrium and to reduce the geometrical distortion between one dimension and multi-dimensions, all models are relaxed on the multi-dimensional Eulerian grid by artificially damping the gas velocity for 5 dynamical time scales ($t_{\rm dyn} = 1/2(G\rho)^{-1/2}$). During this time, a damping factor, smoothly increased from 0.7 to 0.99 on the gas velocity, is imposed at each timestep. We ensure that the companion models remain relatively stable during the relaxation and that the Mach number

is always smaller than 0.01.

After relaxation, we introduce asymmetric effects from orbital motion by adding a WD into the simulation box (three-dimensional runs only). The WD is represented by another particle cloud with 3×10^5 particles and its mass is set to $M = 1.378 M_\odot$ (we assume the binary system is about to explode). In the three-dimensional simulations, the orbital plane is set on the $x - y$ plane and the WD is placed on the positive $x-$axis (positive radial direction in two dimension) with a binary separation a. Positive $z-$axis is set to the direction of angular momentum. The binary system is assumed to be in RLOF and the binary separation is calculated using equation 3.1 (Eggleton, 1983):

$$\frac{R_L}{a} = \frac{0.49 q^{2/3}}{0.6 q^{2/3} + \ln(1 + q^{1/3})}, \tag{3.1}$$

where R_L is the radius of the Roche lobe-filling star, and q is the mass ratio. The non-degenerate binary companion has a spin with a spin-to-orbit ratio of 0.95. In this phase, the maximum AMR level is reduced to 8 levels to save computation time and the AMR level is forced to the maximum level (8) in two spherical regions centered on the WD and the companion star within a radius of $R < 1.8 R_*$. AMR levels in other regions are calculated from the second derivative of gas density and pressure and limited to 6 levels (a situation denoted by 6/8 levels, equivalent to a 1024^3 uniform grid in three dimensions and 1024×2048 in two dimensions).

3.2.4 The supernova model

After the binary system is placed in the simulation box, we simulate the binary evolution for a few orbital periods. During this phase, mass transfer via RLOF occurs and the companion star is slightly distorted due to the tidal force. With current computational resources, we cannot simulate the whole delay time in multi-dimensional hydrodynamics simulations. We therefore simulate the binary evolution for only a few orbital periods ($< 3 P_{\rm orb}$) and assume the morphology does not change much once the RLOF is stable. We tested the impact of a SN Ia explosion on the binary companion using different binary evolution times. We find that binary evolution only affects the morphology of the SNR at a late time and does not alter significantly the impact on the companion star. Thus, all the runs we describe later ignore the binary evolution. The orbital velocity and spin, however, are still considered.

To introduce a SN Ia explosion, we remove the WD particle cloud and replace it with a high-density and high-temperature gas. The physical quantities used to describe the SN Ia explosion are taken from the W7 model by Nomoto et al. (1984). It has a mass $M_{\rm sn} = 1.378 M_\odot$, total explosion energy $E_{\rm sn} = 1.233 \times 10^{51}$

erg, and average ejecta speed $v_{\rm sn} = 8.527 \times 10^3$ km s^{-1}. The kinetic energy of the WD from the orbital motion also is added to the SN. We rely on nickel (^{56}Ni) as a tracer for the SN Ia material.

Although we have AMR, the WD is still much smaller than the minimum zone spacing. Thus, a sub-grid model is required to approximate the SN Ia explosion. To minimize grid effects, we use a small spherical region with a radius equal to fifteen times the smallest zone spacing to represent the SN material. Even if we put in the same amount of explosion mass and energy, the results are actually sensitive to the initial distribution of the SN ejecta within this small region. The detailed setup of the sub-grid SN model and the corresponding behavior will be discussed in the next section.

3.3 Results

In this section, the evolution of the companion stars during the SN Ia explosion for the MS star, RG, and He-star binary companions (all the simulation cases are summarized in Table 3.2) is qualitatively described. Convergence tests of the two-dimensional and three-dimensional simulations were performed to determine the sensitivity of the numerical spatial resolutions. A detailed description of the SN Ia explosion subgrid model setup is examined as well.

3.3.1 A qualitative description of the evolution after the SN Ia explosion

Figure 3.2 demonstrates a typical evolution of the gas density in the orbital plane for the impact of a SN Ia in the MS-WD scenario. In this case (the case MS-Nr in Table 3.2), the simulation is three-dimensional, but the orbital motion is ignored. The initial binary separation is 1.51×10^{11} cm, $\sim 3R_*$, and 6/8 levels of refinement are used. At 88 sec, the SN ejecta reaches the MS star companion and forms a bow shock at the leading surface of the MS star (label A in Figure 3.2). The bow shock extends further, creating an opening angle with $\sim 40^\circ$ with respect to the $x-$axis. As the shock propagates further, the ejecta sweep around the MS star. At about 200 seconds, the ejecta fully surround the MS star and self-interact at the back side of the MS star (label B Figure 3.2 at 203 sec). Subsequently, a cone-shape tail shock forms (label B at 431 sec). The shock waves also penetrate the MS star (label C in Figure 3.2), reaching the center at about 431 seconds. When the shock passes through the MS star, a reverse shock begins to reflect and refill the central SN region (label D in Figure 3.2). The reverse shock mainly contains companion material and forms a solid angle spanning about $40^\circ - 50^\circ$ with respect to the $x-$axis. After the impact, the MS star pulsates, creating shocks around the surface of the MS star (label E in Figure 3.2). By the end of the simulation, $0.18 M_\odot$ of mass has been lost (gravitationally unbound) due to the impact of the SN Ia. The MS star also

Table 3.2: Simulations

Case	a[a] (cm)	$\delta M_{\rm ub}$[b] ($M_\odot$)	$\delta v_{\rm kick}$[c] (km/sec)	$v_{\rm orb}$[d] (km/sec)	$M_{\rm str}/M_{\rm abl}$[e] ($M_\odot$)
MS-r	1.51×10^{11}	2.08×10^{-1}	114	256	0.65
MS-4	2.20×10^{11}	5.00×10^{-2}	58.8	212	0.43
MS-5	2.75×10^{11}	2.41×10^{-2}	39.6	190	0.73
MS-Nr	1.51×10^{11}	1.80×10^{-1}	112	0	0.49
MS-N4	2.20×10^{11}	4.35×10^{-2}	57	0	0.39
MS-N5	2.75×10^{11}	2.31×10^{-2}	41	0	0.58
MS-2D-Nr	1.51×10^{11}	1.84×10^{-1}	113	–	–
MS-2D-N4	2.20×10^{11}	4.21×10^{-2}	59.5	–	–
MS-2D-N5	2.75×10^{11}	2.08×10^{-2}	36	–	–
RG-r	6.13×10^{12}	6.37×10^{-1}	12	41.8	0.01
RG-4	8.58×10^{12}	5.93×10^{-1}	25	35.3	0.06
RG-5	1.07×10^{13}	5.07×10^{-1}	19	31.6	0.19
RG-Nr	6.13×10^{12}	6.37×10^{-1}	14	0	0.01
RG-N4	8.58×10^{12}	5.97×10^{-1}	23	0	0.046
RG-N5	1.07×10^{13}	4.99×10^{-1}	4.6	0	0.16
He-r	3.86×10^{10}	2.3×10^{-2}	65.6	522	0.82
He-4	5.43×10^{10}	8.1×10^{-3}	28.9	440	0.74
He-5	6.79×10^{10}	4.11×10^{-3}	14.7	394	0.74
He-Nr	3.86×10^{10}	1.99×10^{-2}	77	0	0.48
He-N4	5.43×10^{10}	7.3×10^{-3}	29	0	0.53
He-N5	6.79×10^{10}	3.82×10^{-3}	15.5	0	0.56
He-2D-Nr	3.86×10^{10}	1.73×10^{-2}	63	–	–
He-2D-N4	5.43×10^{10}	5.3×10^{-3}	12.7	–	–
He-2D-N5	6.79×10^{10}	2.6×10^{-3}	6.3	–	–

[a] The initial orbital separation, a

[b] The final unbound mass, $\delta M_{\rm ub}$, described in equation 3.4.

[c] The kick velocity, $\delta v_{\rm kick}$, described in equation 3.5.

[d] The initial orbital speed

[e] The stripped mass to ablated mass ratio

[†] Note: The cases beginning with "MS," "RG," and "He" correspond to the MS-WD, RG-WD, and He-WDc scenarios in Table 3.1, respectively. The detailed description for the notations of simulation cases is described in Section 3.3.4. Orbital motion and passive particles are not included in the two-dimensional simulations, so for these cases the orbital velocity and stripped to ablated ratio are not calculated.

receives linear momentum and hence a kick of 112 km/sec from the ejecta.

Qualitatively, the simulation resembles the results in Marietta et al. (2000) and Pakmor et al. (2008). The case rp3_20a in Pakmor et al. (2008) resembles ours, except that the orbital separation is smaller ($a = 2.68 \times 10^{11}$ cm in Pakmor et al. (2008)). The clearer shock structures reveal typical behavior when comparing grid-based hydro and SPH simulations. The most significant difference is the absence of a reverse shock in the SPH simulations. Although Pakmor et al. (2008) demonstrated that their SPH code could produce the same amount of unbound mass as a grid-based hydro code, we believe that the high-speed reverse shock actually plays a more important role for the dynamics of the remnant star as it could take away some momentum from the SN ejecta.

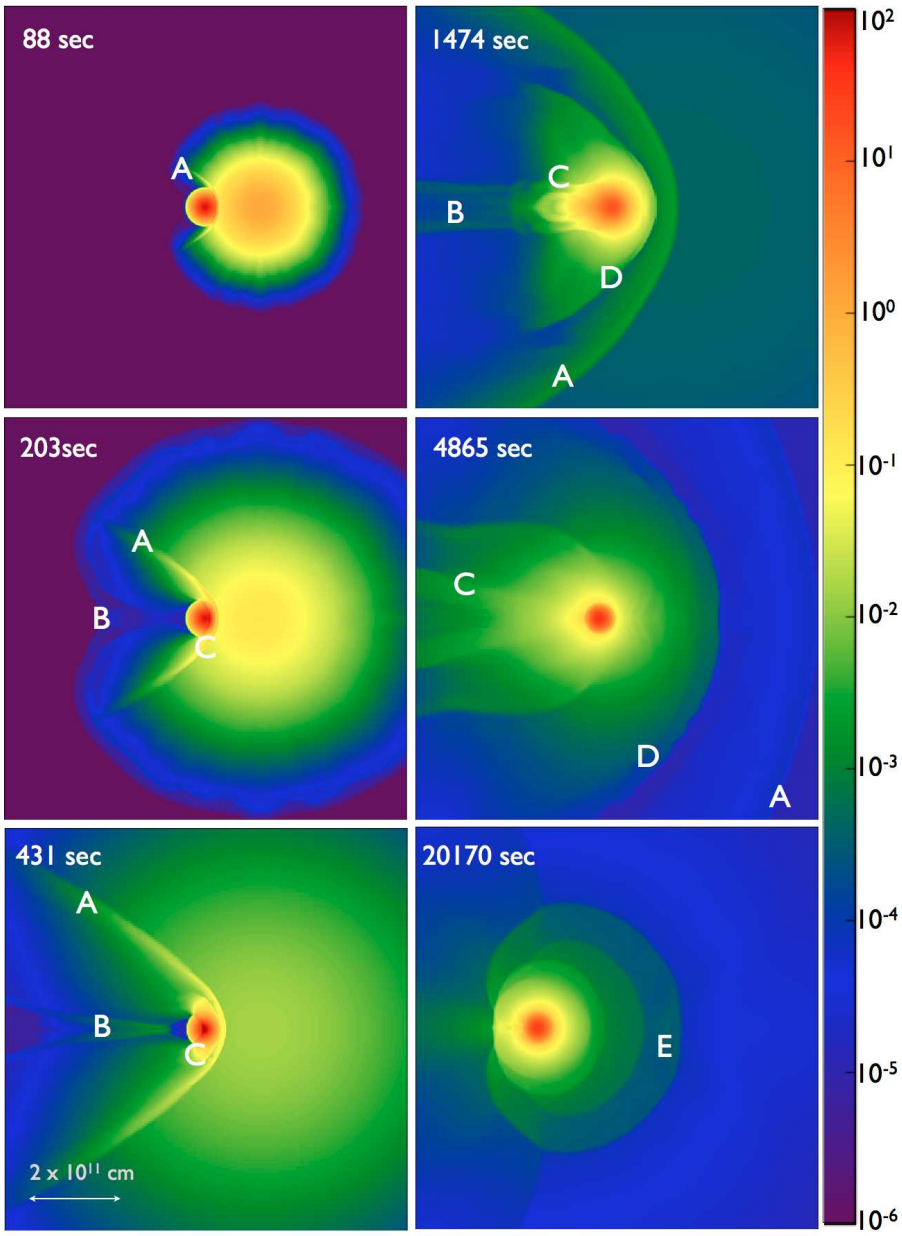

Figure 3.2: Gas density distribution in the orbital plane for a three-dimensional SN Ia simulation with a MS star binary companion (case MS-Nr in Table 3.2). The initial orbital separation is 1.51×10^{11} cm (RLOF), but orbital motion is ignored. Each frame shows a portion of the domain spanning $20R_*$ at the labeled simulation time. The color scale indicates the logarithm of the gas density in g cm^{-3}

.

3.3.2 Effects due to the subgrid SN Ia setup

In SNe Ia, hydrogen has not been detected. However, hydrogen-rich material from the accretion disk or from mass stripping during the SN impact is possible and could be detectable when the SN ejecta become transparent. Thus, one of the most significant quantities we wish to determine is the amount of mass lost from the hydrogen-rich companion star after the SN Ia explosion. The unbound mass could be found by calculating the difference between the initial mass of the companion star and the integrated total bound mass from the companion at each timestep. The total bound mass is the sum of the companion cell masses in all zones for which the total energy is negative.

Because of the limitation of spatial resolution, the explosion cannot be perfectly modeled. It is found that the amount of unbound mass is sensitive to the sub-grid model representing the SN Ia. Therefore, a realistic description of the SN Ia explosion is required in addition to including the correct amount of energy.

Dwarkadas & Chevalier (1998); Dwarkadas (2000) examined the interaction of SN Ia ejecta with the surrounding interstellar medium, suggesting a density profile characterized by an exponential for setting up the SN Ia explosion. However, our simulations are restricted to a much smaller scale (10^{10} cm to 10^{13} cm rather than 10^{15} cm); the binary companion will break the self-similarity of the SN explosion. Thus, the exponential decay may not be appropriate here. We experimented with several different initial distributions of SN Ia in order to study their effect on the post-impact companion star.

The most simple and naive model is to set up a uniform density and constant radial velocity distribution in the SN region (denoted by CV SN). However, in reality, the beginning of the explosion looks more like a Sedov explosion. Thus, a second model is set up with the radial velocity distribution linearly increasing with radius; the gas density is assumed to be uniformly distributed (denoted by LV SN). We calculated the amount of unbound mass after the SN Ia explosion for these models and found that the different SN Ia models will result in a difference of unbound mass of about $\sim 0.05 - 0.3 M_{\odot}$ (see Figure 3.3).

Thus, a more realistic sub-grid model is necessary to model the SN Ia explosion. The early time evolution and distribution of the W7 model is well described in Nomoto et al. (1984). We approximate the density profile in Figure 4b of Nomoto et al. (1984) by following a power-law distribution with a fixed slope in the $M - r$ relation when the explosion expands to the size of our sub-grid model, R_c. For a given total mass ($M_{\rm WD}$) and an explosion size ($R_{\rm c}$), the density profile can be calculated by

$$\rho(r) = \frac{M_0}{r^3 + \zeta R_{\rm c}^3} \tag{3.2}$$

where $M_0 = 2.4998 \times 10^{32}$ g is a constant only related to the slope of the $M - r$ relation in Nomoto et al.

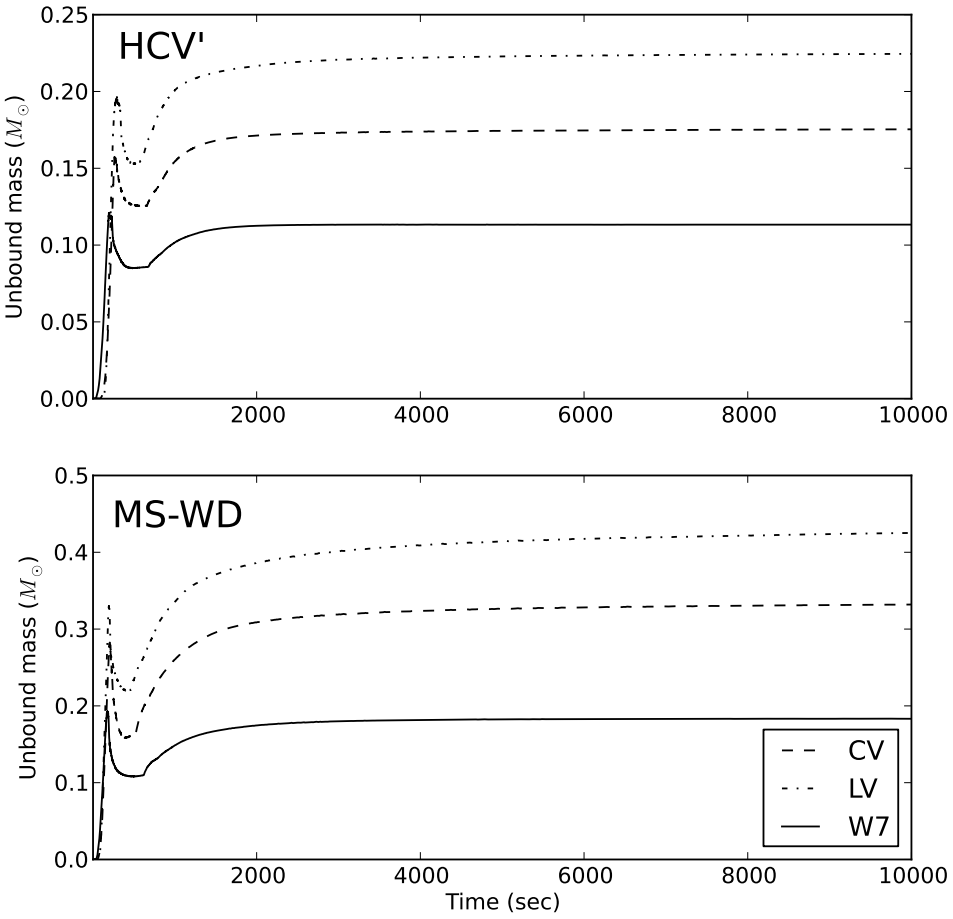

Figure 3.3: Unbound mass vs. simulation time for different SN explosion setups (UPPER: HCV'; LOWER: MS-WD). CV denotes the case with constant density and radial velocity distribution; LV denotes the case in which the velocity is linearly increased in radius, but the density distribution is uniform; W7 denotes the fitted model described in section 3.2.4. The simulations are two-dimensional, and the binary separation is 2.03×10^{11} cm ($= 3R_*$) for the HCV' scenario and 1.51×10^{11} cm ($\sim 2.74R_*$) for the MS-WD scenario.

(1984). The other constant,

$$\zeta = \left(e^{\frac{3M_{\rm WD}}{4\pi M_0}} - 1\right)^{-1} \tag{3.3}$$

depends on M_0 and $M_{\rm WD}$. The velocity distribution also is assumed to increase linearly in radius, $v(r) = fv_{\rm sn}(r/R_{\rm c})$, which is a reasonable assumption and comparable with Figure 4c of Nomoto et al. (1984). If we know the density distribution and the total kinetic energy, the coefficient of the velocity profile, f, can be calculated by integrating the kinetic energy density. Based on the temperature profile in Figure 4a of Nomoto et al. (1984), we assume the temperature is uniformly distributed. We use the Helmholtz EOS solver to iterate the temperature until the total explosion energy is equal to 1.233×10^{51} erg (denote by W7 SN).

Figure 3.3 illustrates two-dimensional simulations of the unbound mass versus simulation time with different SN Ia models and different companion models (HCV' and MS-WD). For the HCV' companion model, the final unbound mass is $0.113M_\odot$ for the W7 SN model, $0.175M_\odot$ for the CV SN model, and $0.225M_\odot$ for the LV SN model. Marietta et al. (2000) obtained $0.15M_\odot$ by using their HCV model; Pakmor et al. (2008) using the same model but with an SPH simulation, obtained $0.134M_\odot$. Their final unbound mass is between our CV SN model and W7 SN model.

For the other companion model, the MS-WD scenario, we obtained $0.179M_\odot$ for the W7 SN model, $0.330M_\odot$ for the CV SN model, and $0.427M_\odot$ for the LV SN model. Pakmor et al. (2008) used the same companion from Ivanova & Taam (2004); due to the difference of constructing this model, Pakmor et al. (2008) has a slightly larger radius and different material compositions. From their fitted power-law relation, the final unbound mass at our initial binary separation ($a = 2.74R_*$) is $0.19M_\odot$, which is consistent with our results. We therefore use the W7 SN model for all other cases in this paper.

3.3.3 Convergence test

In order to check the sensitivity of unbound mass to spatial resolution, we performed convergence tests on two-dimensional and three-dimensional simulations using the MS-WD companion model. We performed several simulations with the same initial binary separation ($a = 1.51 \times 10^{10}$ cm), and the same W7 SN model for the SN Ia explosion, but with several different AMR levels, computing the amount of unbound mass as a function of time for each simulation. In Figure 3.4, we see that the unbound mass decreases when the zone spacing decreases; the decrement changes very little from 6/8 to 7/9 levels. The difference between 6/8 (corresponding to 1024^3 in 3D and 1024×2048 in 2D) and 7/9 (corresponding to 2048^3 in 3D and 2048×4096 in 2D) levels is within 3%. The final unbound mass of this two-dimensional run for the MS-WD scenario is $M_{\rm ub} = 0.175M_\odot$.

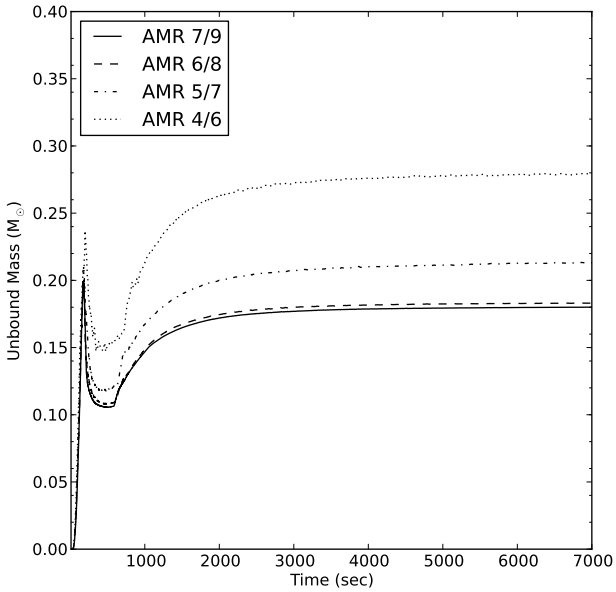

Figure 3.4: Unbound mass from the companion star vs. simulation time using different AMR refinement levels for the MS-WD scenario. The initial binary separation is 1.51×10^{11} cm and the calculation is two-dimensional.

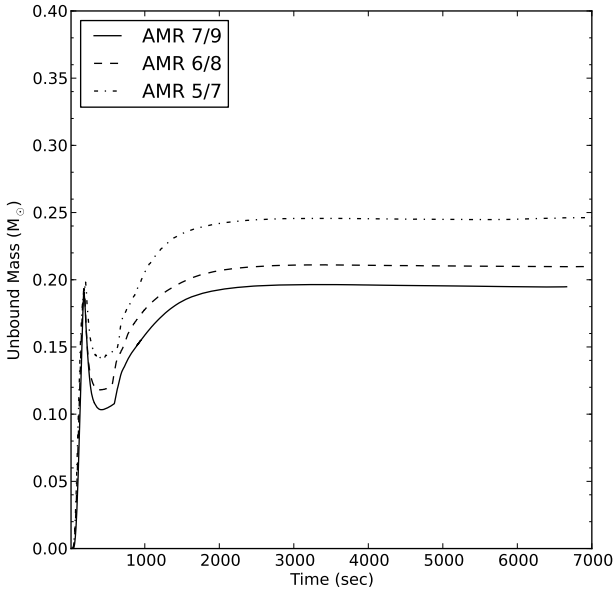

Figure 3.5: Similar to Figure3.4, but with three-dimensional simulations, including orbital motion and spin.

For the convergence test of three-dimensional simulations, we use the same companion model (MS-WD), but the spin and orbital motion are included. In this stage, we are only interested in the sensitivity to numerical resolution during the SN Ia explosion. Thus, we ignored the effects of accretion of Roche-filling material, i.e. the WD exploded immediately when it was added to the simulation. The result is shown in Figure 3.5. The convergence behavior is the same as for two-dimensional simulations. However, three-dimensional runs require a higher AMR level for the same spatial resolution because the cylindrical mesh has only half of the zone spacing, due to symmetry, of the Cartesian mesh for the same number of AMR levels. The final unbound mass $M_{\rm ub} = 0.195 M_\odot$ for 7/9 levels. The difference between 6/8 and 7/9 is about 8%, which is larger than the difference in the two-dimensional case. However, a full set of runs at 7/9 levels proved to be too expensive for us to undertake. Thus, we chose 6/8 levels for all other production runs.

3.3.4 Evolution of the companion star after the SN Ia explosion

We have performed several simulations with the MS-WD, RG-WD, and He-WDc companions (see Table 3.1). For each scenario, we ran cases with and without the orbital motion to distinguish the effects of asymmetry. We also compared simulations between three dimensions and two dimensions. In addition, a parameter survey of changing initial orbital separations was also carried out.

Table 3.2 summarizes all our numerical simulations. The cases beginning with "MS," "RG," and "He" correspond to the MS-WD, RG-WD, and He-WDc scenarios in Table 3.1, respectively. The letter "r" represents the cases with initial orbital separation equal to the separation for RLOF (see equation 3.1); "4" and "5" are cases with initial binary separations equal to $4R_*$ and $5R_*$. The corresponding orbital speeds are calculated for initially circular orbits using Kepler's third law. The letter "N" represents cases that ignored the orbital motion and spin. The cases with "2D" are two-dimensional simulations; others are simulated in three dimensions.

Main-sequence binary companion

In Section 3.3.1, we described the case MS-Nr (see Table 3.2) for a three-dimensional simulation with the MS-WD companion but without orbital motion or spin. Figure 3.6 shows a similar simulation for the case MS-r, which includes the orbital motion and spin. The simulation resembles the case MS-Nr during the first few hundred seconds, except that the tail shock is shifted and curved because the ejecta speed is much higher than the orbital speed. However, after a thousand seconds, the asymmetry becomes more obvious; most of the same features, however, can still be seen. This asymmetry will become more important for the evolution of the SNR. Including orbital motion and spin leads to a greater unbound mass by about 16%, but

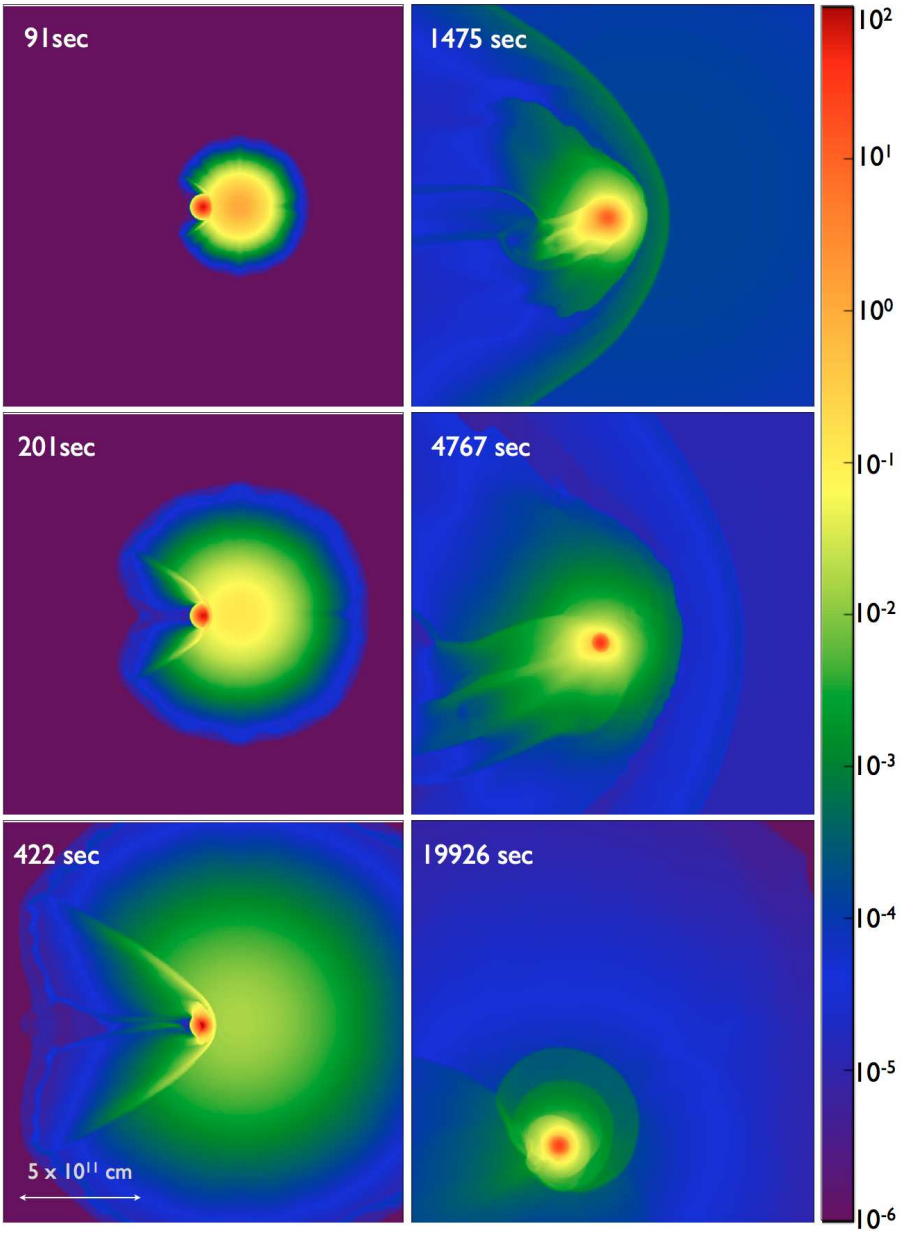

Figure 3.6: Similar to Figure 3.2, but for case MS-r; each frame reveals a portion of the domain spanning $30R_*$.

the kick velocity remains the same. The additional unbound mass may be due to the spin; the rotational energy makes fluid elements easier to unbind. However, the momentum lost in this additional mass may not change the center-of-mass velocity. A more detailed description and explanation is given in Section 3.4.1.

Red-giant binary companion

The evolution of gas density for the RG-WD companion model is shown in Figure 3.7 (RG-Nr, without orbital motion) and Figure 3.8 (RG-r, with orbital motion). The asymmetric effect is insignificant for the RG companion, because the orbital speed is much lower than the ejecta speed.

Unlike the MS star, almost all the envelope ($> 95\%$) of the RG is removed during the initial impact. Although the ejecta speed is smaller than for the MS-WD companion when it reaches the RG, the greater extent and lower binding energy of the RG makes it difficult to survive the SN Ia explosion. As a result, most of the momentum from the SN ejecta is transferred to the unbound mass, creating only a tiny kick on the RG core (less than 30 km/sec). The bow shock has an opening angle of about $40^\circ - 45^\circ$ with respect to the $x-$axis. For the RG-r case, a spiral pattern appears due to the combination of fallback and spin about 5 days after the SN Ia explosion. The reverse shock also is weaker than in the MS-WD scenario. We can only report a lower limit of the final unbound mass: the core of the RG is represented by a particle cloud and the mass of the particle cloud is not lost in our simulation.

Helium star binary companion

The He-WDc companion has the most dramatic impact and is the most compact companion in comparison to the MS-WD and RG-WD cases. Figure 3.9 and Figure 3.10 show the evolution of gas density in the orbital plane for the He-Nr and He-r cases. The opening angle of the bow shock is about $30^\circ - 35^\circ$. Because the orbital speed is higher than in the MS-WD and RG-WD scenarios, asymmetric effects due to the orbital motion appear earlier (within the first few hundreds of seconds).

After the initial impact, the compressed helium star oscillates. The oscillation frequency is higher and the flow is more turbulent in comparison to the MS companion. After several hundreds of seconds, the strong velocity shear behind the helium star leads to Kelvin-Helmholtz instability. Later, the oscillation of the helium star generates shocks which interact with Rayleigh-Taylor instabilities owing to the gravity from the helium star. Therefore, at the end of the simulation, a turbulent remnant environment is obtained. Figure 3.11 shows the velocity vector field in a gas density slice at 2231 sec in the orbital plane for the case He-r. There is a global kick velocity in the lower-left direction, caused by the orbital speed and a random turbulent velocity.

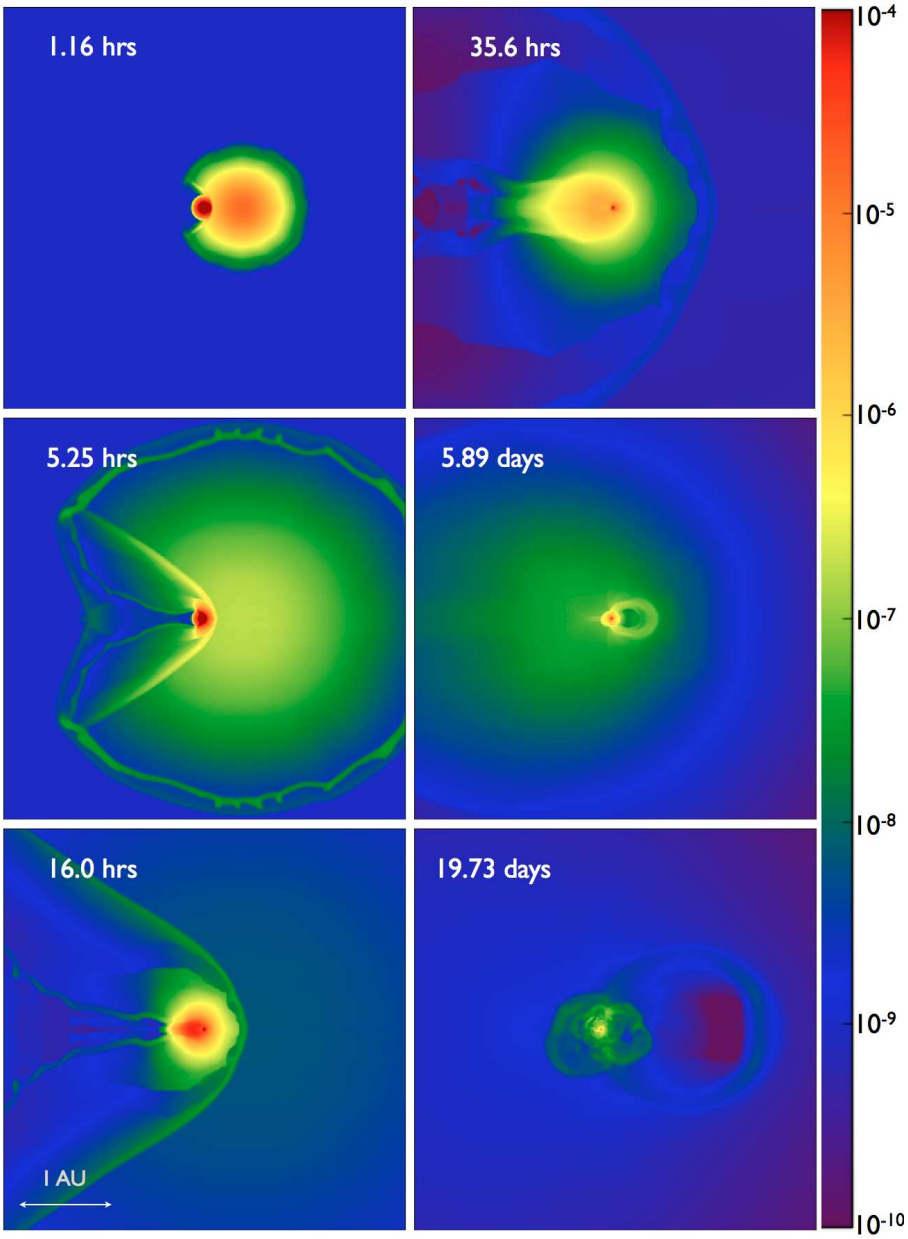

Figure 3.7: Similar to Figure 3.6, but for case RG-Nr.

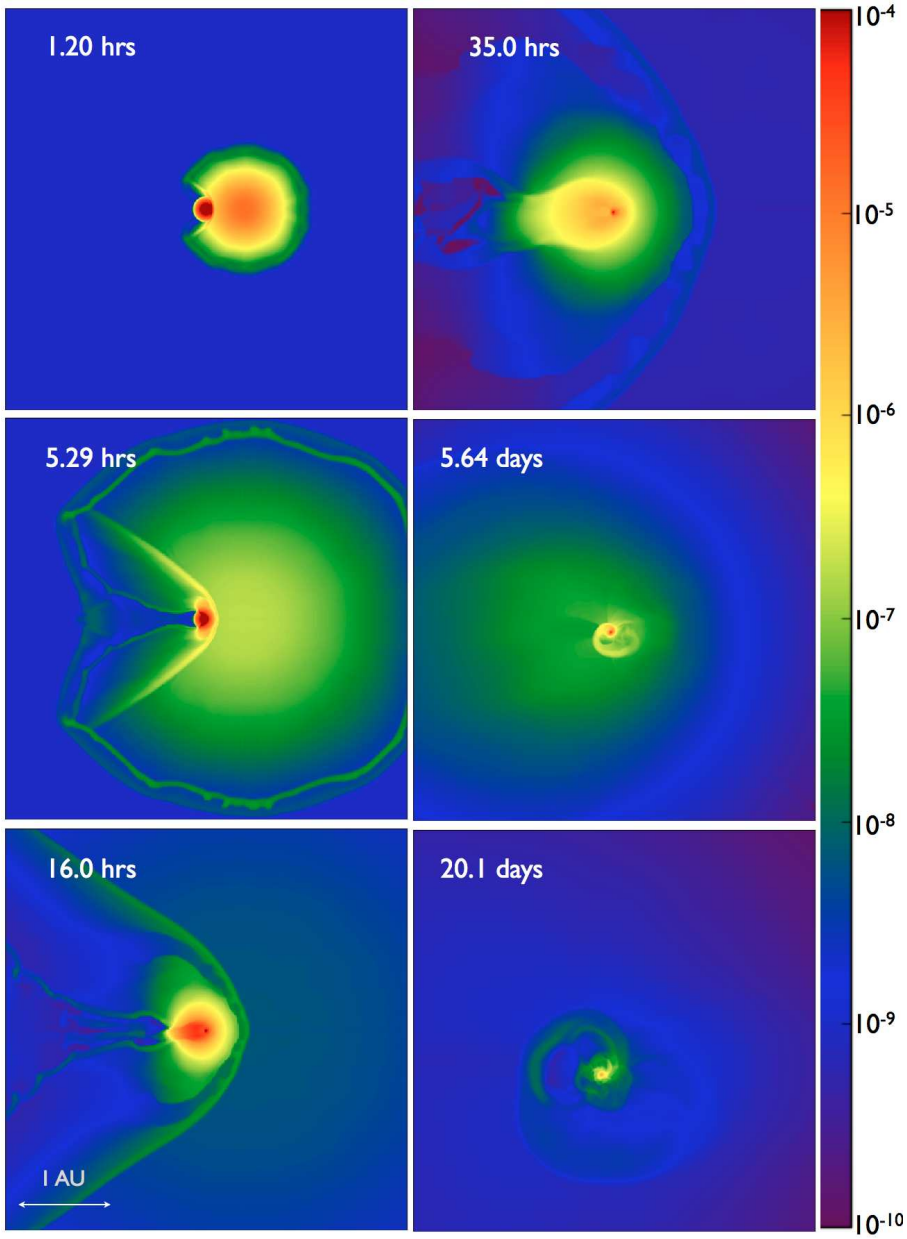

Figure 3.8: Similar to Figure 3.6, but for case RG-r.

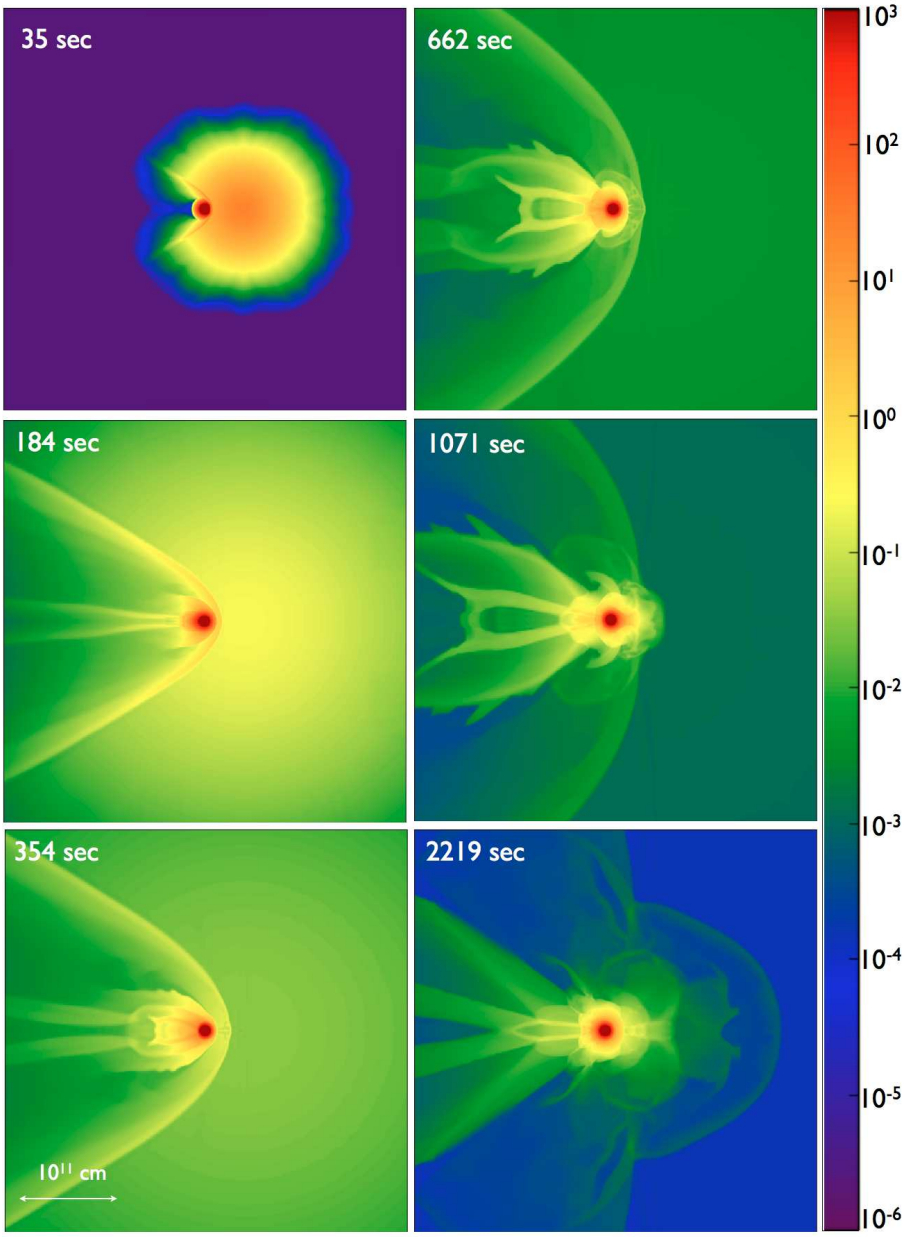

Figure 3.9: Similar to Figure 3.6, but for case He-Nr.

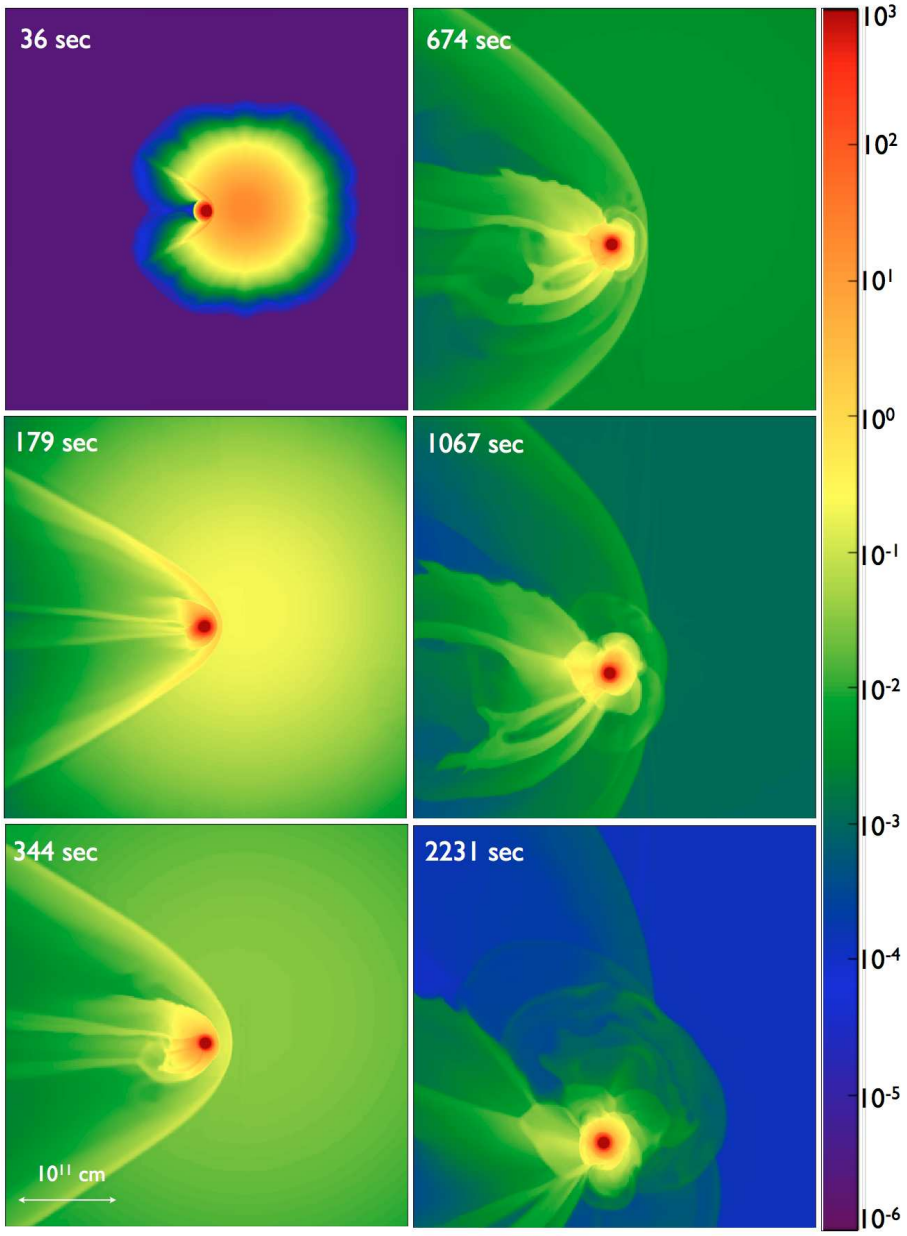

Figure 3.10: Similar to Figure 3.6, but for case He-r.

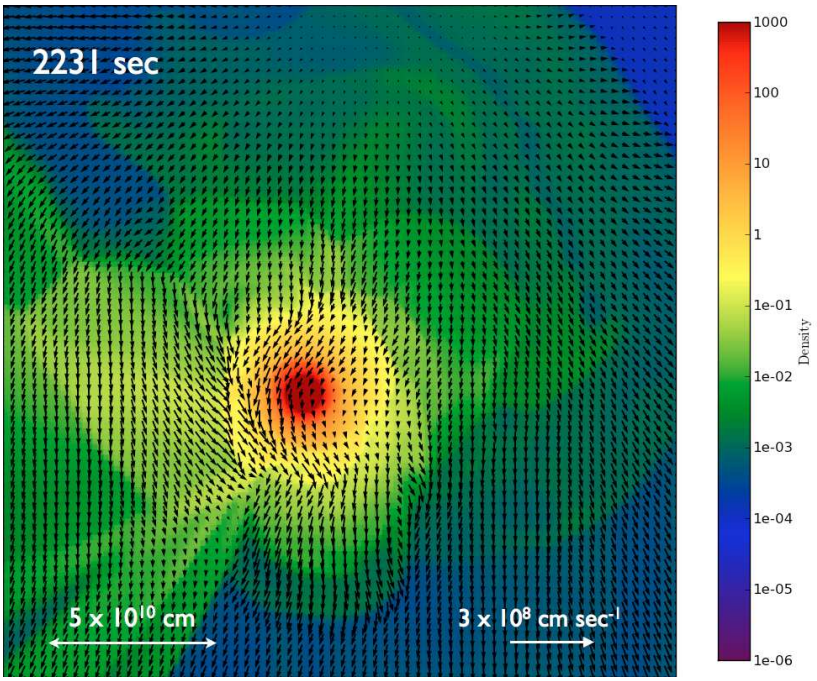

Figure 3.11: Velocity vector field around the helium star companion at 2231 sec after the SN Ia explosion in the simulation He-r. The velocity vectors are plotted every 10 zones. The white arrows reveal the scale of the domain and the scale of the velocity vectors. The color displays the logarithm of the gas density in g cm^{-3} in the orbital plane.

3.4 Discussion

3.4.1 Parameter survey

Although most SDS channels assume the binary system is in RLOF, the actual evolutionary stage and explosion conditions may differ from the model we used in our simulations. We therefore have performed a parameter survey to explore the dependence of the numerical results on varying binary separation. Significant physical quantities for each run are summarized in Table 3.2.

Figure 3.12 and Figure 3.13 show the final unbound mass and companion kick velocity as functions of the binary separation in units of companion radius. Note that the unbound masses for the RG-WD scenario are only lower limits, because the unbound mass is still increasing at the end of these simulations. In addition, the core of the RG is represented by a rigid particle cloud for which the mass is assumed to be unchanged during the simulation. Therefore, we effectively ignored interactions such as mass stripping and ablation on the core of the RG. The companion kick velocity can be derived from the difference between the companion center-of-mass velocity at the end of a simulation and the velocity at the time when the ejecta reached the companion star in that simulation.

In general, the final unbound mass and kick velocity decrease when increasing the binary separation. We

find that the final unbound mass, δM_{ub}, can be described by the relation

$$\delta M_{\rm ub} = C_{\rm ub}(a/R_*)^{m_{\rm ub}} M_\odot, \tag{3.4}$$

where a is the orbital separation, $m_{\rm ub}$ is the power-law index, and the constant $C_{\rm ub}$ depends on the companion model (see Table 3.3). All the companion models we used could be described with this power-law relation; the power-law indices, however, are different for different companion models.

Although the initial binary separation is the smallest for the He-WD scenario, suggesting the impact of the SN ejecta for this scenario should be the largest, the He star is more compact and has a higher binding energy than the MS star or RG. Therefore the amount of unbound mass is smallest in the He-WD scenario. In the RG-WD scenario, the gravitational force acting on the core region is only approximate since the softening length in the particle cloud representing the core is comparable to the size of the remaining envelope. However, most of the envelope is lost with at least $75\% - 96\%$ ejected depending on the binary separation.

For the MS-WD scenario, the difference between two-dimensional and three-dimensional runs varies from 3%, for the smallest binary separations, to 10%, for the largest binary separations. The error in the unbound mass is usually higher for the larger binary separations because the unbound mass decreases by a power-law relation with a high power-law index. The results between 2 and 3 dimensions in the He-WD scenario are even larger than in the MS-WD scenario. The uncertainty arises not only from the low percentage of unbound mass for the He star, but also from the high amount of turbulence seen in these models. Pan et al. (2010) demonstrated that the effect of the turbulence precludes convergence of the unbound mass no matter the spatial resolution and leads to a 14% error for the He-WD scenario in the two-dimensional simulations.

By including the orbital motion and spin, the MS-WD scenario loses 16% more mass for the MS-r run and 4% for the MS-5 run. The additional mass lost may not be accurate for runs with large separations: the mass loss decreases dramatically at larger separations. Other uncertainties associated with the spatial resolution (or the gravitational potential in the binary system) may be comparable to the percentage of mass difference in runs characterized by large separations. In general the orbital motion should not change the binding energy significantly if the binary separation is larger than the Roche separation. In addition, the orbital speed is much smaller than the SN ejecta speed. Thus, orbital motion should not have much effect on the impact of the explosion, instead simply providing a constant velocity for the companion star. However, the spin of the companion may have a stronger influence. Adding rotational energy to the companion star should make its envelope's binding energy lower. This addition may explain the extra mass lost in our

Table 3.3: Power-law indices for the final unbound mass and kick velocity.

Model	$m_{\rm ub}^{\rm a}$	$\log_{10} C_{\rm ub}^{\rm a}$	$m_{\rm kick}^{\rm b}$	$\log_{10} C_{\rm kick}^{\rm b}$
MS	-3.61	0.894	-1.76	2.83
MS-N	-3.46	0.757	-1.69	2.78
MS-2D-N	-3.66	0.859	-1.88	2.89
RG	-0.391	-0.0103	–	–
RG-N	-0.416	0.00269	–	–
He	-3.04	-0.260	-2.62	3.02
He-N	-2.92	-0.381	-2.83	3.17
He-2D-N	-3.36	-0.245	-4.6	3.9

[a] The power-law index, $m_{\rm ub}$, and constant, $C_{\rm ub}$, described in equation 3.4.

[b] The power-law index, $m_{\rm kick}$, and constant, $C_{\rm kick}$, described in equation 3.5.

simulations that include spin. Figure 3.14 shows the distribution of the ratio of rotational energy density and binding energy density in the $x-z$ plane. The rotational energy density in the back and front region of the companion star is $\sim 3\%$ of the binding energy density at $R \sim 0.8 R_*$. When compared with the unbound region in Figure 3.15, there is evidence of some overlap of the unbound mass with the high rotational-energy density region. Therefore, the spin of the companion should broaden the unbound mass region.

The simulation data from Marietta et al. (2000) and Pakmor et al. (2008) are also plotted and compared in Figure 3.12. Although the MS companion model in Marietta et al. (2000) is different from that used here, the general behavior of their results is consistent with ours. Pakmor et al. (2008) have a MS star model that resembles ours but is slightly larger. The power-law relation for the final unbound mass versus separation provided by Pakmor et al. (2008) also is consistent with our MS-WD scenario.

Leonard (2007) studied the spectra of two SNe Ia (SN 2005am and SN 2005cf) in order to search for the Hα emission that may emerge from the unbound hydrogen-rich companion mass. He relied on the data from the two SNe and coupled the modeling results of Mattila et al. (2005) and the final unbound mass in Marietta et al. (2000) and Meng et al. (2007), providing an estimated upper limit of 0.02 $M_\odot$ for the amount of solar abundance material that may have remained undetected. In contrast, the mass loss for our cases in RLOF are all greater than these limits, except for the He-WDc scenario. However, the limits should depend on the actual evolutionary stage of the companion candidate. If the upper limit is correct, SN 2005am and SN 2005cf may result from a more compact binary companion or from the DDS.

Similarly, the kick velocity versus binary separation can also be described by a power-law relation,

$$\delta v_{\rm kick} = C_{\rm kick} (a/R_*)^{m_{\rm kick}} {\rm km\ s^{-1}}, \tag{3.5}$$

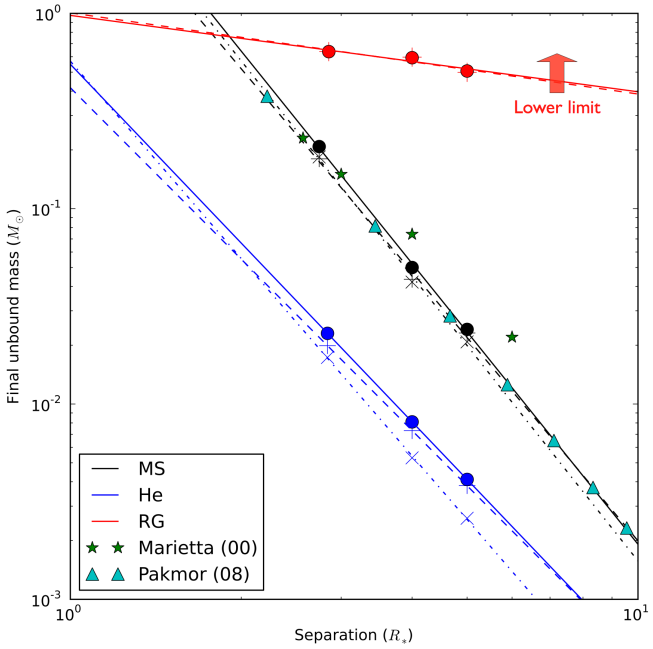

Figure 3.12: Final unbound stellar mass vs. binary separation for different companion models. Each color represents data for a type of companion model: black represents simulations for the MS-WD scenario; blue, the He-WDc scenario; and red, the RG-WD scenario. The separation is expressed in units of the companion radius. Lines show fitted power-law relations based on the numerical simulation results (the red line shows the lower limit of the RG-WD scenario). The "+" symbols and dashed lines indicate 3D data without orbital motion; "o" symbols and solid lines present 3D data with orbital motion; and "x" symbols and dashed dot lines demonstrate 2D data without orbital motion. Star symbols show the data from Marietta et al. (2000) for the HCV model. Triangles indicate the power-law relation for a MS binary companion from Pakmor et al. (2008).

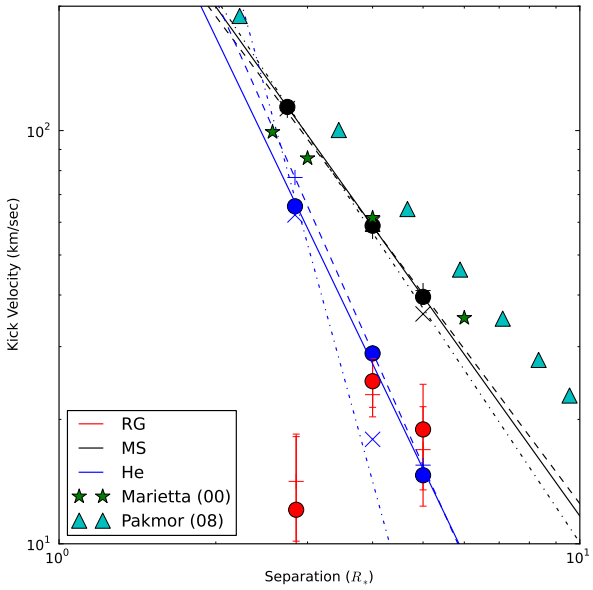

Figure 3.13: Similar to Figure 3.12, but for kick velocity vs. binary separation in different companion models.

where $m_{\rm kick}$ is the power-law index, and $c_{\rm kick}$ is a constant depending only on the companion model (see Figure 3.13). The power-law indices and constants for the final unbound mass and kick velocity are summarized in Table 3.3. For the RG-WD scenario, because the simulation domain is of a very large scale, the error in kick velocity is comparable to the value we deduced. Therefore, we can only provide an upper limit on the kick velocity of about 40 km/sec.

If we include the orbital motion and spin, they only produce about a 2% difference in the kick velocity, which suggests that the orbital motion and spin are unimportant to the momentum transfer between ejecta and companion.

Although our final unbound mass is consistent with Pakmor et al. (2008), the kick velocity we determined is lower than the kick in Pakmor et al. (2008). This result may be due to the lack of a reverse shock in the SPH simulations: the reverse shock carries some momentum away from the SN ejecta, consequently making the companion kick smaller.

3.4.2 Stripped and ablated mass

The unbound mass could be either due to ablation (heating) or to stripping (momentum transfer), depending on the energy of the SN ejecta and the binding energy of the companion. Quantitatively determining the ablated and stripped mass requires a method to trace the fluid elements in Lagrangian coordinates. This

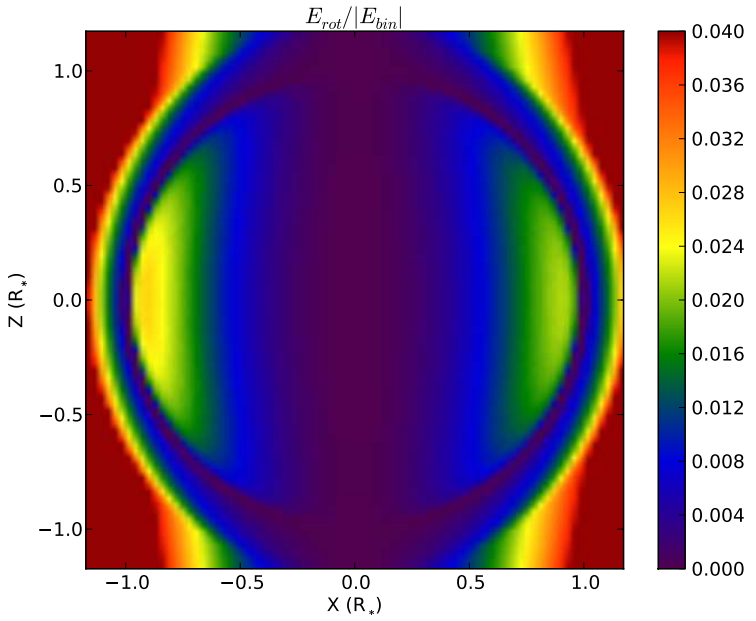

Figure 3.14: The distribution of the ratio of the rotational energy density and binding energy density in the $x-z$ plane for the MS-r run. The region is rescaled to the units of the companion star ($R_* = 5.51 \times 10^{10}$ cm).

method can be implemented in FLASH using passive particles. We create an additional particle property for each passive particle and then label its gravitational-binding status as bound, ablated, or stripped. 10^6 passive particles are randomly distributed, with particle density proportional to the gas density. All passive particles are initialized as bound and then the gravitational-binding status in each timestep is recalculated. Particles in zones with negative total energy ($E_{\rm tot} = E_{\rm grav} + E_{\rm kin} + E_{\rm thermal}$) are considered to be bound; otherwise, we mark passive particles in zones as ablated (stripped) if the thermal energy is larger (smaller) than the kinetic energy. Ablated and stripped particles possibly become bound again in the subsequent timesteps, but they are not allowed to switch from one state to the other.

Figure 3.15 illustrates the initial distribution of passive particles colored by their gravitational-binding status in the $x-z$ plane. At 144 seconds (upper panel), particles on the front side of the companion are all ablated as a result of the initial impact. The MS star companion is compressed and ablated to the initial radius of $\sim 0.4R_*$. This result corresponds to the first peak of the unbound mass ($\sim 0.2M_\odot$) in comparison to the simulation time in Figure 3.5. Next, the reverse shock, traveling in the positive $x-$ direction, thins the unbound layer to $\sim 0.5R_*$ and decreases the unbound mass. Following this decrease, the companion is surrounded by the ejecta while mass around the surface and in the tail region becomes unbound again (lower panel at 1060 sec), eventually increasing to $0.21M_\odot$ at the end of the simulation (Figure 3.5). This non-monotonic behavior of changing unbound mass in time also has been seen by Pakmor et al. (2008)

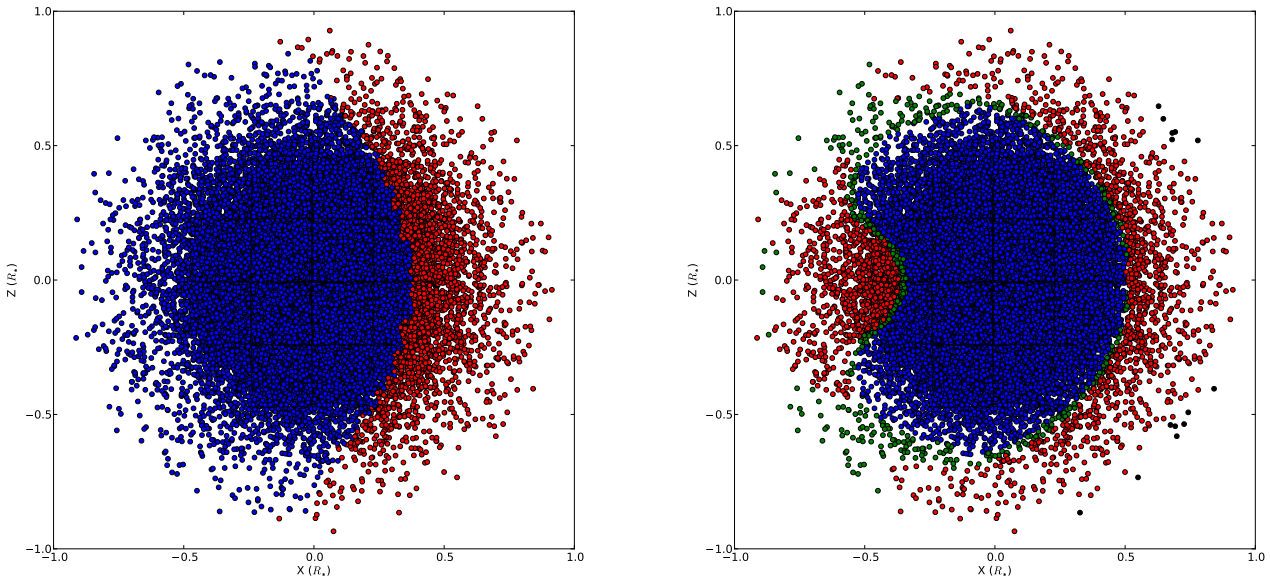

Figure 3.15: Initial position of passive particles in the $x - z$ plane. Particles are plotted within a slice of thickness equal to three zones. The axes are scaled to the radius of the companion star ($R_{\rm MS} = 5.51 \times 10^5$ km). Colors represent the gravitational binding status at $t = 144$ sec (upper) and $t = 1060$ sec (lower) for the case MS-r (see Table 3.2): blue for bound; red for ablated; green for stripped; and black for particles already gone from the simulation box at that time. The black grids between particles reveal some numerical artifacts in particle initialization, but this artifact does not alter the dynamics of the fluid or the tracer particles. A detailed explanation and calibration are given in Section 3.4.2.

in their SPH simulations. They, however, do not examine the unbinding process at early stage and their non-monotonic behavior is relatively weak. Therefore, they deemed it to be a numerical artifact in their convergence study. However, it is difficult to definitively show that the non-monotonic behavior is numerical in origin.

In contrast to the MS-WD scenario, Figure 3.16 and Figure 3.17 reveal similar distributions for the He-WD scenario and the RG-WD scenario. The He-WD scenario's behavior resembles the MS-WD scenario, but mass is only ablated in the leading surface region. More stripped mass in the tail region results from the high turbulence around the He star. The dramatic impact and turbulence make momentum transport more efficient. In the RG-WD scenario, almost all the envelope is ablated during the initial impact; only a small amount of mass ($\sim 0.007 M_{\odot}$) is stripped. Later on, some mass around the core region becomes bound again after the RG is compressed. After the impact, the bound mass slowly increases because of fallback.

The amount of ablated and stripped mass can be calculated by counting the ablated and stripped particles. Non-interacting passive particles do not affect the accuracy of the subsequent time evolution because passive particles simply move in Lagrangian coordinates without interacting with fluids. However, the initialization of passive particles in our setup was found after our simulations to have some numerical artifact related to block boundaries. This grid-shaped artifact can be seen in Figure 3.15. Therefore, a weighting factor for the ablated/stripped mass due to each particle is necessary when calculating the total particle mass.

We calculate the particle weights by evaluating the difference between particle density and gas density in each zone for the initial conditions. Thus, the particles in any given zone have the same weight. However, in low-density regions, some zones may not contain any particles; this lack may lead to another uncertainty, underestimating the total particle mass. Thus, we add this missing mass by assuming that the stripped mass to ablated mass ratio in these zones is the same as for their neighbors. After this correction, we are able to calculate the stripped mass and ablated mass for each timestep.

The stripped mass to ablated mass ratios for all the runs are summarized in Table 3.2. These values are calculated from the unbound particles at a time after the initial impact and before the unbound particles leave the simulation box. It is found that the unbound mass is mainly due to ablation in all the runs. The stripped mass to ablated mass ratio is about $0.4 - 0.7$ for the MS-WD scenario, $0.5 - 0.8$ for the He-WD scenario, and less than 0.2 for the RG-WD scenario. This result contradicts our previous results using the mixing of SN ejecta at late times in 2D simulations (Pan et al., 2010) (tracer particles are not supported in 2D). The ablation happens at the very beginning of the initial impact, but the mixing of ejecta occurs later, based on our analysis using passive particles. Thus, the mass treated as stripped in the previous study may

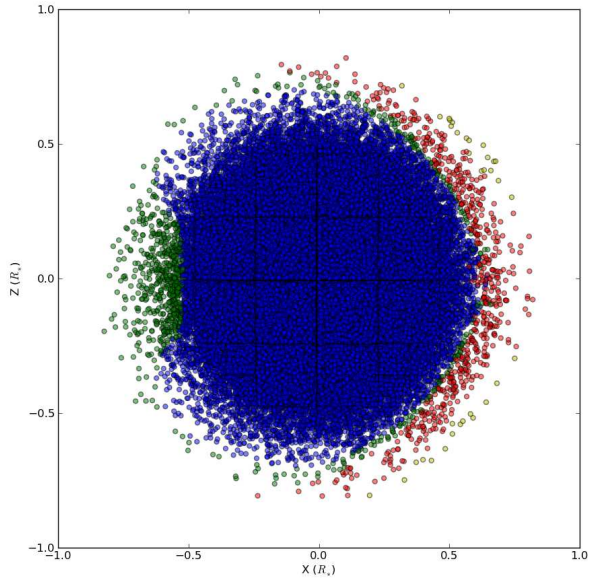

Figure 3.16: Similar to Figure 3.15, but for case He-r at $t = 265$ second.

already have been ablated during the initial impact. In addition, ablation was previously ignored in most previous analytical or semi-analytical work (Meng et al., 2007), resulting in an underestimate of the impact of SN ejecta on the binary companion.

3.4.3 Hole in the supernova remnant

In the SDS, the impact of SN ejecta not only can affect the companion star, but it also can affect the shape of the ejecta: a cone-shaped hole shadowed by the companion will break the symmetry of the ejecta. Observationally, spectropolarimetry studies reveal a continuum polarization of about $0.2\% - 0.7\%$ for normal SNe Ia and $0.3\% - 0.8\%$ for subluminous SNe Ia (Howell et al., 2001; Wang & Wheeler, 2008), implying that the asymmetry in SN Ia explosions is small but real. Recent theoretical and numerical studies suggest that the intrinsic variation in SN Ia light curves potentially results from viewing asymmetric explosions from different angles (Kasen et al., 2004; Kasen, 2010; Maeda et al., 2010; Blondin et al., 2011). Furthermore, García-Senz et al. (2012) studied the interaction of the hole, SN material, and ambient medium using SPH simulations. They conclude that the hole could remain open in the SNR for hundreds of years, suggesting the hole could affect its structure and evolution.

Figure 3.18 shows the companion-material and SN-material density distribution in the orbital plane for the MS-r, RG-r, and He-r cases. The companion material is confined mainly in the bow shock; the opening

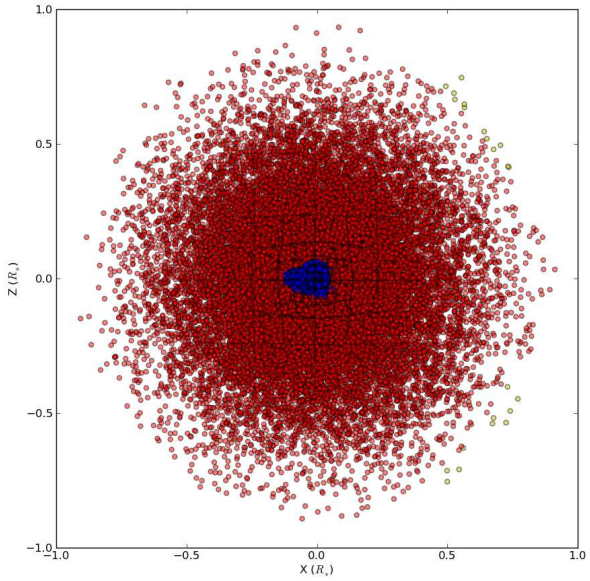

Figure 3.17: Similar to Figure 3.15, but for case RG-r at $t = 16.0$ hours.

angle of the hole is about $40° - 45°$ for the MS-r case, $45° - 50°$ for the RG-r case, and $30° - 35°$ for the He-r case. The MS star and RG companions have a similar opening angle, but the high-speed tail shock in the RG companion has the largest opening angle due to having the lowest ejecta Mach number. The high orbital speed and strong turbulence in the He-r case distort and mix the hole with more SN material than other companion models, creating a smaller hole with more fallback in the SNR.

We may also ask how the unbound hydrogen-rich material is distributed in the SNR and how this material can be detected by observations. Based on our simulations, the unbound mass is mostly confined in the hole. The velocity distribution of unbound mass is shown in Figure 3.19. The peak velocity is 550km/sec^{-1} for the MS-WD, 955km/sec^{-1} for the He-WDc, and 660km/sec^{-1} for the RG-WD. The RG companion has the largest velocity dispersion, but the peak velocity is slightly larger than the peak velocity for the MS star companion. This low outflow velocity ($< 1,000$km/s^{-1}) is much smaller than the ejecta speed ($\sim 8,000$km/s^{-1}), suggesting that the hydrogen could be hidden in the ejecta in the early-stage explosion, except when looking directly from the backside of the companion. However, it is still possible to detect it at late times when the expansion slows down and the ejecta becomes transparent.

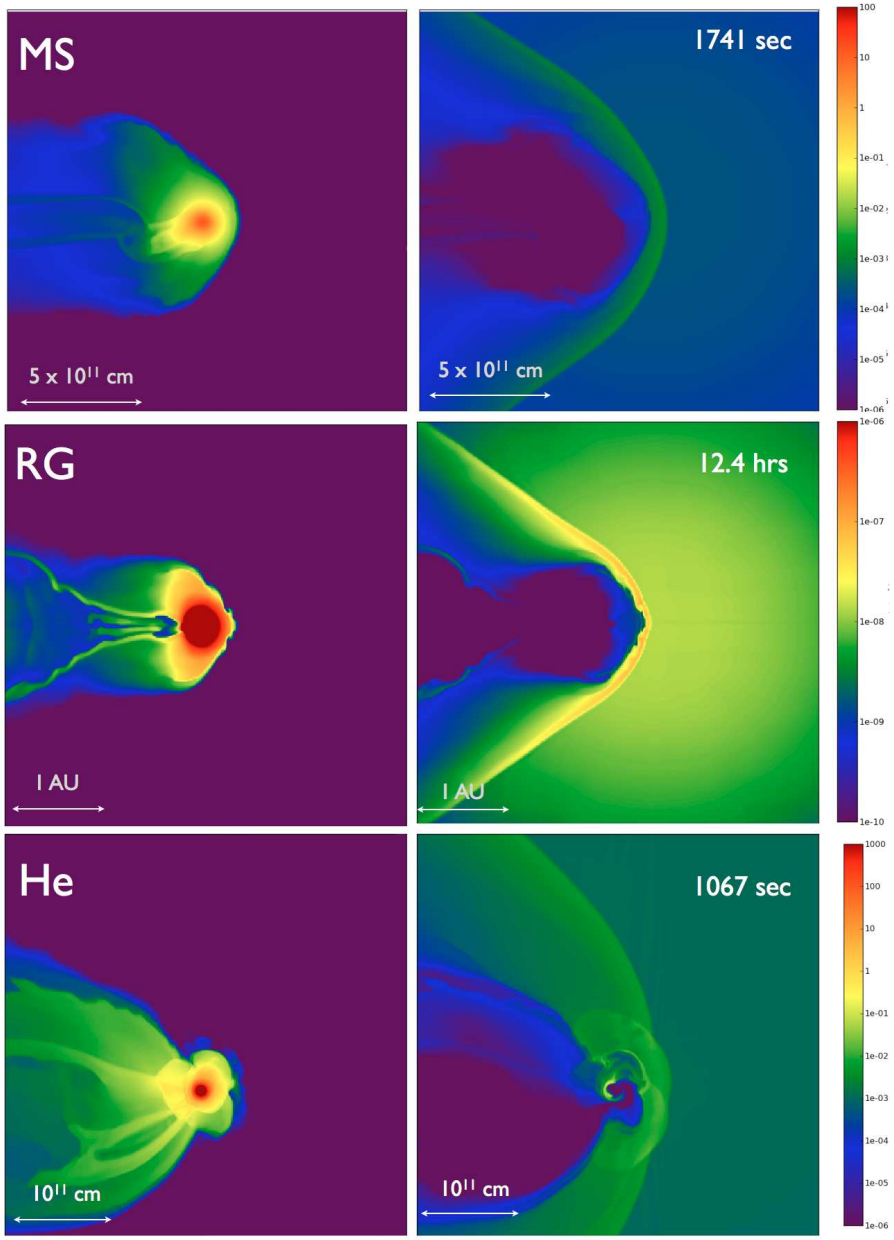

Figure 3.18: Companion and SN gas density in the orbital plane for different scenarios. The left panel displays the density of the companion material ($^1H + ^4He + ^{12}C$) and the right panel shows the density of SN material (^{56}Ni). Companion model and initial setup from the top row to the lowest row are MS-r, RG-r, He-r cases in Table 3.2.

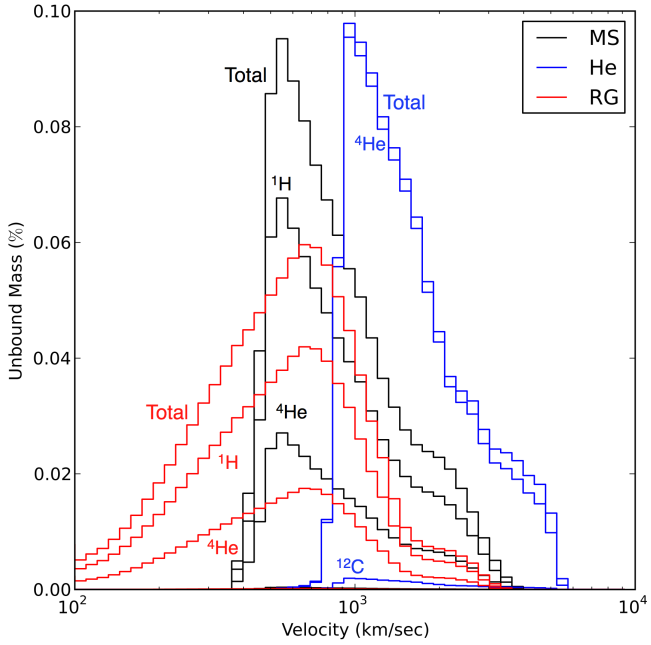

Figure 3.19: Speed distribution of unbound mass and compositions for the MS-r, RG-r, He-r cases (Table 3.2). Each color represents the speed distribution for a particular run: black represents the case MS-r; red, case RG-r; and blue, case He-r.

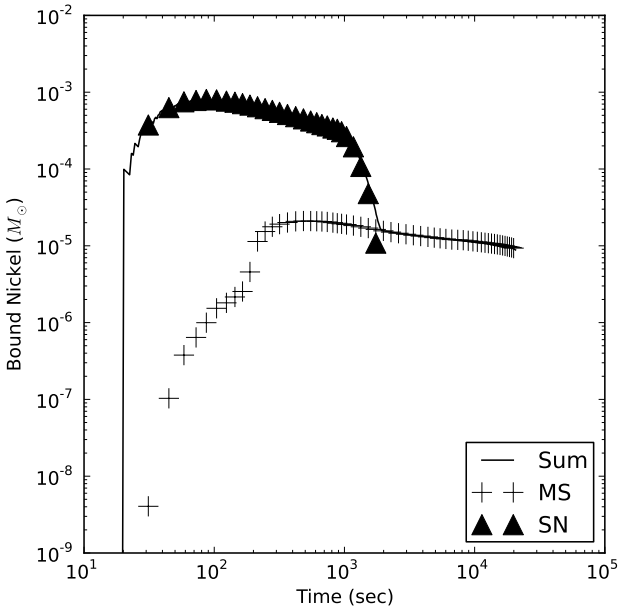

Figure 3.20: Bound nickel around the MS star companion region and the SN region. The plus sign indicates the companion region, and triangles indicate the SN region. Total bound nickel is plotted using the solid line.

3.4.4 Nickel contamination

The companion star could be contaminated by the SN ejecta in its envelope during the initial impact or as fallback at late times. If the mixing of SN ejecta occurs mainly in the companion's envelope, the contamination provides one possibility for detecting iron abundance from the remnant star after the nickel radioactively decays. Since we use nickel as a tracer for the SN Ia ejecta in our simulations, we could estimate the nickel contamination in the remnant star in a SNR by calculating the amount of bound nickel after the SN Ia explosion. Following the same method as that used to determine the bound mass, we can calculate the amount of bound nickel by summing the ejecta material that cannot escape the gravitational potential. There are essentially two bound regions in the simulations: the region around the post-impact companion star and the region at the explosion center, separated by the reverse shock. The bound nickel in the SN region likely results from the fact that the some of the nickel is bound to the system in the initial setup due to the presence of the companion star. We assume that the bound nickel in the companion star more likely reveals the nickel contamination.

Figure 3.20 illustrates the amount of bound nickel in these two regions for the case MS-r. The bound nickel is dominated by the SN region at the beginning and then reaches a peak of $\sim 10^{-3} M_{\odot}$ at about ~ 80 sec. However, after the interaction between the reverse shock and the SN region, the bound nickel in the SN region becomes unbound and eventually disappears after around $2,000$ sec. The remaining bound nickel in the MS star companion is $\sim 10^{-5} M_{\odot}$. In general, increasing the initial binary separation leads to a greater contamination because a slower ejecta speed makes it more difficult for ejecta material to escape; a larger separation, however, leads to a smaller companion cross-section, thereby blocking less SN material. Thus, a simple variation for the nickel contamination with the binary separation is not found. All the results are consistent to within an order of magnitude with a value of $\sim 10^{-5} M_{\odot}$. Orbital motion and spin only introduce a minimal effect. This amount of nickel contamination is significantly less than the previous estimate by Marietta et al. (2000) for the HCV scenario (an upper limit of $10^{-3} M_{\odot}$) because the interaction of the reverse shock.

Figure 3.21 shows the nickel contamination for the RG companion, the RG-r case. In this example, the bound nickel in the SN region only exists for a very short time at about 10^5 sec after the explosion. There are two bumps of bound nickel around the RG region. The first bump, at about $\sim 4,000$ sec, is related to the initial impact of the SN Ia explosion. Bound nickel reaches the first peak when the shock compresses the leading surface of the RG, and then it decreases when the reverse shock passes through it. The second bump occurs later at about $\sim 10^5$ sec in a region at the back side of the RG while the compressed RG relaxes. The nickel contamination for the case RG-r is about $10^{-8} \sim 5 \times 10^{-8} M_{\odot}$.

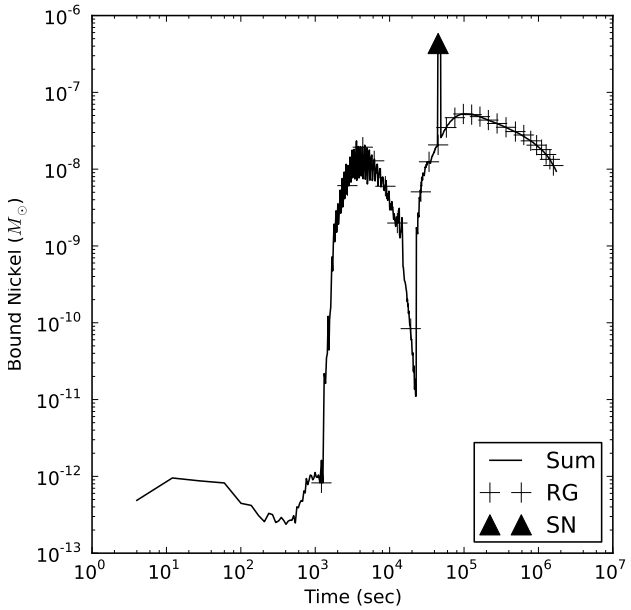

Figure 3.21: Similar to Figure 3.20, but for RG binary companion. Note that there is only one triangle data point for SN region because the duration of this region is short. We have only one checkpoint file during that time.

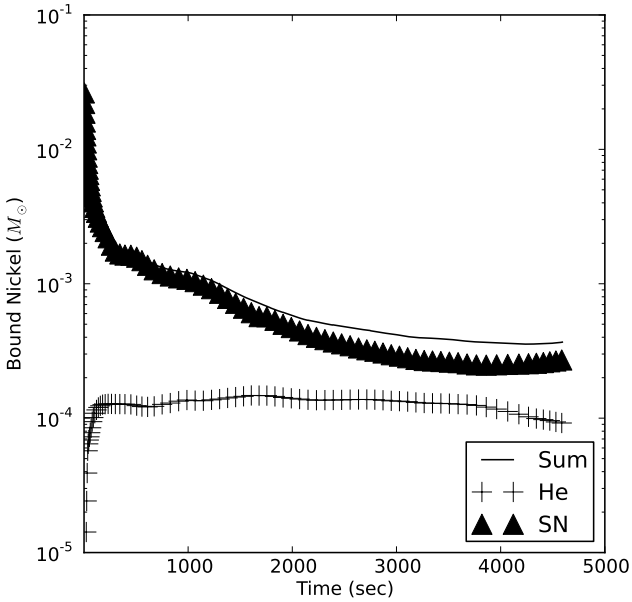

Figure 3.22: Similar to Figure 3.20, but for helium star binary companion.

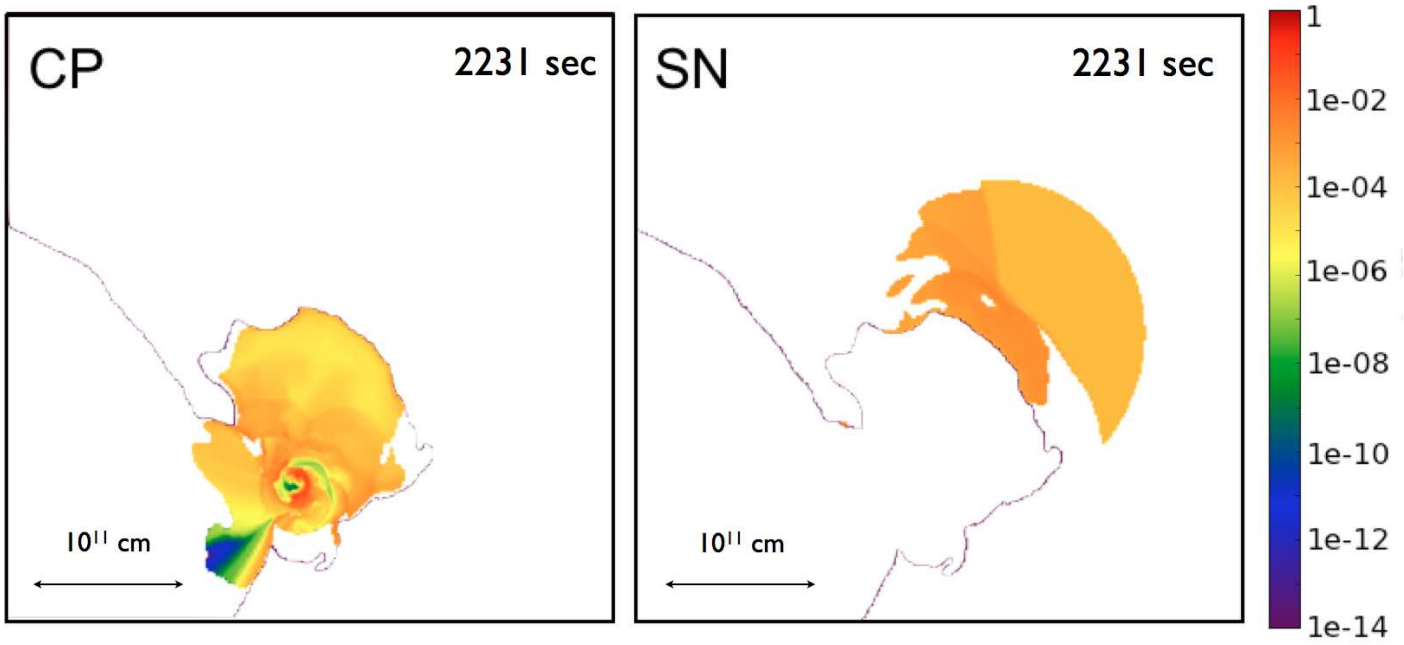

Figure 3.23: Bound nickel density distribution in the orbital plane around the helium star companion (left) and the SN region (right). The black line describes the boundary between the companion material region and the SN material region. The color scale indicates the logarithm of the nickel density in g cm^{-3}.

Similarly, Figure 3.22 shows the nickel contamination for the helium star companion (case He-r). The nickel contamination in the He star region stays around $\sim 10^{-4} M_\odot$ for the whole simulation, but in the SN region it decreases from $10^{-3} \sim 10^{-2} M_\odot$ to $\sim 3 \times 10^{-4}$. Unlike the MS star cases, the bound nickel in the SN region does not disappear at the end of the simulation while interacting with the reverse shock. It is more likely that the bound nickel in the SN region will merge eventually with the He star region at late times, resulting in a total contamination of $\sim 4 \times 10^{-4} M_\odot$. Figure 3.23 shows the bound nickel density in the orbital plane at $2,231$ sec for these two regions; at that time, the two regions are already mixed with each other.

If the nickel contamination is restricted to the envelope of the companion star, we can estimate the nickel to hydrogen plus helium ratio by using the bound nickel and the envelope mass (Pan et al., 2010). We define the envelope radius using the extreme in second derivative of the companion gas density with respect to the radius in the initial conditions. Thus, the envelope mass is the mass outside this envelope radius. If we assume the unbound mass is entirely from the envelope (Figure 3.15), then the final envelope mass is the difference between the initial envelope mass and the final unbound mass in Table 3.2. However, we note that the envelope mass ($\sim 0.3 M_\odot \pm 0.1 M_\odot$) we estimate for the MS star companion is close to the final unbound mass ($\sim 0.2 M_\odot$); thus for this case we only can provide an order of magnitude estimate. The

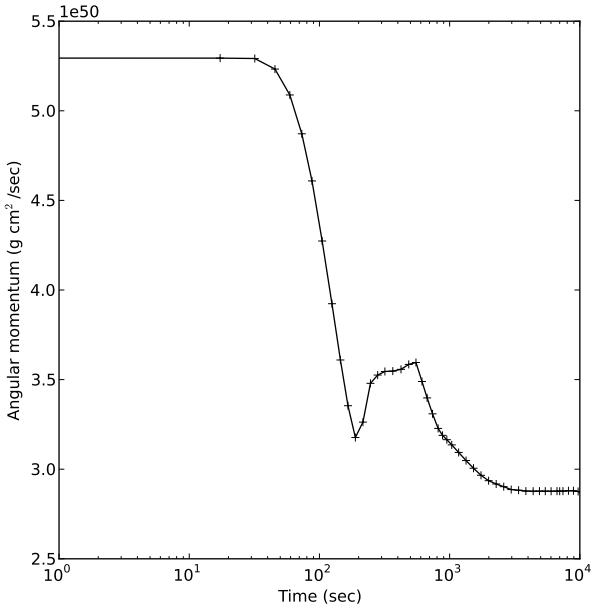

Figure 3.24: Angular momentum versus simulation time for the MS-r case. The angular momentum is calculated in the companion center of mass frame and only considers the bound companion gas.

estimated upper limit for the ratio of nickel to hydrogen plus helium is about 10^{-4} for the MS-WD, 10^{-3} for the He-WDc, and $2 \times 10^{-5} - 10^{-6}$ for the RG-WD scenario. The solar ratio from Anders & Grevesse (1989) is about 5×10^{-4}, which is similar to or slightly smaller than the results in our simulation values, suggesting a possible probe to identify the progenitor candidate in a SN Ia SNR.

3.4.5 The remnant companion star

At the end of our simulations, all the companion stars have survived the impact of the SN Ia explosion. The post-impact velocity of the remnant star will be the original orbital velocity plus the kick velocity. In general, this velocity should be larger than the velocities of background stars. In our simulations, the kick velocity contributes up to 45% of the final net velocity for the MS-r case, 13% for the He-r case and $< 50\%$ for the RG-r case. Therefore if the binary systems in the SDS are in RLOF, then the final velocity including kick and orbital speed will provide information in the search for the progenitor star in the SNR.

Ruiz-Lapuente et al. (2004) observed stars near the remnant center in Tycho's SN. They found a star named Tycho G which has a higher radial velocity (108 ± 6km s^{-1}, in the local standard of rest) than other background stars at the corresponding distance ($20 - 40$ km s^{-1} at $2 - 4$ kpc), suggesting Tycho G could be the non-degenerate remnant star resulting from the SDS. Tycho G is a slightly evolved star with a stellar type G0-G2, mass $M \sim 1 M_\odot$, radius $R \sim 1 - 3 R_\odot$, and effective temperature $T_{\rm eff} = 5,750$ K. Thus, if it

is indeed a remnant, the progenitor star was likely a MS star. Although our simulation is not set up for Tycho's SN, the MS-r case resembles it. The final net velocity of our MS-r case is 277km s^{-1}, which covers the value of Tycho G. If the remnant star in Tycho's SN has not changed significantly since the SN explosion, the property of our post-impact companion may provide further information for identifying the progenitor star of Tycho's SN. The post-impact central density, temperature, and pressure in our simulation for the MS-WD model are 24 g cm^{-3}, 7.8×10^6 K, and 2.7×10^{16} dyne cm^{-2}, which are consistent with the values in Marietta et al. (2000).

As Meng & Yang (2011) pointed out, the rotational velocity of the remnant star could be an important diagnostic for the Tycho G star as the companion candidate in Tycho's SN with the SDS. In their model, the mass, space velocity, radius, luminosity, and effective temperature of the remnant star are consistent with observations by Ruiz-Lapuente et al. (2004) and Kerzendorf et al. (2009), but not the rotational velocity. The rotational velocity observed by Kerzendorf et al. (2009) is only 7.5 ± 2 km s^{-1}, but the predicted rotational velocity in Meng & Yang (2011) is ~ 100 km s^{-1}. However, Meng & Yang (2011) ignore the impact of the SN ejecta on the companion star and assume the remnant star did not change at the onset of the SN Ia explosion. Our simulation shows that about 18% of the mass is lost in the MS-r case, suggesting that the angular momentum of the remnant star also should decrease after the impact.

Figure 3.24 shows the change of angular momentum versus simulation time in the companion center of mass frame. After the impact, the MS companion loses 48% of its initial angular momentum (6% for the He-r case and $\sim 99\%$ for the RG-r case), but only loses 18% of the mass. If the angular momentum, $J = \alpha M_* R_*^2 \omega_*$, has a constant α after the impact of SN explosion, then α can be calculated using the angular momentum from the initial conditions ($\alpha = J_0/(M_* R_* \omega_*) = 0.251$). However, the post-impact radius of the companion is not straightforward to define, because the remnant companion star is not in hydrostatic equilibrium and the location of the photosphere is unclear. We can estimate the equilibrium radius of the remnant star in the case MS-r using the virial theorem, $R_{\rm remnant} \sim GM^2/E_{\rm int} = 1.6 \times 10^{11}$ cm$= 2.4 R_\odot$. Therefore, the post-impact rotational velocity can be calculated from the post-impact R', M' and J' to obtain $v_r' \sim 37$ km s^{-1}, which is only 23% of the initial rotational velocity ($v_{r,0} = R_* \omega_* = 164.4$ km s^{-1}). However, the virial theorem and constant α assume hydrostatic equilibrium, and Tycho's SN is only 439 yr old. The real R' should be larger, causing a lower rotational velocity for the post-impact companion star. This result provides additional support for the interpretation of Tycho G as the candidate for the progenitor star in Tycho's SN with the SDS.

In contrast, the luminosity and surface temperature of the He star in the He-WD scenario are about $1.3 \times 10^2 L_\odot$ and 4.4×10^4 K, which are too high to be consistent with the candidate progenitor for the

Tycho's SN. This would also be the case for the RG-WD scenario since the luminosity of the remnant is expected to be comparable to its RG progenitor, which must be sufficiently luminous. This is required in the SDS model in order that the mass transfer rate prior to the SN explosion be greater than $\sim 10^{-7} M_{\odot} yr^{-1}$ such that the CO WD accumulate sufficient matter to reach the Chandrasekhar limit.

3.5 Conclusions

We have investigated the impact of SN Ia ejecta on companion stars in the single-degenerate scenario via three-dimensional hydrodynamical simulations. We studied possible binary companion models, including a MS star, a RG and a He star, and considered the effects of asymmetry introduced by orbital motion and spin. A detailed setup of the sub-grid SN Ia explosion using the W7 model in Nomoto et al. (1984) also is described. It is found that the orbital motion and spin lead to $\sim 16\%$ more unbound mass in the MS star companion channel but do not significantly affect the kick velocity. Furthermore, the orbital motion and spin play an important role in determining the morphology of the SNR. A power-law relation between the unbound mass and initial binary separation is found for all companion channels and is consistent with previous studies. Similarly, the kick velocity can be fitted by a power-law for the MS and He star binary companions. For the RG companion, we can only report a 40 km s^{-1} kick as an upper limit due to numerical uncertainty. By using the technique of passive particles, we find that the unbound mass is dominated by ablation instead of stripping. This result is in conflict with previous understanding, in which ablation was ignored in previous analytical studies. In addition, a hole shadowed by the ejecta is found to break the symmetry of the SNR. The amount of nickel contamination of the companion star is found to be $\sim 10^{-5} M_{\odot}$ for the MS star companion, $\sim 10^{-8} M_{\odot}$ for the RG companion, and $\sim 10^{-4} M_{\odot}$ for the He star companion. The corresponding nickel/iron to hydrogen plus helium abundance ratio may be useful for identifying the progenitor candidate in SN Ia remnants in future observations. We also find that the post-impact companion star loses about half of its initial angular momentum for the MS-WD scenario with the rotational velocity decreasing to 23% of its initial rotational velocity, providing added support for the SDS model for the Tycho SN.

Chapter 4

Evolution of Post-Impact Remnant Stars in SN Ia Remnants within the Single-Degenerate Scenario[†]

Abstract

The nature of the progenitor systems of Type Ia supernovae is still uncertain. One way to distinguish between the single-degenerate scenario (SDS) and double-degenerate scenario (DDS) is to search for the post-impact remnant star. To examine the characteristics of the post-impact remnant star, we have carried out three-dimensional hydrodynamic simulations of supernova impacts on main sequence-like stars. We explore the evolution of the post-impact remnants using the stellar evolution code MESA. We find that the luminosity and radius of the remnant star dramatically increase just after the impact. After the explosion, post-impact companions continue to expand on a progenitor-dependent timescale of $\sim 10^{2.5-3}$ yr before contracting. It is found that the time evolution of the remnant star is dependent on not only the amount of energy absorbed, but also on the depth of the energy deposition. We examine the viability of the candidate star Tycho G as the possible remnant companion in Tycho's supernova by comparing it to the evolved post-impact remnant stars in our simulations. The closest model in our simulations has a similar effective temperature, but the luminosity and radius are twice as large. By examining the angular momentum distribution in our simulations, we find that the surface rotational speed could drop to ~ 10 km s^{-1} if the specific angular momentum is conserved during the post-impact evolution, implying that Tycho G cannot be completely ruled out because of its low surface rotation speed.

4.1 Introduction

Type Ia supernovae (SNe Ia) are important as cosmological distance probes and sources of metal enrichment for the interstellar medium. Although they can be treated as "standardizable candles," intrinsic variations in SN Ia properties do exist (Livio, 2000; Hillebrandt & Niemeyer, 2000). In principle these could be associated

[†] Published as Kuo-Chuan Pan, Paul Ricker, and Ronald Taam 2012, ApJ, 760, 21

with different SN Ia progenitor systems and explosion mechanisms. It is widely accepted that SNe Ia are thermonuclear explosions of carbon-oxygen (CO) white dwarfs (WDs), but so far observations have not conclusively favored only a single model (Livio, 2000; Hillebrandt & Niemeyer, 2000; Ruiz-Lapuente, 2012; Wang & Han, 2012).

The mainstream progenitor scenarios include the single-degenerate scenario (SDS; Whelan & Iben (1973); Nomoto (1982)) and the double-degenerate scenario (DDS; Iben & Tutukov (1984); Webbink (1984)). The SDS involves a CO WD accreting mass from a non-degenerate companion, such as a main sequence (MS) star, red giant (RG), or helium (He) star, through Roche-lobe overflow (RLOF). Once the CO WD reaches the Chandrasekhar mass, it becomes unstable and explodes as an SN Ia. The DDS instead involves gravitational wave-driven merging of two CO WDs with total mass greater than the Chandrasekhar mass. Recent observations of the nearby SN 2011fe provide useful constraints on its progenitor system (Li et al., 2011a; Nugent et al., 2011; Bloom et al., 2012; Brown et al., 2012; Chomiuk et al., 2012), though both scenarios may contribute to the SN Ia population.

To distinguish between the SDS and DDS, different approaches have been proposed during the past decade. For example, detection of the pre-supernova circumstellar medium around supernova remnants (SNRs) provides evidence of the mass transfer phase in the SDS (Branch et al., 1995; Sternberg et al., 2011; Foley et al., 2012b; Dilday et al., 2012). Collision of the SN ejecta with a non-degenerate companion may affect the early SN light curve, depending on the companion type and viewing angle (Kasen, 2010). Numerical simulations of the SDS also suggest that the non-degenerate companion will survive the SN impact and should be detectable in the SNR (Marietta et al., 2000; Pakmor et al., 2008; Pan et al., 2010, 2012b).

Ruiz-Lapuente et al. (2004) found a star, which they called Tycho G, that is located in the central region of Tycho's SN and has a high proper motion, which in the SDS would be associated with the original orbital speed. This suggests that Tycho G could be a post-impact SDS remnant star. However, Kerzendorf et al. (2009) found that the upper limit of the rotational speed of Tycho G is $\lesssim 7.5$ km s^{-1}, which would seem to be a problem for the SDS interpretation, since the companion stars in close binary systems are usually rapidly rotating. Pan et al. (2012b) address this problem by analyzing the angular momentum lost during the supernova impact, but the final rotational speed depends on the post-impact evolution of the remnant star. Although many detailed studies of the effects of binary evolution on non-degenerate companions have been published (Hachisu et al., 1999; Han & Podsiadlowski, 2004; Han, 2008; Hachisu et al., 2008b; Wang et al., 2009; Meng et al., 2009; Meng & Yang, 2010; Wang & Han, 2010b), usually they have not included the SN impact and post-impact evolution.

Podsiadlowski (2003) studied the post-impact evolution of a $1M_{\odot}$ subgiant by assuming a fixed amount of

energy input and mass stripping. Unsurprisingly, they found that the post-impact star could be overluminous or underluminous compared to a normal star of the same temperature, depending on the choices of these parameters. A more recent study by Shappee et al. (2013a) examined the post-impact evolution of a $1M_{\odot}$ MS star from the HCV scenario in Marietta et al. (2000), using an approach similar to that adopted by Podsiadlowski (2003). They find an overluminous post-impact companion ($10 - 10^3 L_{\odot}$) and suggest that because of this Tycho G may not be associated with Tycho's SN. However, without detailed study of the impact of the SN ejecta on the companion star, especially shock compression in the stellar interior and the depth of energy deposition, these results cannot be considered definitive. Furthermore, the stellar mass and delay time for Tycho G might differ from the progenitor in the HCV scenario, which is the only model considered in Shappee et al. (2012).

In this paper, we consider a wide range of progenitor models from the supersoft channel (WD+MS or WD+subgiant) in Hachisu et al. (2008b)(hereafter HKN) and perform three-dimensional hydrodynamics simulations of the impact of SN Ia ejecta using the method described in Pan et al. (2012b) (hereafter PRT). We then use a one-dimensional stellar evolution code to study the post-impact evolution for each of these progenitor models. In the next section, the numerical methods and progenitor models are described. In Section 4.3, we present the results of post-impact evolution for different companion models and compare their observational quantities with Tycho G. In the final section, we summarize our results and conclude.

4.2 Numerical methods

Our numerical simulations are divided into three stages. The first stage uses a one-dimensional stellar evolution code to construct the progenitor system at the onset of the SN Ia based on detailed binary evolution. The second stage uses a three-dimensional hydrodynamics code to simulate the impact of SN Ia ejecta on the binary companion. The final stage takes the post-impact companion star from the hydrodynamics simulation as input to the stellar evolution code, which is then used to simulate the post-impact evolution.

4.2.1 Simulation codes

The hydrodynamics code used is FLASH[1] version 3 (Fryxell et al., 2000; Dubey et al., 2008). FLASH is a parallel, multi-dimensional hydrodynamics code based on block-structured adaptive mesh refinement (AMR). The equation of state (EOS) applied is the Helmholtz EOS (Timmes & Swesty, 2000). The Poisson equation is solved on the AMR mesh using a Fourier transform-based multigrid algorithm (Ricker, 2008).

[1] `http://flash.uchicago.edu`

The detailed numerical setup and initial conditions are the same as in PRT. In this paper, we consider only three-dimensional simulations that include orbital motion. The initial binary systems are assumed to be in RLOF, and the SN model used is the W7 model (Nomoto et al., 1984).

To construct the progenitor systems and simulate the post-impact evolution of the remnant star, the stellar evolution code MESA[2] (Modules for Experiments in Stellar Astrophysics; Paxton et al. (2011)) is employed. The mixing-length theory (MLT) of convection used is the modified MLT by Henyey et al. (1965), which allows the convective efficiency to vary with the opacity and has important effects on convective zones near the surfaces of stars. The ratio of mixing length to the local pressure scale height is set to $\alpha = 1.918$, which is the value calibrated using the Sun. The initial metallicity is assumed to be $Z = 0.02$ for all the progenitor models.

4.2.2 Progenitor systems

The progenitor systems are taken from the models in HKN. HKN studied the binary evolution of WD+MS systems and found the region of the donor mass-orbital period plane for which SNe Ia may occur. In addition to RLOF mass transfer, HKN consider the optically thick wind from the WD and the mass stripping effects of a massive circumstellar torus. Although recent EVLA observations of SN 2011fe disagree with this scenario (Chomiuk et al., 2012), HKN can explain the circumstellar matter around SN 2002ic, SN 2005gj, and SN 2006X. Furthermore, Hachisu et al. (2008a) found that the theoretical delay-time distribution (DTD) based on this scenario is consistent with the observed DTD.

Figure 7 and Figure 8 in HKN show the initial and final regions of the donor mass-orbital period plane for WD+MS systems with initial WD mass $M_{\rm WD} = 1.0 M_{\odot}$, hydrogen composition $X = 0.70$, metallicity $Z = 0.02$, and stripping rate parameter $c_1 = 3$. We take six evolved MS models from these figures as our progenitor models (see Table 4.1). Since these models are assumed to be in RLOF, we use MESA to evolve a zero-age-main-sequence (ZAMS) star with the initial mass and metallicity taken from HKN until the radius of the MS star reaches its Roche-lobe radius. The Roche-lobe radius, R_L, is approximately given by Eggleton (1983):

$$\frac{R_{\rm L}}{a} = \frac{0.49 q^{2/3}}{0.6 q^{2/3} + \ln(1 + q^{1/3})} \ , \tag{4.1}$$

where q is the mass ratio, and a is the binary separation. The binary separation can be found using Kepler's third law with the given mass and period from HKN. Although MESA has the ability to model binary evolution, we do not include the detailed physics of binary evolution as HKN considered but rather assume the MS star to have a constant mass-loss rate. We vary the mass-loss rate until the MS star matches the

[2] `http://mesa.sourceforge.net`

Table 4.1: The progenitor models

Model	$M_{\rm i}^{\rm a}$ ($M_\odot$)	$P_{\rm i}$ (day)	$R_{\rm i}$ ($R_\odot$)	$L_{\rm i}$ ($L_\odot$)	$T_{\rm eff,i}$ (K)	$M_{\rm f}^{\rm b}$ ($M_\odot$)	$P_{\rm f}$ (day)	$R_{\rm f}$ ($R_\odot$)	$L_{\rm f}$ ($L_\odot$)	$T_{\rm eff,f}$ (K)
A	2.51	0.477	1.83	39.2	10,696	1.88	0.350	1.25	2.35	6,392
B	2.51	0.600	2.08	42.4	10,224	1.82	0.466	1.50	3.64	6,516
C	3.01	1.23	3.64	110.0	9,800	1.82	1.09	2.63	8.06	6,003
D	2.09	0.472	1.67	19.2	9,358	1.63	0.353	1.19	2.09	6,372
E	2.09	0.589	1.91	20.8	8,933	1.59	0.470	1.42	3.15	6,450
F	2.09	0.936	2.59	23.9	7,934	1.55	0.770	1.97	5.09	6,182
G^*	2.00	1.00	1.70	17.6	9,083	1.17	0.233	0.792	0.463	5,355

[a] The mass ($M_{\rm i}$), period (day), radius ($R_{\rm i}$), luminosity ($L_{\rm i}$), and effective temperature ($T_{\rm eff,i}$) for different progenitor models at the beginning of RLOF for WD+MS systems, using the initial masses and orbital periods in Figure 7 of HKN.

[b] The mass ($M_{\rm f}$), period (day), radius ($R_{\rm f}$), luminosity ($L_{\rm f}$), and effective temperature ($T_{\rm eff,f}$) for different progenitor models at the time of the SN explosion, using the final masses and orbital periods in Figure 8 of HKN.

[*] The MS-r model in PRT.

final mass and radius given in HKN within a timescale comparable to theirs ($\sim 10^6$ yr). The mass and radius of these MS stars are shown in Figure 4.1. Since we assume RLOF, the ones with longer periods have larger radii and longer delay times.

Table 4.1 summarizes the initial and final conditions of these six models we have created using MESA. The "MS-r" case in PRT is also included as a comparison (the star G in Table 4.1). Note that the HCV model in Marietta et al. (2000); Shappee et al. (2012) and the HCV' model in PRT are not considered here, since these scenarios did not consider detailed binary evolution. Figure 4.2 shows the density profiles of all these models at the time of the explosion. Most models are slightly evolved MS stars, but some of them are close to ZAMS, depending on the initial periods in HKN. MESA provides all the thermodynamical quantities we need for FLASH simulations. To save computation time, the compositions of the companion models are adjusted to ^{1}H, ^{4}He, plus ^{12}C, where ^{12}C represents all elements heavier than helium. After converting MESA models to FLASH models, we perform FLASH simulations using the method described in PRT.

4.2.3 Post-impact companion models

After the SN impact, the companion star is heated and loses about $\sim 10-20\%$ of its mass due to stripping and ablation by the SN ejecta (see PRT for detailed description of the SN impact). The remaining mass and final conditions of the remnant stars are summarized in Table 4.2. Figure 4.3 shows a typical gas density distribution for model F in the orbital plane at the end of the simulation ($t = 3.26\times10^4$ sec). It is difficult to run hydrodynamics simulations up to the age of historical SNRs ($\sim 500-1000$ yrs) because the dynamical

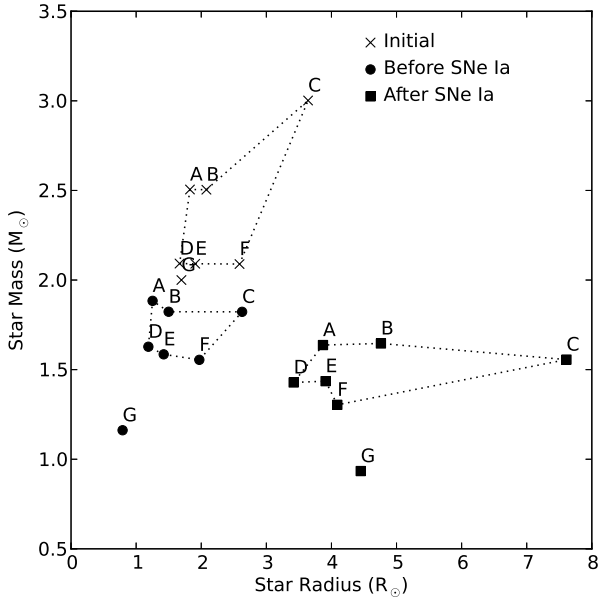

Figure 4.1: Stellar mass and radius for all considered progenitor models at different stages: initial state (×), just prior to SN (filled circles), after reaching hydrostatic equilibrium following SN (filled squares).

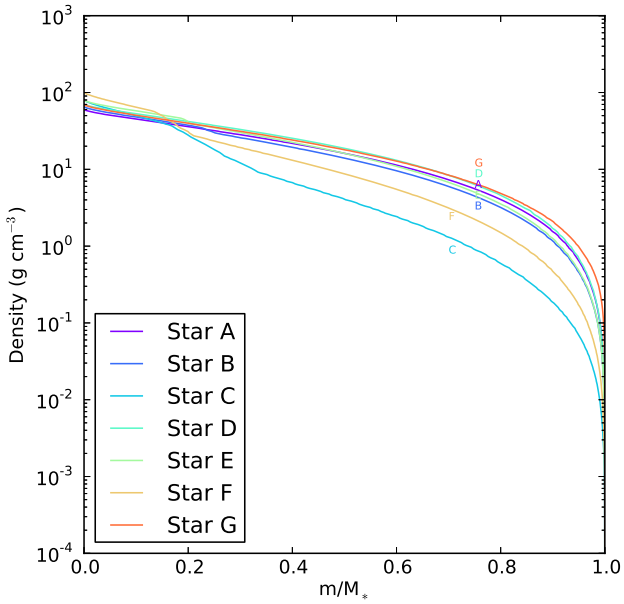

Figure 4.2: Density vs. radius profiles for all the MS models at the time of the SN explosion. The label for each model refers to Table 4.1.

Table 4.2: Post-impact remnant stars

Model	$M_{\rm SN}$ $(M_\odot)$[a]	$R_{\rm SN}$ $(R_\odot)$	$\Delta M/M_*$	$v_{\rm Linear}$ (km s^{-1})[b]	$L_{\rm SN}$ $(L_\odot)$	$T_{\rm eff,SN}$ (K)
A	1.64	3.87	12.8 %	179.0	16.9	5,954
B	1.65	4.76	9.3 %	178.7	22.4	5,760
C	1.56	7.61	14.3 %	136.3	44.2	5,398
D	1.43	3.42	12.3 %	187.7	13.1	5,936
E	1.44	3.91	9.4 %	190.9	14.6	5,715
F	1.30	4.09	16.1 %	142.6	15.0	5,618
G	0.93	4.45	20.1 %	271.0	13.9	5,289

[a] The mass ($M_{\rm SN}$), radius ($R_{\rm SN}$), percentage of unbound mass ($\Delta M/M_*$), linear velocity ($v_{\rm Linear}$), luminosity ($L_{\rm SN}$), and effective temperature ($T_{\rm eff,SN}$) of initial post-impact hydrostatic models in MESA.

[b] Linear velocity includes the pre-supernova orbital speed and kick velocity.

time scale, which determines the timestep, is only on the order of hundreds of seconds. Moreover, the star is close to being spherically symmetric. Therefore, the most straightforward method is to turn the post-impact results back into a one-dimensional problem and solve for the subsequent evolution using MESA.

To run simulations of the post-impact evolution of remnant stars in MESA, the first step is to convert the three-dimensional data into angle-averaged one-dimensional radial profiles. Our setup in MESA cannot deal with the spin of the remnant star, and the angular momentum is finite at the end of the FLASH simulations. However, PRT demonstrated that the loss of angular momentum during the SN impact will significantly decrease the spin. Since the rotational velocity is significantly less than breakup, $\Omega_{\rm K} = (GM/R_*^3)^{1/2} \sim 5 \times 10^{-5}$ s^{-1}, we ignore the spin during MESA simulations, but consider it separately using the post-impact specific angular momentum from FLASH. The role of rotation will be discussed in more detail in Section4.3.3.

Since the companion models at the end of the FLASH simulations are not yet in hydrostatic equilibrium, the averaged radial profiles of density, temperature and pressure cannot be used directly in MESA. However, the averaged specific entropy and composition mass profiles are conserved if the system is adiabatic. Since the Mach numbers at the end of the FLASH simulations are subsonic for most gravitationally bound gas, we can use these profiles, as a start, to construct hydrostatic models for MESA. Hydrostatic equilibrium should be achieved relatively quickly after the SN impact in comparison with the thermal timescale.

To calculate the averaged specific entropy and composition profiles, only gravitationally bound gas is considered, and the center of the remnant star is taken to be the location of the gravitational potential minimum. The simulation domain is then divided into $128 - 256$ radial bins, depending on the zone spacing and the distance between the star's center and the boundary of the simulation box at the end of the FLASH simulation. Although FLASH and MESA include a more realistic EOS, for simplicity only an "ideal gas

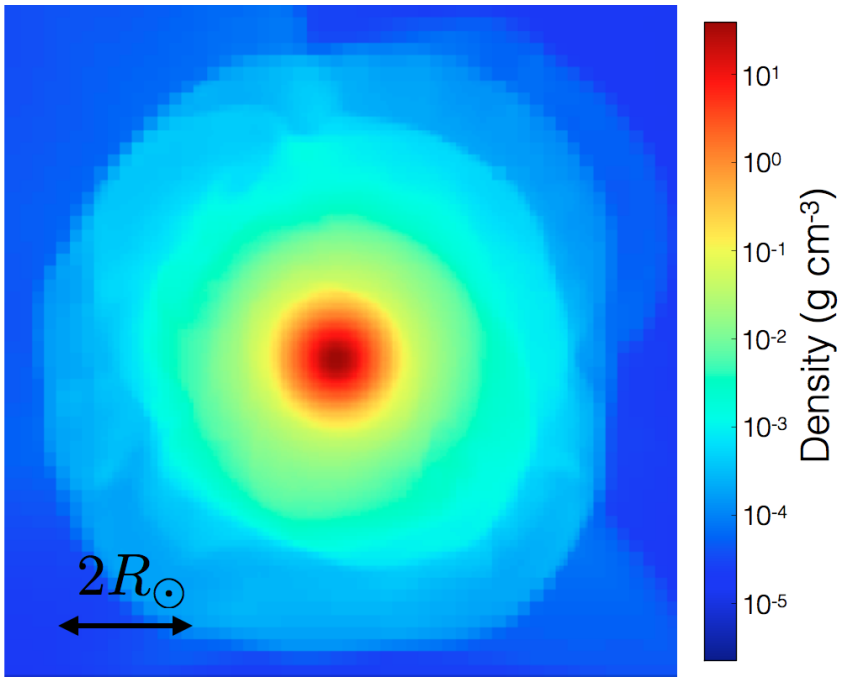

Figure 4.3: Gas density distribution in the orbital plane for a three-dimensional SN Ia simulation with model F (see Table 4.1) at time $t = 3.26 \times 10^4$ sec after the explosion. The frame shows a domain spanning $10R_\odot$. The color scale indicates the logarithm of the gas density.

plus radiation" EOS is used to calculate the entropy profile. Therefore the specific entropy is

$$S = \frac{N_A k_B}{\mu} \ln\left(\frac{T^{3/2}}{\rho}\right) + \frac{4aT^3}{3\rho} \ , \tag{4.2}$$

where N_A is the Avogadro constant, k_B is the Boltzmann constant, a is the radiation constant, ρ is the bound gas density, T is the temperature, and μ is the mean molecular weight. Using the total bound mass (M_*), the EOS, and the entropy and composition profiles, the density, pressure (P), temperature (T), and radius can be calculated by solving the hydrostatic equations,

$$\frac{dr}{dM_r} = \frac{1}{4\pi r^2 \rho}, \tag{4.3}$$

$$\frac{dP}{dM_r} = -\frac{GM_r}{4\pi r^4}, \tag{4.4}$$

where G is the gravitational constant, and M_r is the mass within radius r. The hydrostatic equations are solved using the fourth-order Runge-Kutta method with adaptive stepsize control. We use the shooting method, varying the initial central density to match the boundary condition $M(r = R_*) = M_*$, $\rho(r = R_*) = 0$, and $P(r = R_*) = 0$.

The reconstructed mass and radius of the post-impact remnant stars are shown in Figure 4.1. The upper left and right panels in Figure 4.4 and Figure 4.5 show the averaged 1D entropy and helium composition profiles from the FLASH output. Models B, C, E, and F have larger radii and higher central helium abundances (upper right panel), since their delay time and initial orbital periods are longer in HKN. We flatten the entropy profiles in the outermost region ($0.95 - 0.99 < m/M_* < 1$) to avoid negative entropy gradients. The sensitivity of our results to these flattened entropy profiles have been tested by varying the amount of the flattened entropy and using a smoothly increasing profile instead of a flat one. We find that the outermost region of the entropy profile does not significantly affect the hydrostatic solution and post-impact evolution.

Another necessary variable is the initial luminosity profile, $L(m)$. If there is no convection, the luminosity profile can be estimated using the radiative temperature gradient expression,

$$L(m) = -\frac{(4\pi r^2)^2 ac}{3\kappa}\frac{dT^4}{dm} \ , \tag{4.5}$$

where κ is the opacity and c is the speed of light. The opacity can be calculated using the `kap` module in MESA for a given density, temperature, and composition. This estimate is reasonable only at the beginning, since the modified entropy gradient is positive everywhere. The energy deposited by SN ejecta heating causes a small temperature bump at $m \sim 0.95 M_*$ (see middle panels in Figure 4.4 and Figure 4.5), leading to the luminous region in the luminosity profiles in Figure 4.4 and Figure 4.5.

4.3 Evolution of post-impact remnant stars

In this section, the post-impact evolution of remnant stars using MESA is qualitatively described and compared with Tycho G. The effect of post-impact evolution with a different explosion energy is also studied to provide an understanding of the resultant evolution for a non-W7 explosion. In addition, the angular momentum distribution of post-impact remnant stars is examined by using the specific angular momentum from FLASH and the hydrostatic models in MESA, addressing the rotation problem in Tycho G.

4.3.1 Post-impact evolution

The hydrostatic solutions described in the previous section are used as initial conditions for the models used in MESA. The initial timestep in MESA is chosen to be between 10^{-4} and 10^{-1} years, depending on the particular model. The compositions in the FLASH simulations are expanded to the extended network in MESA with 25 isotopes. The percentages of compositions other than ^{1}H and ^{4}He are scaled to solar

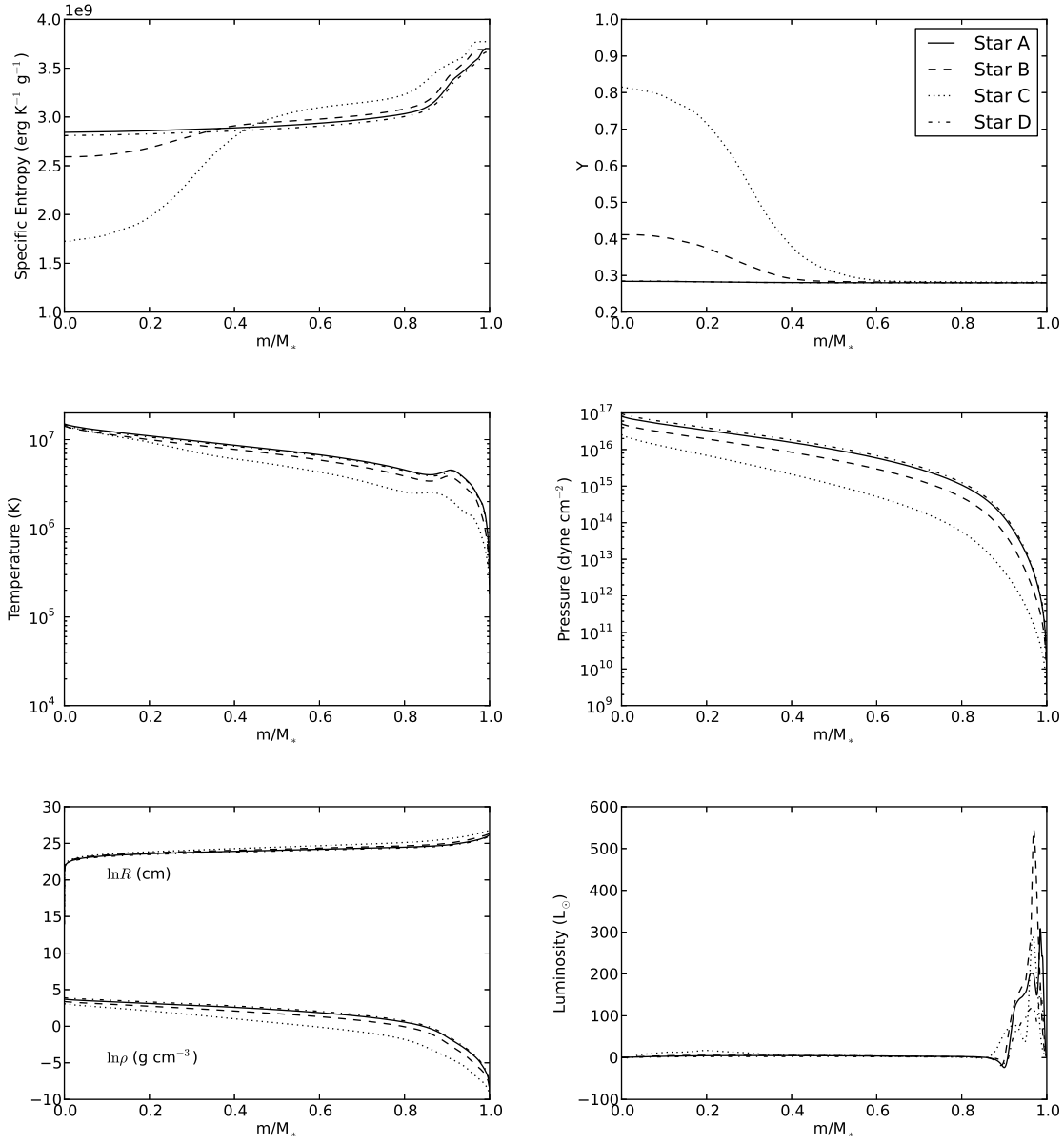

Figure 4.4: Hydrostatic solutions for entropy (S) helium composition (Y), density (ρ), temperature (T), pressure (P), radius (R), and enclosed luminosity $L(m)$ for models A, B, C, and D in Table 4.2.

abundances, but with the same total metallicity. When starting a MESA simulation the model is iterated until convergence to ensure that both the EOS and the energy generation rate are consistent. During the first few steps, the evolution is transient, but eventually evolves to a parameter-independent model within a year. Thus, only simulation results after one year are considered in this study.

Figure 4.6 shows the evolution of the photospheric radius, luminosity, and effective temperature as functions of time. The post-impact remnant stars rapidly expand on a timescale of $\sim 10^2$ years for models

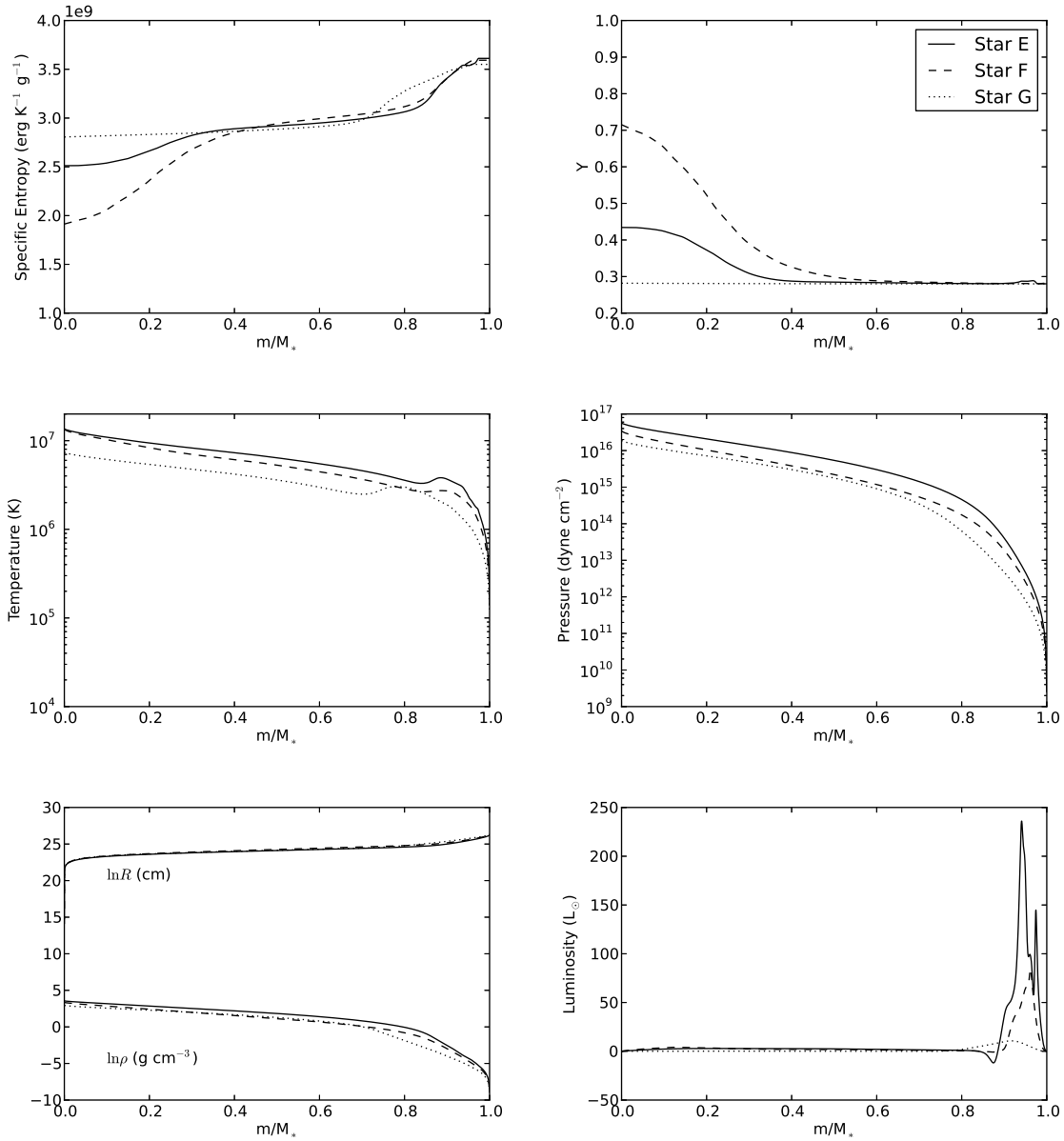

Figure 4.5: Similar to Figure 4.4 but for models E, F, and G.

Table 4.3: Post-impact remnant star after 440 years

Model	$M_{\rm SN}$ $(M_\odot)$[a]	$R_{\rm SN}$ $(R_\odot)$	$L_{\rm SN}$ $(L_\odot)$	$T_{\rm eff,SN}$ (K)	$v_{\rm Rotation}$ (km s^{-1})
A	1.64	7.18	202.7	8,135	10.5 ± 1.3
B	1.65	11.9	279.0	6,832	8.3 ± 0.6
C	1.56	10.5	81.4	5,356	2.0 ± 2.9
D	1.43	6.57	111.4	7,319	9.1 ± 1.3
E	1.44	4.56	20.2	5,737	26.7 ± 4.4
F	1.30	4.35	17.0	5,623	17.3 ± 2.2
G	0.93	4.37	13.4	5,287	18.9 ± 2.5
GH09 †	1.0	$1.4 - 2.8$	$1.9 - 7.6$	5900 ± 100	—
GH09 †	1.4	$1.6 - 3.3$	$3.0 - 11.8$	5900 ± 100	—

[a] The mass ($M_{\rm SN}$), radius ($R_{\rm SN}$), luminosity ($L_{\rm SN}$), effective temperature ($T_{\rm eff,SN}$), and surface rotational speed ($v_{\rm Rotation}$) of post-impact remnant stars at 440 yr after SN explosion.

† The radius and luminosity are estimated using the surface gravity value $\log g = 3.85 \pm 0.3$ in González Hernández et al. (2009), assuming the mass is $1M_\odot$ or $1.4M_\odot$.

A, B, D, and E, and $\sim 10^3$ years for models C and F. Note that there is no significant change in model G within 10^4 years, because the thermal timescales in model G are much longer than other stars.

Here we describe the detailed evolution of model A as an example. Due to the high opacity in the outermost region of the envelope, the photospheric luminosity is $\sim 4\ L_\odot$, but the luminosity inside the envelope is much higher than the surface luminosity (Figure 4.4). Therefore, the strong radiation at $m \sim 0.9M_*$ expands the outermost $\lesssim 1\%$ of mass. In addition, the luminosity profile of the outermost 10% of mass flattens due to radiative diffusion. This radiative diffusion timescale is characterized by the local thermal timescale (Henyey & L'Ecuyer, 1969),

$$\tau_{\rm th}(r) = \frac{3}{64\pi\sigma_{\rm SB}} \left[\int_r^{R_*} \left(\frac{\kappa C_p}{T^3} \right)^{1/2} \rho dr \right]^2 , \tag{4.6}$$

where $\sigma_{\rm SB}$ is the Stefan-Boltzmann constant, and C_p is the specific heat capacity. Although the global thermal timescale, $t_{\rm th} = GM^2/2RL$, is of the order of 10^6 years, the local thermal timescale in the envelope region is only $\sim 10^2 - 10^3$ years.

After $\sim$ 200 years, the deposited energy has been radiated away and model A starts to contract by releasing gravitational energy. The luminosity decreases, but the effective temperature increases. The star will eventually return to a stage similar to the ZAMS on a global thermal timescale. As a SN Ia remnant may not be recognizable in millions of years, the simulation is terminated at 10^4 years.

The evolutionary tracks of post-impact remnant stars in the Hertzsprung-Russell (H-R) diagram are plotted in Figure 4.7. In general, the remnant stars become brighter but cooler after the impact. By

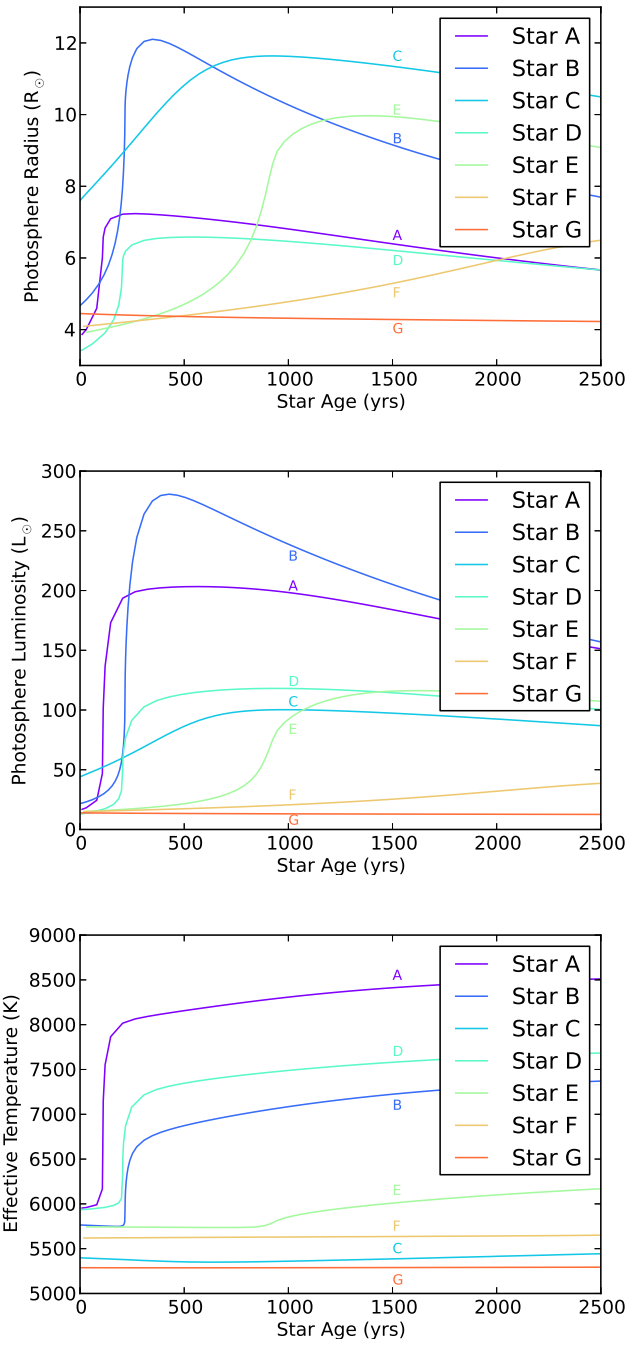

Figure 4.6: Evolution of the photospheric radius, luminosity, and effective temperature as functions of time. Each line shows the evolution of a post-impact companion star in Table 4.2.

comparing Figure 4.7 with Figure 4.1, we find that there is a trend for more massive stars coupled with smaller radius (shorter orbital period) to evolve faster in the HR diagram. In addition, stars with smaller radii have higher effective temperatures after the SN impact. This can be understood given the fact that stars with shorter orbital periods are closer to the exploding WD, leading to more violent SN impacts and greater energy deposition, but with less unbound mass due to their more compact states.

The Tycho G star, based on observations by González Hernández et al. (2009), is also plotted in Figure 4.7. Ruiz-Lapuente et al. (2004) determined Tycho G's effective temperature, $T_{\rm eff} = 5750 \pm 250$ K, and surface gravity, $\log(g/{\rm cm\ s^{-2}}) = 3.5 \pm 0.5$, by fitting spectral lines. Subsequently, González Hernández et al. (2009) updated the observed values to $T_{\rm eff} = 5900 \pm 100$ K and $\log(g/{\rm cm\ s^{-2}}) = 3.85 \pm 0.30$ based on fits to iron lines. González Hernández et al. (2009) estimated the radius of Tycho G using the surface gravity, assuming the mass of Tycho G to be $1 M_\odot$. They estimated the bolometric luminosity L_* to lie in the range $1.9 < L_*/L_\odot < 7.6$. However, this luminosity could be underestimated if Tycho G is more massive. Since $\log L_* \propto 2 \log R + 4 \log T$ and $\log g \propto \log M - 2 \log R$, L_* could be increased to $3.0 < L_*/L_\odot < 11.8$ if the mass of Tycho G were instead $1.4 M_\odot$. Our post-impact remnant stars have masses ranging from $1.3 M_\odot$ to $1.65 M_\odot$. A mass $M_* = 1.4 M_\odot$ instead of $1 M_\odot$ is, therefore, assumed for Tycho G. As a result, the placement of Tycho G in the HR diagram is now closer to our models A, B, D, E and F immediately after the SN impact (triangle symbols in Figure 4.7). However, Tycho's SN exploded 440 years ago, and models A, B and D would have evolved to a hotter and more luminous state in that time (star symbols in Figure 4.7), suggesting that model E among our progenitor systems is the least discrepant with Tycho G. Our model E has a consistent effective temperature, but the luminosity (radius) is twice brighter (larger) than the observed value in González Hernández et al. (2009). Model F has a luminosity similar to that of model E, but the effective temperature is a few hundred degrees lower than Tycho G. A less massive or smaller model than model E may better match the observation by González Hernández et al. (2009). Table 4.3 summarizes the stellar properties for all the progenitor models at 440 yr after the SN explosion.

4.3.2 Dependence on the SN ejecta energy

Although Tycho's SN has previously been suggested to be a subluminous SN Ia (van den Bergh, 1993), or a overluminous SN Ia (Ruiz-Lapuente, 2004), the most recent observation using the light echo suggests Tycho's SN is actually a normal SN Ia (Krause et al., 2008). In our hydrodynamics simulations, the W7 model ($E_{\rm SN} = 1.23 \times 10^{51}$ erg) is assumed to describe the SN explosion. However, the exact explosion energy could be different from case to case. Therefore, two additional simulations for model D and E, which are the remnant stars closest to Tycho G, are performed with double the explosion energy. We specify that this

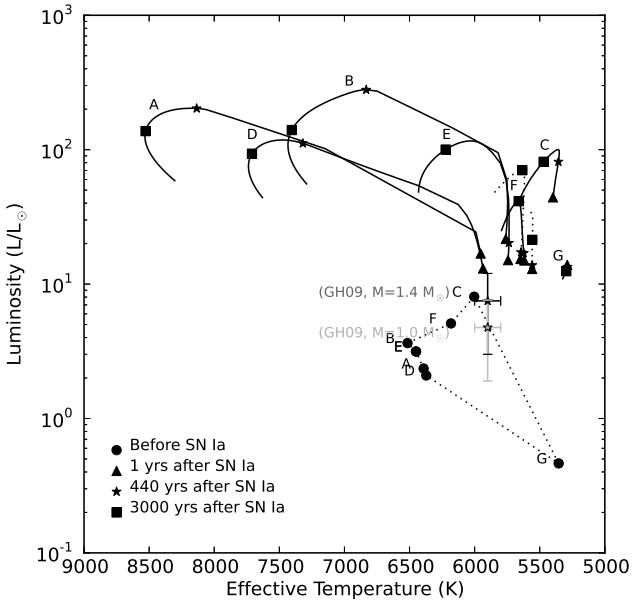

Figure 4.7: The evolutionary tracks in the HR diagram for different post-impact companion models. Each line shows an evolutionary track of a companion model in Table 4.2 over an interval of 10^4 years. The filled circles indicate the condition of stars just before the SN Ia explosion; filled triangles present the condition of stars at ~ 1 year after the SN impact; star symbols show the conditions at 440 years after the SN impact, which is the same age as Tycho's SN; filled squares present the conditions at $3,000$ years after the SN impact. The star symbols with error bars show the observed luminosity and effective temperature of Tycho G as measured by González Hernández et al. (2009) (GH09) in Table 4.3.

additional energy is in a thermal form.

Pakmor et al. (2008) have shown that the unbound mass of the companion star is linearly proportional to the SN kinetic energy. In our hydrodynamics simulations, a similar trend is observed, but it is not linear, since there are essentially two mechanisms that unbind the mass: ablation and stripping (see PRT for detailed description). The resulting mass of the post-impact remnant star for model D (model E) is $M_{\rm W7} = 1.43\ M_\odot$ ($1.44\ M_\odot$) for the W7 case and $M_{\rm 2X} = 1.23\ M_\odot$ ($1.37\ M_\odot$) for the case with double the explosion energy.

Figure 4.8 shows the temperature profiles of these four explosion cases after the SN impact. The heating is stronger in the higher explosion energy case, resulting in a lower remnant mass and causing a lower central temperature. The temperature bump in the higher explosion energy case shifts inwards because the heating penetrates to deeper mass layers with a stronger impact. Therefore, the radiative diffusion time for the propagation of energy to the surface becomes longer.

The evolution of the photospheric radius, luminosity, and effective temperature can be seen in Figure 4.9. The lower mass and temperature in the higher energy case cause the radius, luminosity, and effective temperature to be smaller than for the W7 case. In general, increasing the explosion energy will lower the effective temperature and luminosity, but the evolution timescale is also proportional to the explosion energy. For example, a dramatic difference in the evolution is seen for model D in which the luminosity decreases by a factor of eight (see Figure 4.9) at 440 years in comparison with the standard explosion energy (W7). This difference reflects the deeper energy deposition and longer thermal diffusion time associated the sequence corresponding to twice the explosion energy. If we desire to match the luminosity of Tycho G by enhancing the explosion energy, the effective temperature becomes too low since the mass of the remnant star becomes lower. Thus, neither an overluminous or subluminous explosion model for model D or E can perfectly match the observed properties of Tycho G.

4.3.3 Rotation problem

In the binary evolution scenarios in HKN, the evolution time from the onset of RLOF in the MS+WD systems to the SN Ia phase is about 10^6 years. Although the mass transfer in close binary systems may cause the companion stars to be non-corotating, Zahn (1977) finds the synchronization time in binary systems to be

$$t_{\rm sync} \sim q^{-2}(a/R)^6 \sim 10^4((1+q)/2q)^2 P^4 \text{ years}, \tag{4.7}$$

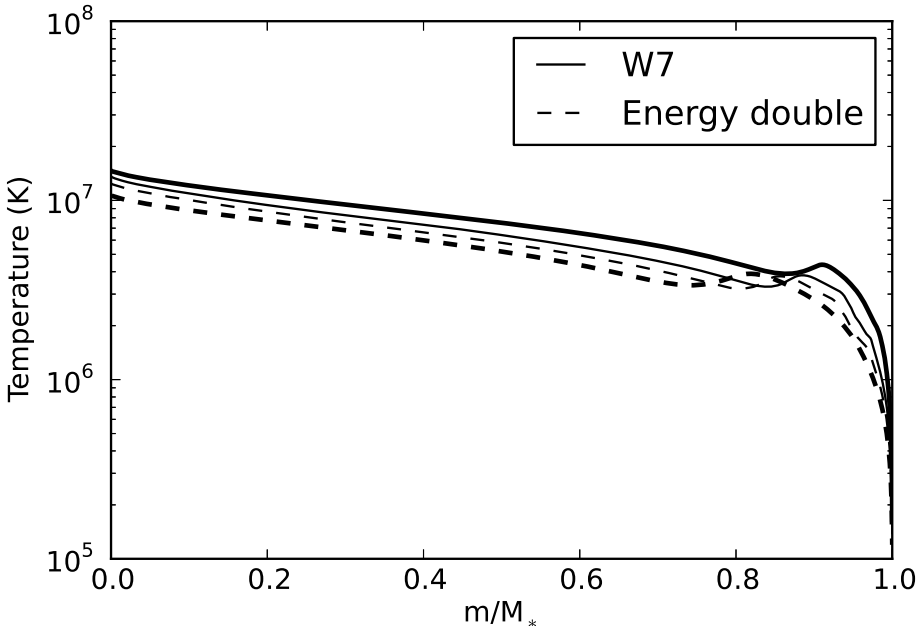

Figure 4.8: Temperature vs. mass profiles of the hydrostatic solutions for model D (thick lines) and model E (thin lines) with different SN Ia explosion energies. The solid lines indicate the temperature profiles with explosion energy using the W7 model ($E_{\rm SN} = 1.23 \times 10^{51}$ erg). The dashed lines show the temperature profiles with double the explosion energy.

which is $\sim 10^3$ years in our cases. Therefore, the companion stars should all be synchronized by tidal locking and be rapidly rotating, resulting in surface rotational speeds of the order of hundreds of kilometers per second. However, the upper limit on the rotation speed of Tycho G found by Kerzendorf et al. (2009) is $v \sin i \lesssim 7.5$ km s^{-1}, where i is the inclination angle.

PRT indicate that the companion star (model G in Table 4.1) loses about half of its angular momentum while only losing about 20% of its mass. With the strong assumptions that the parameter α is constant in the angular momentum expression, $J = \alpha M R^2 \omega$, and that the companion star is in a state of solid-body rotation before and after the impact, the rotation speed can significantly drop to about a quarter of its original rotation speed. However, the equilibrium status of the remnant stars and the location of the photosphere were not calculated in detail in PRT. Combining the post-impact angular momentum distributions in FLASH with the stellar structure of post-impact remnant stars in MESA, the rotation problem in the Tycho G can be addressed quantitatively.

Before the SN impact, the companion stars were set into uniform rotation and were given a spin with spin-to-orbit ratio of 0.95. After the SN impact, the companion stars are no longer in solid-body rotation.

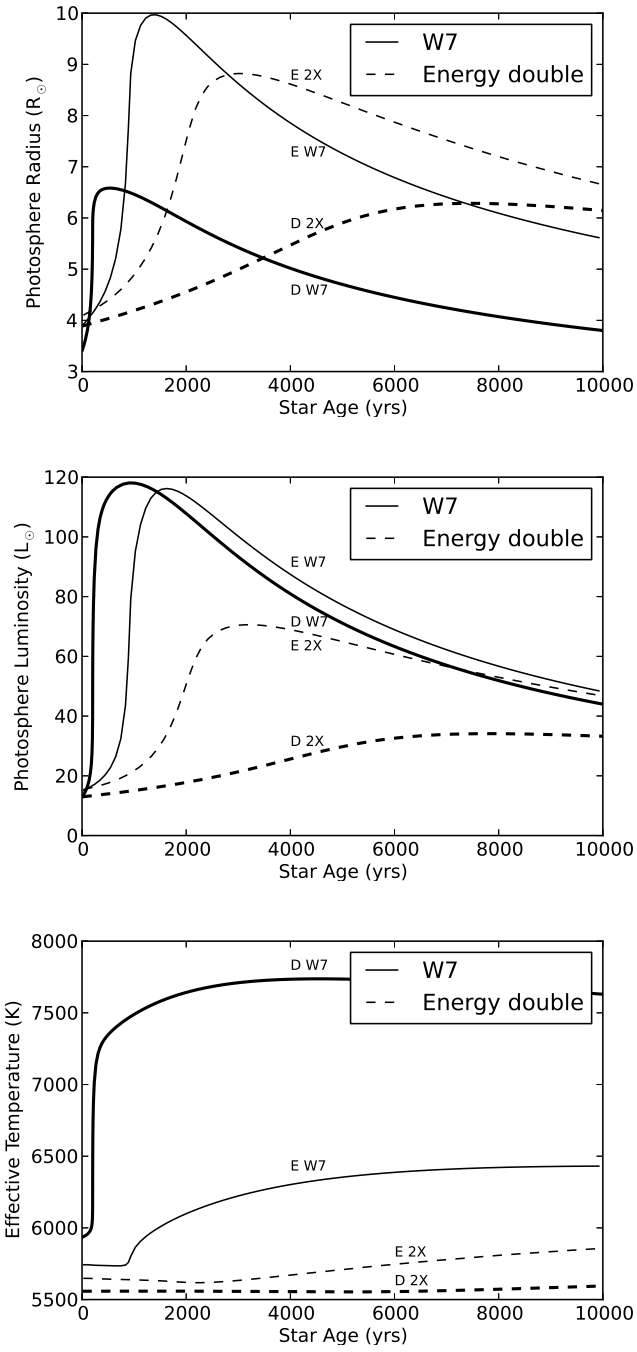

Figure 4.9: Similar to Figure 4.6, but for model D (thick lines) and E (thin lines) with different SN Ia ejecta energy.

The angle-averaged angular velocity profiles can be calculated using

$$\Omega(r) = \left\langle \frac{v_\phi}{r\cos\theta} \right\rangle_{\phi,\theta}, \tag{4.8}$$

where θ and ϕ are latitude (zero at the equator; positive northward) and longitude (positive in the direction of rotation) in spherical coordinates and in the center-of-mass frame. It is found that the angular velocity is insensitive to the latitude and longitude. Thus, only the radial dependence in spherical coordinates is considered. If we assume the specific angular momentum, $h(m) = \frac{2}{3}r(m)^2\Omega(m)$, to be conserved during the evolution, the angular velocity and surface rotational speed profiles of hydrostatic models can be calculated. Figure 4.10 shows the specific angular momentum profiles of all considered models in Table 4.2. Since the angular velocity from the FLASH simulations has some variations in the surface region, we use the standard deviation of the specific angular momentum in the region of $0.8 < m/M_* < 1.0$ to estimate the uncertainty of specific angular momentum.

Figure 4.11 shows the evolution of surface rotational speed for all the remnant star models. The error bars show the uncertainty of surface rotational speed based on the uncertainty from the specific angular momentum. It is found that the rotational speed at the surface of all the models significantly decreases to a value less than 30 km/sec. Note that the observed radial velocity of Tycho G is 94 ± 27 km s^{-1} by Ruiz-Lapuente et al. (2004) and 79 ± 2 km s^{-1} by Kerzendorf et al. (2009), but the linear speed in our models are about ~ 200 km s^{-1} (Table 4.2), corresponding to an inclination angle $\sin i \sim 0.4$. Since the specific angular momentum $h_{\rm surface} \propto R_*^2\Omega(R_*) \propto R_* v_{\rm rot}$, the surface rotation speed decreases while the post-impact remnant star is expanding. For the rapidly evolving stars such as models A,B, and D, the rotation speed decreases to less than 10 km/sec within 500 years. After $1,000 - 1,500$ yrs, the stars start to contract, slowly increasing the surface rotation speed, but the surface rotation speeds of all models at 440 years are still below 30 km s^{-1}. In addition, the surface rotation speed of models A, B, C, and D lie below 10 km/sec at 440 years (Table 4.3). Although the surface rotation speed in our model E is still above the upper limit found by Kerzendorf et al. (2009), our progenitor models show that the post-impact remnant stars do not need to be fast rotaters in the supersoft channel (WD+MS). However, Tycho G could also be a stripped giant star that has lost most of its angular momentum during the SN Ia impact and then cooled (Kerzendorf et al., 2009), or an expanded and slowed-down M dwarf as suggested by Wheeler (2012).

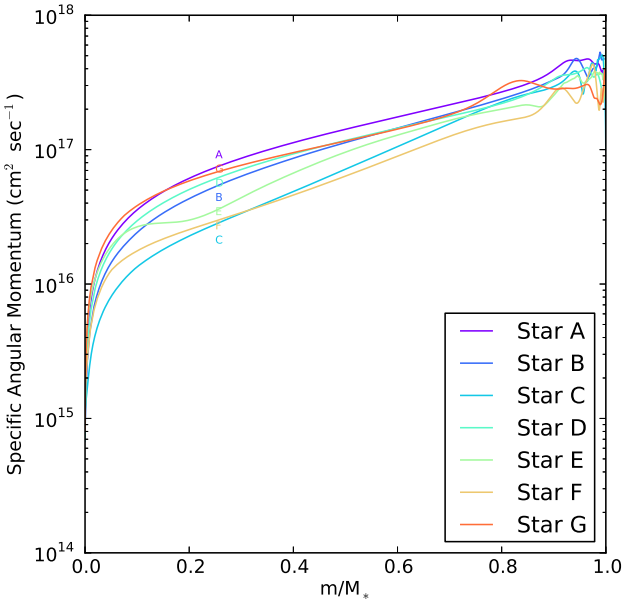

Figure 4.10: Specific angular momentum as a function of the mass fraction for all companion models in Table4.2.

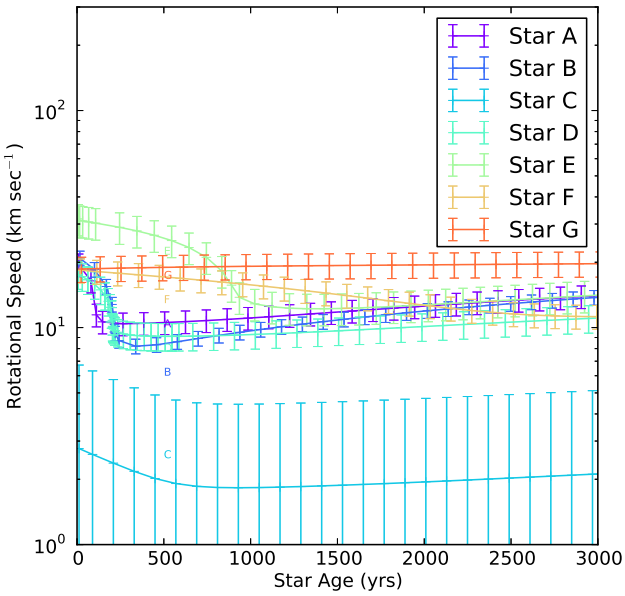

Figure 4.11: Evolution of surface rotational speed for all the companion models in Table 4.2. The error is estimated by the variation of specific angular momentum within $0.9 < m/M_* < 1.0$ in Figure 4.10.

4.4 Conclusions

We have investigated the post-impact evolution of remnant stars in the single-degenerate scenario for SNe Ia via stellar evolution calculations. We examined six possible binary companion models in the mass-orbital-period space from Hachisu et al. (2008b) and one companion model in Pan et al. (2012b), and we performed three-dimensional hydrodynamics simulations using the setup in Pan et al. (2012b). The post-impact evolution of the surviving stars was studied by using the stellar evolution code MESA, together with the reconstructed hydrostatic remnant star models. It is found that the luminosity of post-impact remnant stars increases to $10 - 50 L_{\odot}$ after the supernova impact and increases to $\sim 100 L_{\odot}$ within a few thousand years, depending on the progenitor model. Due to the energy deposition from the SN ejecta, the envelope of the post-impact remnant expands on its local thermal timescale ($\sim 10^2 - 10^4$ yrs). After this expansion, stars start to contract and release gravitational energy. The post-impact evolution is directly affected by the explosion energy since it is related to the amount of unbound mass after the SN impact and the amount and depth of energy deposited in the remnant star. Among the calculated models, the companion E in our simulation (see Table 4.1), which has a mass $M = 1.44 M_{\odot}$, radius $R = 4.57 R_{\odot}$, effective temperature $T_{\rm eff} = 5,737$ K, and luminosity $L = 20.3 L_{\odot}$ after 440 years of the SN Ia explosion, is closest to the observed properties of Tycho G as determined by González Hernández et al. (2009) Although the fits are promising, the luminosity is twice as large as the value given by González Hernández et al. (2009). Finally, by comparing the observed radial velocity to the linear speed in our progenitor models, an inclination angle $\sin i \sim 0.4$ can be inferred. The surface rotational speed thus implied ($\sim 10 - 20$ km s^{-1}) approaches the low upper limit on the rotational speed of Tycho G found by Kerzendorf et al. (2009). Our results provide some support for Tycho G as a possible progenitor candidate in the SDS and point to the need for further detailed studies of the SDS binary evolutionary channel.

Chapter 5

Evolution of Post-Impact Remnant He Stars in SN Ia Remnants within the Single-Degenerate Scenario[†]

Abstract

The progenitor systems of Type Ia supernovae (SNe Ia) are still under debate. Based on recent hydrodynamics simulations, non-degenerate companions in the single-degenerate scenario (SDS) should survive the supernova impact. One way to distinguish between the SDS and the double-degenerate scenario is to search for the post-impact remnant stars (PIRSs) in SN Ia remnants. Using a technique that combines multi-dimensional hydrodynamics simulations with one-dimensional stellar evolution simulations, we have examined the post-impact evolution of helium-rich binary companions in the SDS. It is found that these helium-rich PIRSs (He PIRSs) dramatically expand and evolve to a luminous phase ($L \sim 10^4 L_\odot$) about 10 years after a supernova explosion. Subsequently, they contract and evolve to become hot blue-subdwarf-like (sdO-like) stars by releasing gravitational energy, persisting as sdO-like stars for several million years before evolving to the helium red-giant phase. We therefore predict that a luminous OB-like star should be detectable within ~ 30 years after the SN explosion. Thereafter, it will shrink and become an sdO-like star in the central regions of SN Ia remnants within star-forming regions for SN Ia progenitors evolved via the helium-star channel in the SDS. These He PIRSs are predicted to be rapidly rotating ($v_{\rm rot} \gtrsim 50$ km s^{-1}) and to have high spatial velocities ($v_{\rm linear} \gtrsim 500$ km s^{-1}). Furthermore, if supernova remnants have diffused away and are not recognizable at a later stage, He PIRSs could be an additional source of single sdO stars and/or hypervelocity stars.

5.1 Introduction

The catastrophic explosions of Type Ia supernovae (SNe Ia) are of great importance in probing the history of the universe. It is generally believed that SNe Ia are caused by thermonuclear explosions of carbon-oxygen

[†] Kuo-Chuan Pan, Paul Ricker, and Ronald Taam 2013, ApJ, submitted

(CO) white dwarfs (WDs) in close binary systems, but their intrinsic variety and nature of their progenitor systems is still under debate (Livio, 2000; Hillebrandt & Niemeyer, 2000; Ruiz-Lapuente, 2012; Wang & Han, 2012).

Current mainstream progenitor scenarios include the single-degenerate scenario (SDS; Whelan & Iben, 1973; Nomoto, 1982) and the double-degenerate scenario (DDS; Iben & Tutukov, 1984; Webbink, 1984). In the SDS, the binary companion is a non-degenerate companion which could include stars of many different stellar types, including main-sequence (MS) stars, red giants (RGs), helium (He) stars, and M-dwarfs (Hachisu et al., 1999; Ivanova & Taam, 2004; Hachisu et al., 2008b; Wang et al., 2009, 2010; Wang & Han, 2010a; Wheeler, 2012). However, these non-degenerate companions are usually hydrogen- or helium-rich. The observational upper limit of stripped hydrogen after SN impact is $< 0.01 M_{\odot}$ for SN 2005am and SN 2005cf (Leonard, 2007), and $< 0.001 M_{\odot}$ for SN 2011fe (Shappee et al., 2013b). Thus, the absence of the hydrogen that should appear in SN Ia spectra poses a problem for the SDS. The DDS instead results from mergers of two CO WDs with total mass greater than the Chandrasekhar mass, avoiding the hydrogen problem. These violent events may lead to accretion-induced collapse to neutron stars instead of thermonuclear explosions (Nomoto & Iben, 1985). However, estimates of the delay time distribution (DTD) based on observed supernova rates are consistent with a large fraction of events being due to double degenerate progenitors (Maoz et al., 2011, 2012).

Based on recent hydrodynamics simulations of SN Ia impact on binary companions in the SDS, including grid-based (Marietta et al., 2000; Pan et al., 2010, 2012b) and smooth particle (SPH; Pakmor et al., 2008; Liu et al., 2012) simulations, these non-degenerate companions should survive the SN impact and could be detectable. Thus, one of the simplest ways to distinguish between the SDS and DDS is to search for post-impact remnant stars (PIRSs) in Type Ia supernova remnants (Ia SNRs).

Recent PIRS searches have studied two Galactic Ia SNRs (SN 1572, Ruiz-Lapuente et al. 2004; Ihara et al. 2007; Kerzendorf et al. 2009; González Hernández et al. 2009; Kerzendorf et al. 2012b, and SN 1006, González Hernández et al. 2012; Kerzendorf et al. 2012a) and two Ia SNRs in the Large Magellanic Cloud (LMC; Edwards et al., 2012; Schaefer & Pagnotta, 2012). So far, only M-dwarf stars and the subgiant Tycho G star have emerged as possible PIRS candidates, and they are not well matched with companion models in the standard SDS channels, a result that may favor the DDS. However, the properties of a PIRS could change significantly after the SN impact. For instance, Marietta et al. (2000) and Pan et al. (2012b) have shown that almost all the envelope of the RG in the RG-WD channel should be removed during the SN impact, and $\sim 10 - 20\%$ of the MS star mass should be stripped and ablated in the MS-WD channel (Marietta et al., 2000; Pan et al., 2012b; Liu et al., 2012). Therefore, the PIRS in the RG-WD channel could

be a helium pre-WD or low mass helium burning star with little hydrogen-rich envelope. We note that the SN impact will not only strip and ablate the mass of a non-degenerate companion star, but also compress and deposit energy into it (Pan et al., 2012b).

The evolution of PIRSs has been studied by Podsiadlowski (2003) for a $1M_{\odot}$ sub-giant companion and by Shappee et al. (2013a) for a $1M_{\odot}$ MS companion. They found that PIRSs could be over-luminous due to the energy release from the SN energy deposition, suggesting that the SDS should be ruled out for several Ia SNRs. However, in their calculations, these authors assumed ad-hoc prescriptions for energy input and mass stripping without performing detailed hydrodynamical calculations and, therefore, did not accurately calculate the shock compression in the stellar interior and the depth of the energy deposition. In Pan et al. (2012a), we studied the evolution of PIRSs using a detailed treatment of SN impact via three-dimensional hydrodynamics simulations. These simulations included the symmetry-breaking effects of orbital motion, rotation of the non-degenerate companions, and Roche-lobe overflow for the MS-WD channel. These three-dimensional simulation results were mapped into a one-dimensional stellar evolution code to simulate the post-impact evolution. It was found that MS-like PIRSs evolve to become subgiants ($L \sim 10 - 100 L_{\odot}$) after a few hundred years and could be slowly rotating after stellar expansion. Although the model closest to the Tycho G star in these calculations was twice as bright, these results provide some support for Tycho G as a possible PIRS in the SDS.

A new subclass of sub-luminous SNe Ia, namely Type Iax supernovae (SNe Iax), recently has been proposed by Foley et al. (2012a). This population could originate from the He-WD channel in the SDS via a helium double-detonation explosion or by merger of a He WD with a CO WD (Foley et al., 2012a; Wang et al., 2013). The He-WD channel naturally explains the absence of hydrogen lines, and two SNe Iax have shown helium lines in their spectra, suggesting that helium must be present in the progenitor systems. Pan et al. (2010, 2012b) have shown that only about $\lesssim 5\%$ of the mass of the helium star is lost into the SNR in the He-WD channel, an amount that is much lower than the hydrogen mass lost in the MS-WD channel and the RG-WD channel. The He-WD channel mainly contributes to the prompt part of the delay-time distribution in population synthesis studies ($\sim 45 - 220$ Myr, Wang & Han 2010b), and this is consistent with the distribution of SNe Iax, since no SNe Iax have been observed in elliptical galaxies. Finally, several He-WD binary systems with the properties required to be SN Ia progenitors have been observed, for example KPD 1930+2752 (Maxted et al., 2000; Geier et al., 2007), CD-30 11223 (Vennes et al., 2012; Geier et al., 2012), and RX J0648.0-4418 (Mereghetti et al., 2009). These systems have either a massive WD ($M_{\rm WD} \gtrsim 1.3 M_{\odot}$) or a short orbital period ($P_{\rm orb} < 0.05$ d). The helium nova V445 Pup is also considered to be a likely progenitor system (Kato et al., 2008).

In this paper, we follow the methods in Pan et al. (2012a) and extend the study of post-impact evolution to helium-rich PIRSs (He PIRSs) in the SDS. We show that He PIRSs become hot blue-subdwarf-like (sdO-like) stars after the SN impact and should be detectable in Ia SNRs. Hot blue subdwarfs are core helium-burning stars, and about half of them are in binary systems. The formation of single hot blue subdwarfs is still an open question (Heber, 2009), and the He-WD channel could be one source. He PIRSs may also contribute to the hypervelocity star (HVS) population (Wang & Han, 2010c), since the original orbital speed is very high at the time of the SN explosion in the He-WD channel. HVSs have extremely high space motions and can be unbound in our Galaxy; for example, US 708 has $v \sin i = 708 \pm 15$ km s^{-1} (Hirsch et al., 2005). We consider four different helium star progenitor models from the He-WD channel in Wang et al. (2009) (HeWDa, HeWDb, HeWDc, and HeWDd in Pan et al. (2010), hereafter Paper I) and perform three-dimensional hydrodynamics simulations of the impact of SN Ia ejecta using the method described in Pan et al. (2012b) (hereafter Paper II). Based on the hydrodynamics results, we carry out post-impact stellar evolution simulations using a method similar to the one described in Pan et al. (2012a) (hereafter Paper III). In the next section, the numerical codes and methods are described. Section 5.3 gives a detailed description of the He star progenitor systems in our calculations. In Section 5.4, we present the simulation results and the possible evolutionary tracks of He PIRSs. We discuss several effects on the post-impact evolution and the possibility of He PIRSs as sources of single hot blue subdwarfs and/or HVSs in Section 5.5. In the final section, we summarize our simulation results and conclude.

5.2 Numerical codes and methods

The simulation codes used in this paper are essentially the same as those in Papers II & III, including the three-dimensional hydrodynamics code FLASH[1] version 3 (Fryxell et al., 2000; Dubey et al., 2008), to simulate the impact of SN Ia ejecta on the binary companions, and the stellar evolution code, MESA[2] (Modules for Experiments in Stellar Astrophysics; Paxton et al. 2011, 2013), to create the progenitor models and simulate the post-impact evolution. We perform the SN Ia explosion simulations and post-impact stellar evolution calculations using a technique similar to the one described in Paper II, but we focus on the He-WD channel. To link FLASH's output with MESA's initial stellar models, we solve the hydrostatic equilibrium equation using a fourth-order Runge-Kutta solver with adaptive stepsize control, as described in Paper III. However, the assumption of ideal gas plus radiation equation of state (EOS) is no longer valid for He star companions, where the central density and temperature are much higher than in main sequence-like stars.

[1] `http://flash.uchicago.edu`
[2] `http://mesa.sourceforge.net`

Table 5.1: The progenitor models at the onset of the SN explosion

Model	M_0 ($M_\odot$)†	R_0 (10^{10} cm)	$\log_{10} L_0$ ($L_\odot$)	$\log_{10} T_{\rm eff,0}$ (K)	$P_{\rm orb,0}$ (sec)
HeWDa	0.697	0.63	1.30	4.61	1,033
HeWDb	0.803	1.10	1.62	4.57	2,257
HeWDc	1.007	1.35	2.11	4.64	2,682
HeWDd	1.206	1.61	1.09	4.35	3,410

† The mass (M_0), radius (R_0), luminosity (L_0), effective temperature ($T_{\rm eff,0}$), and orbital period ($P_{\rm orb,0}$) for different He star progenitor models at the time of the SN explosion, using the final masses in Wang et al. (2009).

We therefore update the EOS solver to include the OPAL, SCVH, and HELM EOS tables from the `eos` and `kap` modules in MESA.

5.3 He star progenitor systems

The progenitor models are taken from the HeWDa, HeWDb, HeWDc, and HeWDd helium star models in Paper I, but without the simplification of uniform composition. These four models were generated with initial masses equal to 1.25, 1.35, 1.4, and 1.8 $M_\odot$ and initial metallicity $Z = 0.02$. An artificial constant mass loss rate was adopted such that the evolution times and final helium-star masses were consistent with the detailed binary evolution models of Wang et al. (2009). Once the mass-loss phase ended, the stellar models were taken as initial models for the three-dimensional FLASH simulations. The physical properties of these four initial models are summarized in Table 5.1. All four helium star models were relaxed on the three-dimensional grid by artificially damping the gas velocity for five dynamical timescales, ensuring that our models started in hydrostatic equilibrium and reducing the geometrical distortion introduced by passing from one dimension to three dimensions. The entropy, composition, density, and temperature of these four helium stars at the onset of the SN Ia explosion are shown in Figure 5.1.

Using the numerical setup and initial conditions for SN Ia explosions described in Paper II, we performed three-dimensional FLASH simulations of SN Ia explosions in close binary systems with resolutions of 6/8 AMR levels (equivalent to a 1024^3 uniform grid and a zone size of $0.029 R_*$; see Paper II for definition). In Paper II, we performed a convergence study and concluded that this resolution would be sufficient to adequately describe the properties of post-impact companions. The initial binary systems were assumed to be in Roche-lobe overflow (RLOF), and the SN model used was the W7 model (Nomoto et al., 1984). Although SNe Iax are mostly sub-Chandrasekhar mass explosions, we chose the standard W7 explosion as the first case for comparison with our previous studies in Papers I and II. Since the mass loss from the non-degenerate star is sensitive to the detailed numerical setup of the SN model, we adopted the "W7 SN"

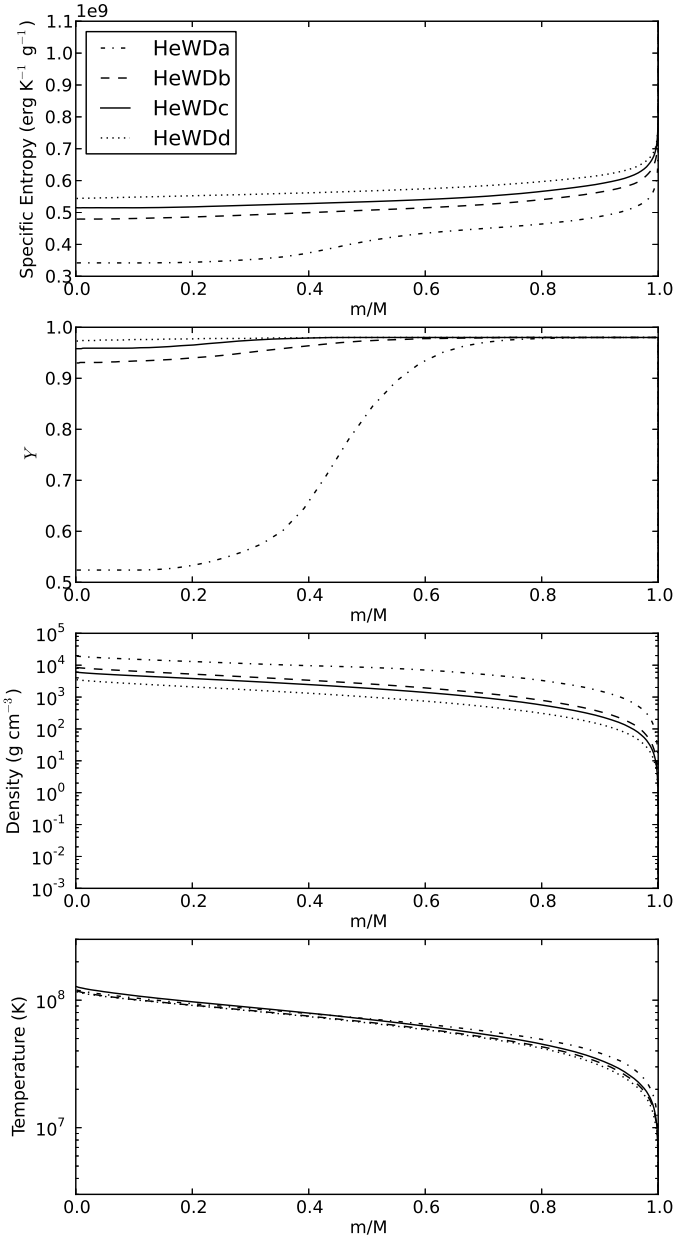

Figure 5.1: The initial specific entropy, helium composition (Y), density, and temperature profiles as functions of the fractional mass before the SN Ia explosion for models HeWDa, HeWDb, HeWDc, and HeWDd in Table 3.1.

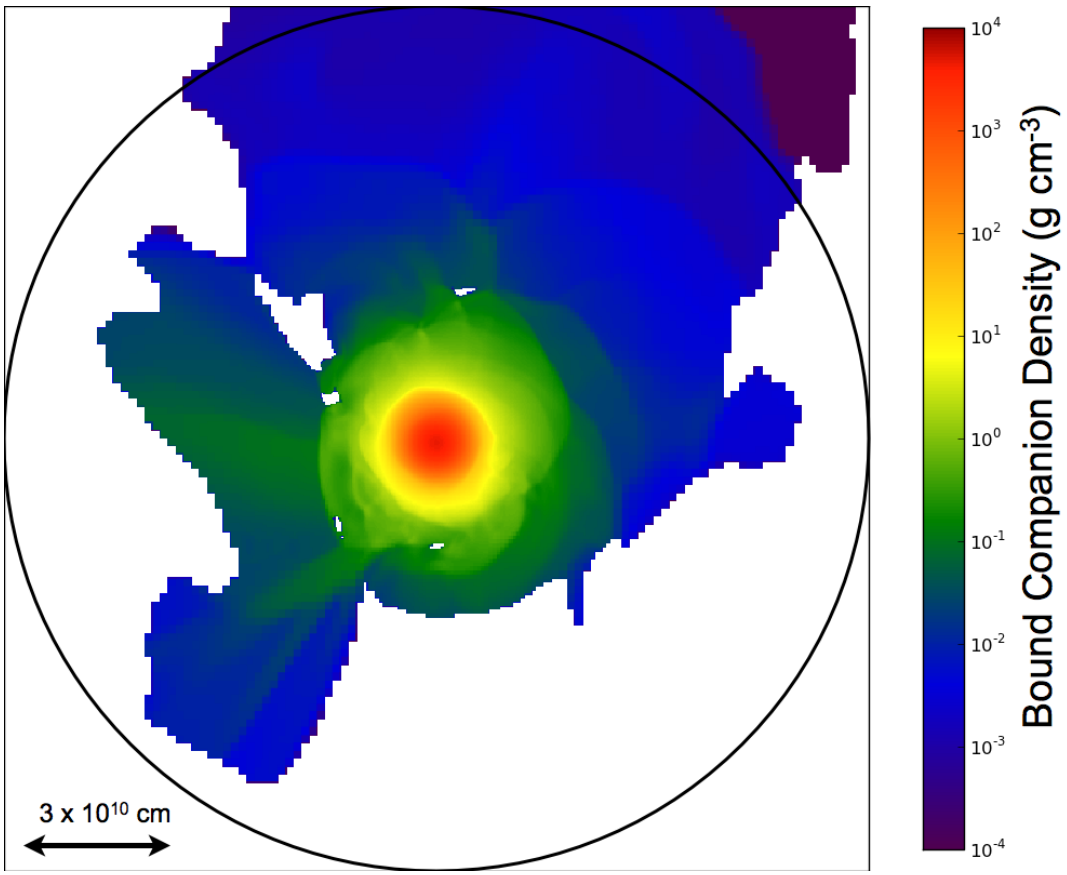

Figure 5.2: Bound gas density distribution in the orbital plane for a three-dimensional SN Ia simulation with the model HeWDc in Table 3.1 at time 3106 sec after the explosion. The black circle shows the maximum distance ($r_{\rm max} = 8.83 \times 10^{10}$ cm) which is used for the one-dimensional model reconstruction.

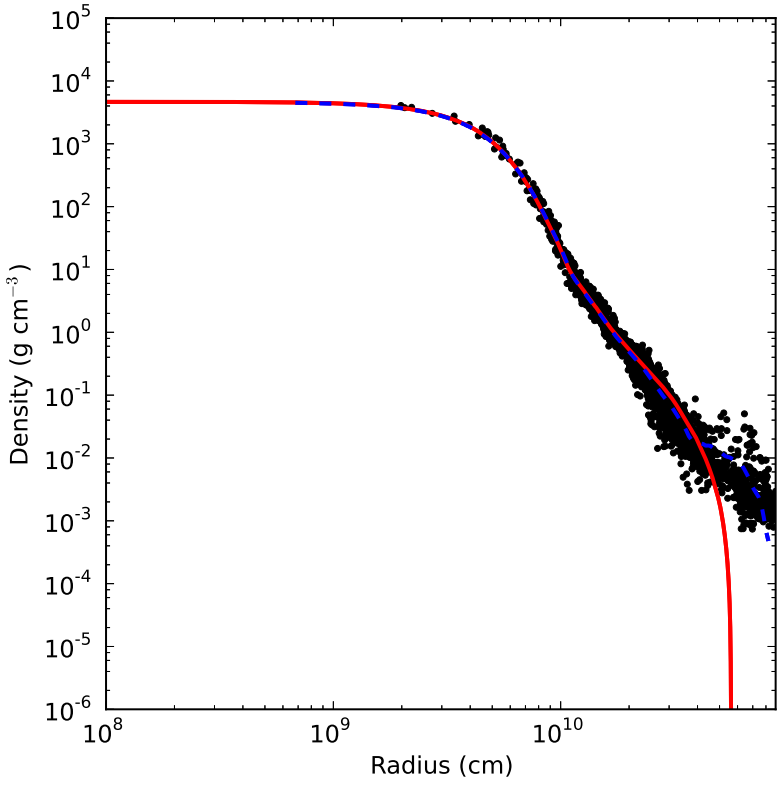

Figure 5.3: Bound gas density versus radius distribution for the model HeWDc in Table 3.1 at time 3106 sec after the explosion. Black dots represent the scattered values before angle-averaging (randomly selected 1/512 of total data points). The blue dashed line represents the angle-averaged radial profile. The solid red line indicates the relaxed hydrostatic solutions in MESA.

sub-grid model, which has a power-law density distribution and a constant temperature distribution in radius that matches the exploding mass and energy in the W7 model (see Paper II for detailed descriptions).

After the SN Ia impact, the helium star binary companion loses about $\sim 4-6\%$ of its mass and is heated, the degree to which depends on the progenitor model (see Table **??**). In addition, because of the shock interaction during the SN Ia impact, the central density of the helium star decreases to $\sim 20-30\%$ of its original value, and the central temperature decreases by $\sim 10-15\%$, except for model HeWDa. Before the SN impact, the HeWDa model has a lower central helium composition than the other three models due to central helium burning, causing a higher positive entropy gradient at about $m/M_* \sim 0.5$. Therefore, in this model the central density decreases 22% during the SN impact, while the central temperature increases by 12%.

Figure 5.2 shows the bound gas density distribution for model HeWDc in the orbital plane at the end of the simulation ($t = 3,106$ sec). Since the companion star has a high linear speed and will eventually reach the edge of the simulation box, we cannot simulate the evolution for a sufficiently long time for the companion to be fully in hydrostatic equilibrium. However, we can assume the specific entropy and composition profiles are conserved if the system is adiabatic. To calculate the specific entropy and composition profiles, a large spherical region is considered (the black circle in Figure 5.2) and then divided into $128-256$ radial bins. Figure 5.3 shows the comparison of angle-averaged bound density radial profile with the scattered 3D data points, and relaxed hydrostatic profiles for the model HeWDc. It is clear to see that the angle-averaged profiles and the location of photosphere are consistent with our reconstructed hydrostatic model which will described in the next paragraph. Figure 5.4 shows the angle-averaged one-dimensional radial post-impact profiles of the specific entropy, helium composition, density and temperature at the end of the FLASH simulations. Note that the SN ejecta and unbound companion mass are optically think at the end of the FLASH simulations. However, the ejecta will become transparent in the optical waveband and the surviving stars should be detectable after several months.

With the `eos` (equation of state) and `kap` (opacity) module in MESA, we used the post-impact specific entropy profiles and composition profiles to construct hydrostatic models by solving the continuity and hydrostatic equations for the density ρ, pressure P, and radius r as functions of the enclosed mass m:

$$\frac{dr}{dm} = \frac{1}{4\pi r^2 \rho} \tag{5.1}$$

$$\frac{dP}{dm} = -\frac{Gm}{4\pi r^4} \ . \tag{5.2}$$

The entropy of each mass element was kept fixed, except that the entropy profiles were flattened in the

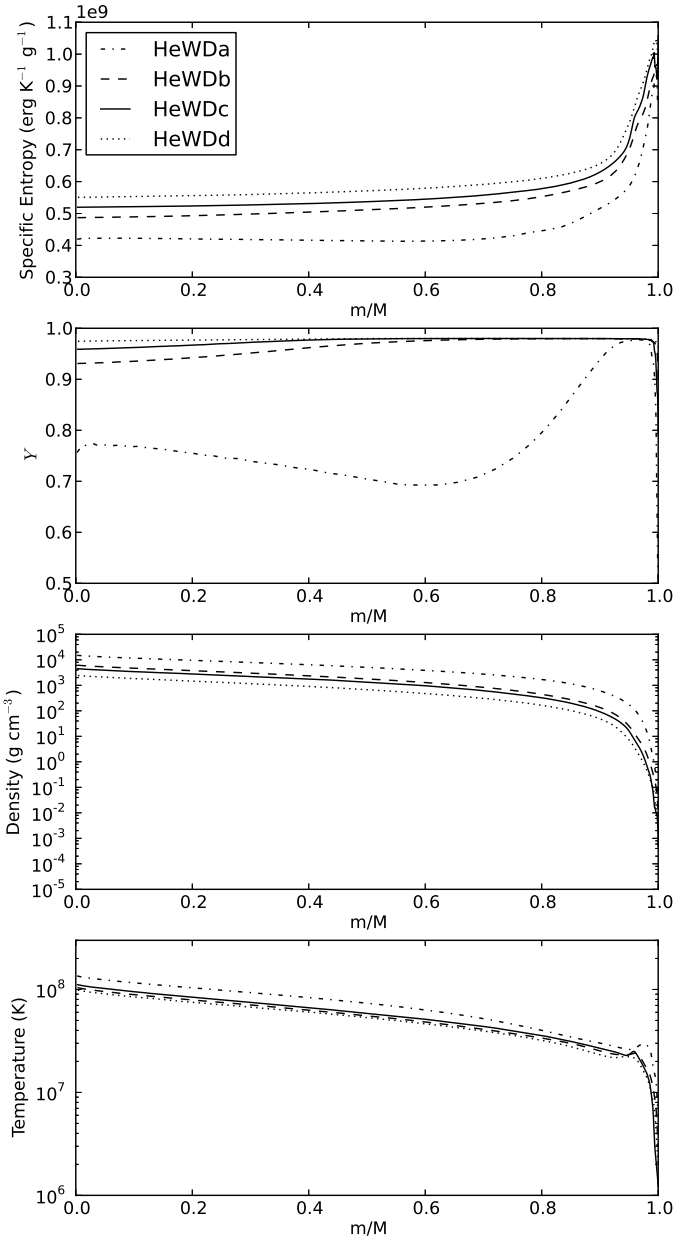

Figure 5.4: Similar to Figure 5.1 but for post-impact angle-averaged profiles at the end of the FLASH simulations.

Table 5.2: The progenitor models immediately after the SN impact

Model	$M_{\rm SN}^{\dagger}$ ($M_\odot$)	$(\Delta M/M_0)$	$R_{\rm SN}$ (10^{10} cm)	$(R_{\rm SN}/R_0)$	$\log_{10} L_{\rm SN}$ ($L_\odot$)	$\log_{10} T_{\rm eff,SN}$ (K)	$v_{\rm linear,SN}$ (km sec^{-1})	$M_{\rm Ni}$ ($10^{-4} M_\odot$)	$E_{\rm in}$ (10^{49} erg)
HeWDa	0.656	5.88 %	2.71	4.30	0.265	4.03	734	15.0	1.3
HeWDb	0.748	6.85 %	3.93	3.58	0.510	4.01	550	2.38	1.3
HeWDc	0.962	4.47 %	5.63	4.17	0.792	4.01	509	5.64	1.5
HeWDd	1.126	6.6 3%	7.24	4.50	1.16	4.03	446	1.75	1.7

† The mass ($M_{\rm SN}$), mass change ($\Delta M \equiv M_{\rm SN} - M_0$), radius ($R_{\rm SN}$), luminosity ($L_{\rm SN}$), effective temperature ($T_{\rm eff,SN}$), linear spatial velocity ($v_{\rm linear,SN}$), mass of bound nickel ($M_{\rm Ni}$) , and energy deposition from the SN ejecta ($E_{\rm in}$) of initial relaxed post-impact hydrostatic models in MESA.

outermost region ($0.995 < m/M_* < 1$) to avoid negative entropy gradients. For the HeWDa model, the composition profile was adjusted to a uniform distribution due to the strong mixing during the SN impact and to avoid negative entropy and composition gradients. The hydrostatic solutions were taken as initial conditions for the models used in MESA.

The initial luminosity profile for MESA was estimated using the radiative temperature gradient expression,

$$L(m) = -\frac{(4\pi r^2)^2 ac}{3\kappa}\frac{dT^4}{dm} \ , \tag{5.3}$$

where κ is the opacity, a is the radiation constant, and c is the speed of light. Since our initial luminosity profile is based on an assumption of radiative equilibrium and our surface profiles are not as sharp as the standard surface profile in MESA, the calculated photospheric luminosity and effective temperature were very rough at the beginning and needed to be relaxed in MESA. A fixed time step, $\Delta t = 10^{-8}$ years, was enforced for the first 10^{-6} years to relax the models. After 10^{-6} years, we allowed the time step to be automatically determined in MESA.

Figure 5.5 shows the specific entropy, helium composition, density, and temperature profiles of the relaxed helium star models in MESA. The relaxed hydrostatic helium star models differ somewhat in the photospheric luminosity and effective temperature, but the stellar radius and interior density and temperature profiles are nearly the same as in the original models. Figure 5.6 shows the changes of mass and radius before and after SN impact. Although He PIRSs only lose a few percent of their masses, post-impact radii increase by a factor of ~ 4 (see Table 5.2). These changes in radius dramatically alter the He PIRSs.

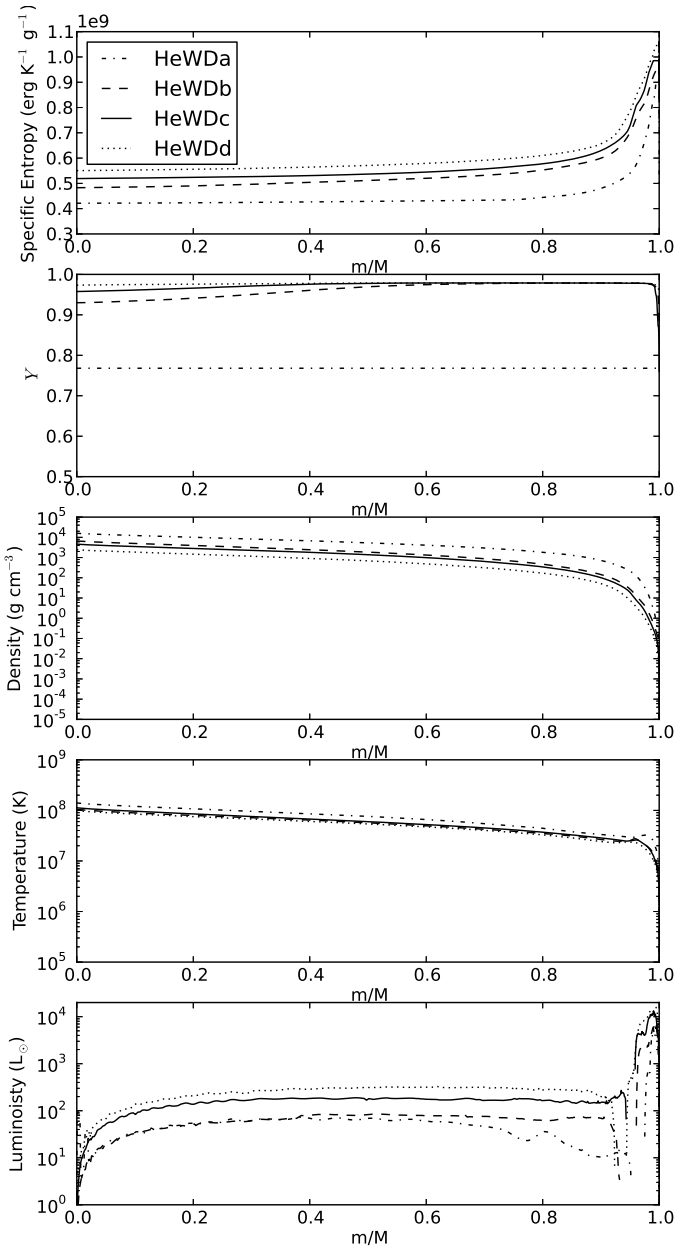

Figure 5.5: Relaxed post-impact companion models in MESA for specific entropy, helium composition (Y), density, temperature, and enclosed luminosity as functions of the fractional mass for models HeWDa, HeWDb, HeWDc, and HeWDd in Table 5.2.

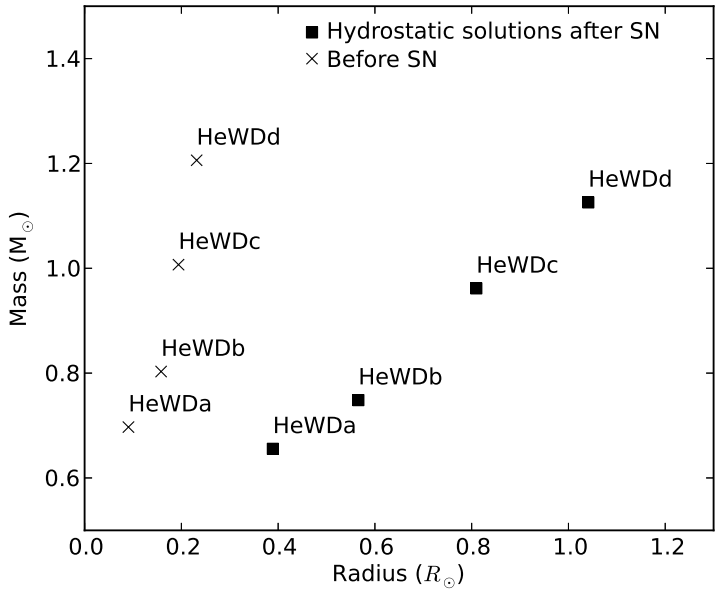

Figure 5.6: Stellar mass and radius for all considered helium star models before (crosses) and after (filled squares) supernova impact.

5.4 Post-impact evolution

Once we have the relaxed hydrostatic stellar models, the post-impact evolution of He PIRSs can be easily calculated in MESA. In this section, we describe this evolution. Hertzsprung-Russell (H-R) diagrams of post-impact evolutionary tracks of He PIRSs are presented in luminosity versus effective temperature, surface gravity versus effective temperature, and color-magnitude forms, providing diagnostics for searches in future observations for He PIRSs in Ia SNRs.

5.4.1 Evolutionary tracks

Similarly to the MS-like PIRSs in Paper III, the He PIRSs expand rapidly and dramatically due to the release of energy deposited by the SN impact. Figure 5.7 shows the evolution of the photospheric radius, luminosity, and effective temperature as functions of time. All He PIRSs expand on a timescale of $\sim 10-30$ years, depending on their progenitor models. These expansion rates are determined by the local radiative diffusion timescale (Henyey & L'Ecuyer, 1969), which is associated with not only the stellar structure, but also the amount and depth of SN energy deposition. Since He stars are more compact than MS-like stars, the depths of energy deposition are shallower, causing a shorter local radiative diffusion timescale. Therefore, heat transfer initially occurs more rapidly than the thermal expansion. The effective temperature

starts to increase at $\sim 10^{-2} - 10^{-1}$ years and then continues increasing for another $10^{0} - 10^{1}$ yr up to $\sim 30,000 - 50,000$ K. Subsequently, the surfaces of the He PIRSs cool off to $\sim 10,000 - 30,000$ K on a timescale of ~ 10 years due to the expansion. The stars quickly become luminous helium OB stars ($L \sim 10^{3} - 10^{4} L_{\odot}$). When the deposited energy has radiated away, the photospheric radii reach maximum values at around $\sim 10 - 30$ yrs. Subsequently, the stars contract and release gravitational energy, turning them into sdO-like stars for $\sim 10^{7}$ years. After $\sim 10^{7}$ years, the core helium of He PIRSs should be exhausted, and the stars should evolve to the helium red giant phase. The simulations are terminated at $\sim 10^{5}$ years, since the SN Ia remnant may not be recognizable after this time.

We have noticed that there is $\lesssim 1\%$ artificial mass loss during angle-averaging of the post-impact density, since the helium star is close to the edge of the simulation box at the end of the FLASH simulations. However, the most important factors that control the post-impact evolution are the amount of energy deposited and the corresponding depth, which are mainly concentrated in the outer 5% of mass (see the temperature bump in Figure 5.4). We have tested the effect of mass loss by changing the mass of the post-impact remnant star and conclude that the artificial mass loss will not lead to a notable difference in the post-impact evolution.

The evolutionary tracks of He PIRSs in the H-R diagram are plotted in Figures 5.8 and 5.9, representing the effective temperature versus luminosity and effective temperature versus surface gravity, respectively. Based on our post-impact simulations, we predict that He PIRSs will evolve to luminous OB stars on a timescale of ~ 30 years and will fade within a hundred years. Therefore, only in young SN Ia remnants can one observe luminous helium OB stars at the center of the SNR if the non-degenerate companion was a He star. However, an sdO-like star is observable for the remaining time. Note that for the He-WD channel in the SDS the delay time ($\sim 45 - 220$ Myr, Wang & Han 2010b) is much shorter than in other SDS channels since the helium star was formed from a more massive star. This suggests that He PIRSs are expected to be detected only in star-forming regions.

As SNe Iax represent a sub-class of sub-luminous SNe Ia, their explosion energy and ejecta speed are lower than in the standard W7 model, causing a reduced effect of the SN impact on binary companions. In Paper III, we studied the effect of the SN explosion energy on the post-impact evolution and found that the explosion energy dramatically affects the amount and depth of SN energy depositition in MS-like PIRSs. For a lower explosion energy, the effect of the SN impact is shallower, causing a shorter radiative diffusion timescale. However, these differences become small once the deposited energy has radiated away. Therefore, for He PIRSs with sub-luminous explosions, He PIRSs behave similarly after ~ 30 years, but with less mass lost during the SN impact.

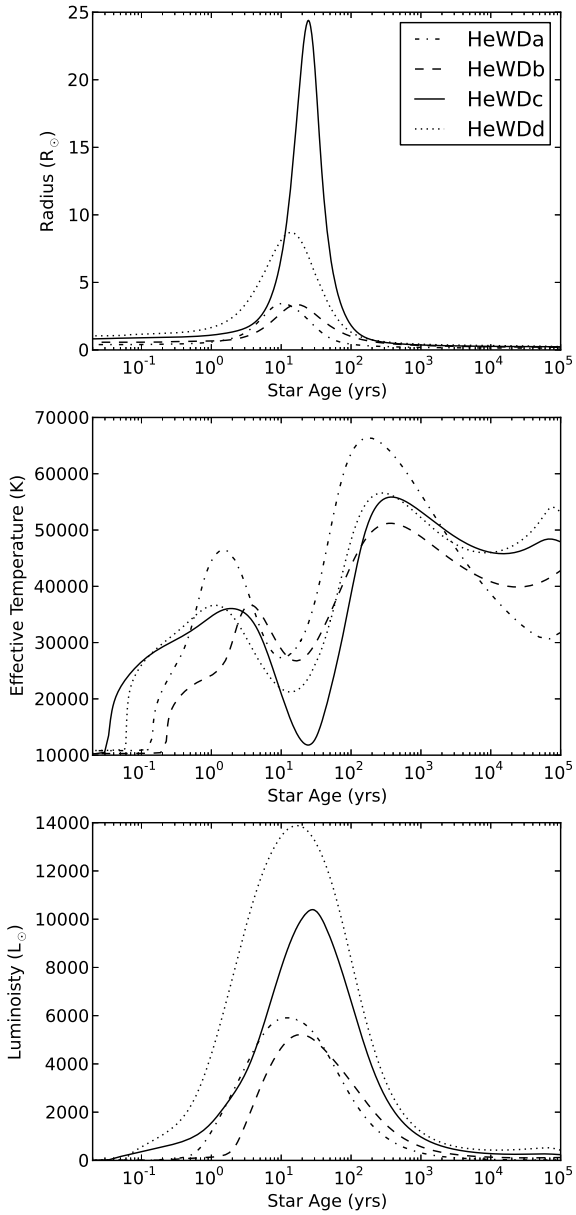

Figure 5.7: Evolution of the photospheric radius, effective temperature, and luminosity as functions of time. Each line shows the evolution of a He PIRS in Table 5.2.

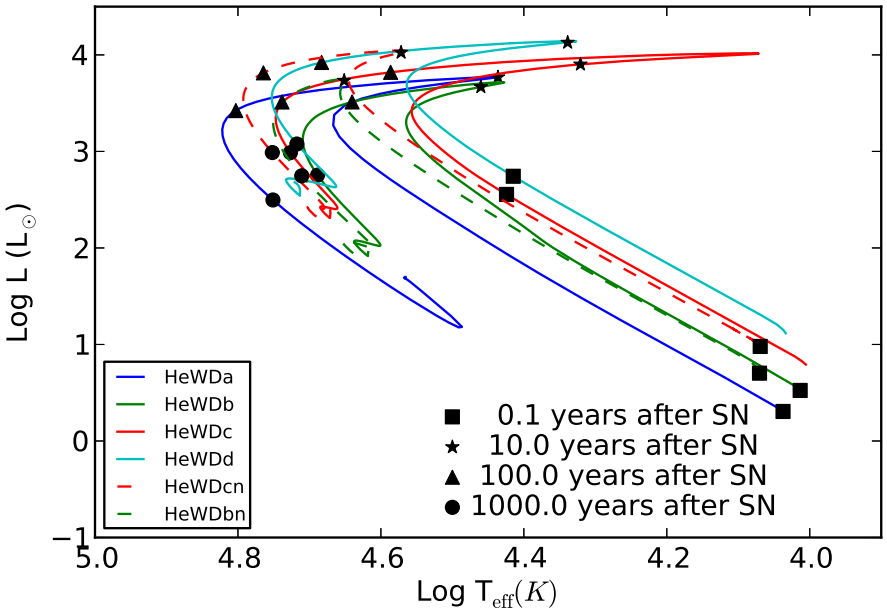

Figure 5.8: Evolutionary tracks in the H-R diagram for different He PIRS models. Each line represents an evolutionary track of a He PIRS in Table 5.2 over an interval of 10^5 years. The filled squares indicate the conditions at 0.1 years after the SN impact; filled stars, 10 years after the SN impact; filled triangles, 10^2 years after the SN impact; filled circles, 10^3 years after the SN impact. The He PIRS models with letter "n" represent the cases without nickel contamination (with dashed lines).

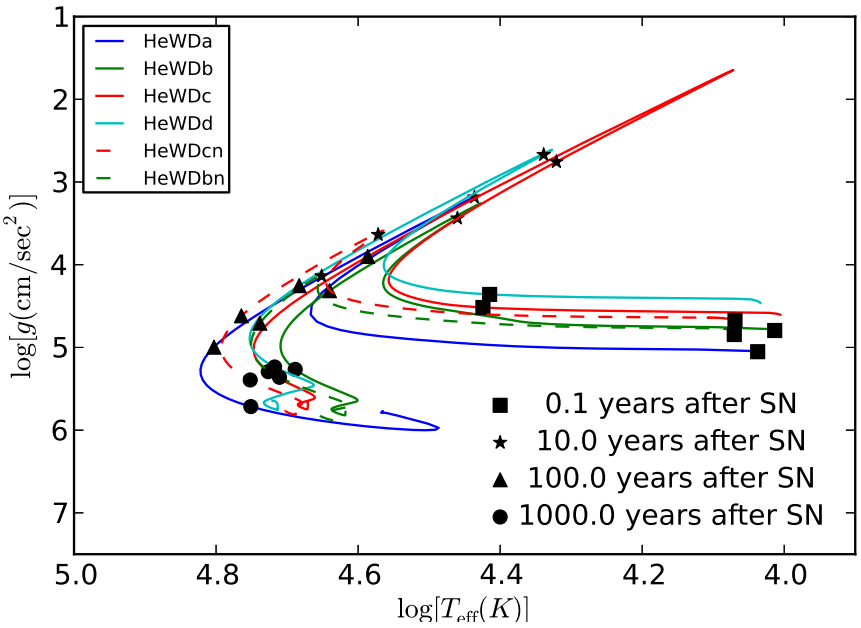

Figure 5.9: Similar to Figure 5.8 but for surface gravity (in cgs units) versus effective temperature (K).

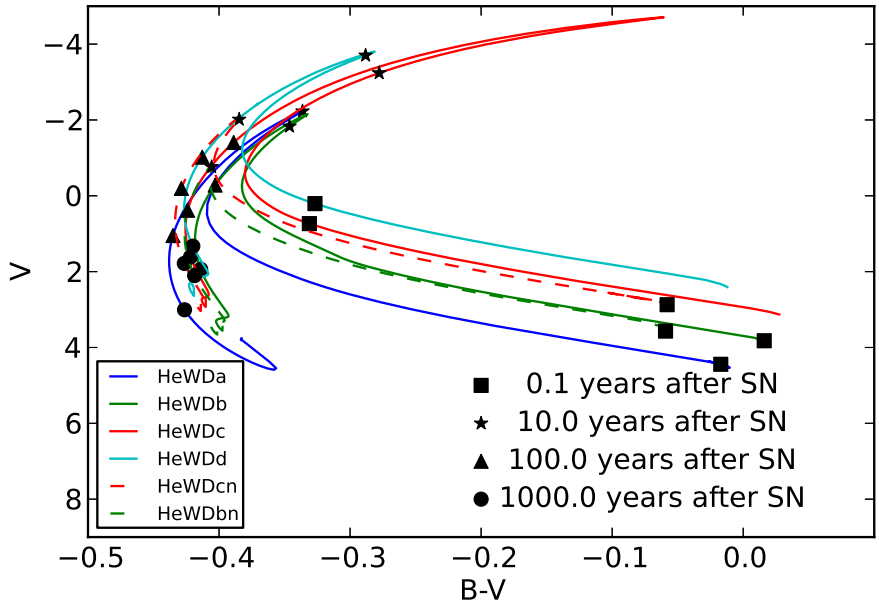

Figure 5.10: Similar to Figure 5.8 but for V magnitude versus B-V color. The magnitudes are absolute magnitudes using the broadband u and v filters in the AB magnitude system.

5.4.2 Color-magnitude diagram

For direct comparison with observations, we convert the luminosity to magnitude in the optical bands. Given the effective temperature ($T_{\rm eff}$) and photospheric radius (R) of a PIRS, the magnitude of the PIRS can be calculated using Equation 6.1 with an assumption of blackbody radiation:

$$m_{S_\lambda} = -2.5 \log_{10} \left[\frac{\int S_\lambda (\pi B_\lambda) d\lambda}{\int (f_\nu^0 c/\lambda^2) S_\lambda d\lambda} \left(\frac{R}{d} \right)^2 \right], \tag{5.4}$$

where S_λ is the sensitivity function of a given filter at wavelength λ, B_λ is the Planck function, d is the distance of the PIRS, and $f_\nu^0 = 3.631 \times 10^{-20}$ erg cm^{-2} s^{-1} Hz^{-1} is the zero-point value in the AB magnitude system. Figure 5.10 shows the color-magnitude evolutionary trajectories of He PIRSs. The absolute magnitudes are calculated using the broadband u and v filters.

5.5 Discussion

In this section, we study the possible observational effects of the post SN impact evolution. In particular, we examine the effect of nickel contaminations from the supernova ejecta on the post-impact evolution. The surface rotational speeds of He PIRSs during post-impact evolution are also predicted as functions of time.

Furthermore, we also discuss the possibility that He PIRSs could be a source of single sdO stars and/or HVSs.

5.5.1 Nickel contamination

The envelope of a companion star could be contaminated by the supernova ejecta during the supernova impact or as fallback. In Paper II, we have shown that this nickel contamination is much greater for He PIRSs ($1.7 \times 10^{-4} M_{\odot} - 1.5 \times 10^{-3} M_{\odot}$; see Table 5.2) than MS-like PIRSs ($< 10^{-5} M_{\odot}$). We note that the nickel contamination can affect the post-impact evolution for He PIRSs, since the change of metallicity in the envelope will also change the opacity and radiative diffusion timescale. To study this effect, two He PIRSs (labeled "HeWDbn" and "HeWDcn") without nickel contamination have been reconstructed by removing the bound nickel at the end of the FLASH simulations. The hydrostatic profiles of the reconstructed models do not change significantly, but they have slightly smaller radii. Figure 5.11 shows the evolution of the photospheric radius, effective temperature, and luminosity of these two models with and without (cases with the letter "n") nickel contamination. Removing the bound nickel causes the opacity to be lower in the outer regions, making stars more transparent and causing smaller photospheric radii. It is clear that the maximum radii of He PIRSs without nickel contamination are much smaller than the same He PIRSs with nickel contamination. Note that we used the fixed metal tables (Type I) opacity module in MESA. Thus, the opacity contributed by heavy metals in our calculations is not very accurate, since the abundance ratios are different in the nickel-contaminated region than the abundances assumed in OPAL. However, the difference between models with and without nickel contamination is not very significant in the H-R diagrams (see Figure 5.8). Thus, these differences can be treated as an uncertainty in our post-impact simulations.

Energy generation by ^{28}Ni decay and ^{28}Co decay in the SN ejecta-contaminated regions is neglected in our calculations. This is justified by the fact that the energy generated by these nuclear decays is much smaller than the energy deposited from the supernova ejecta since the mass of bound nickel is small.

5.5.2 Surface rotational speed

In Paper III, we showed that the surface rotational speed could decrease to $\sim 10 - 20$ km s^{-1} for MS-like PIRSs, if the specific angular momentum is conserved during the post-impact evolution. This result implied that the possible PIRS candidate Tycho G could not be completely ruled out because of its low surface rotation speed. Here, we apply the same method to He PIRSs. The He stars were set into rigid rotation at the beginning of the FLASH simulations because the synchronization time due to tidal locking for a given mass ratio q and orbital period P (Zahn, 1977), $t_{\rm sync} \sim 10^4((1+q)/2q)^2 P^4$ yrs $\ll 1$ day, is extremely

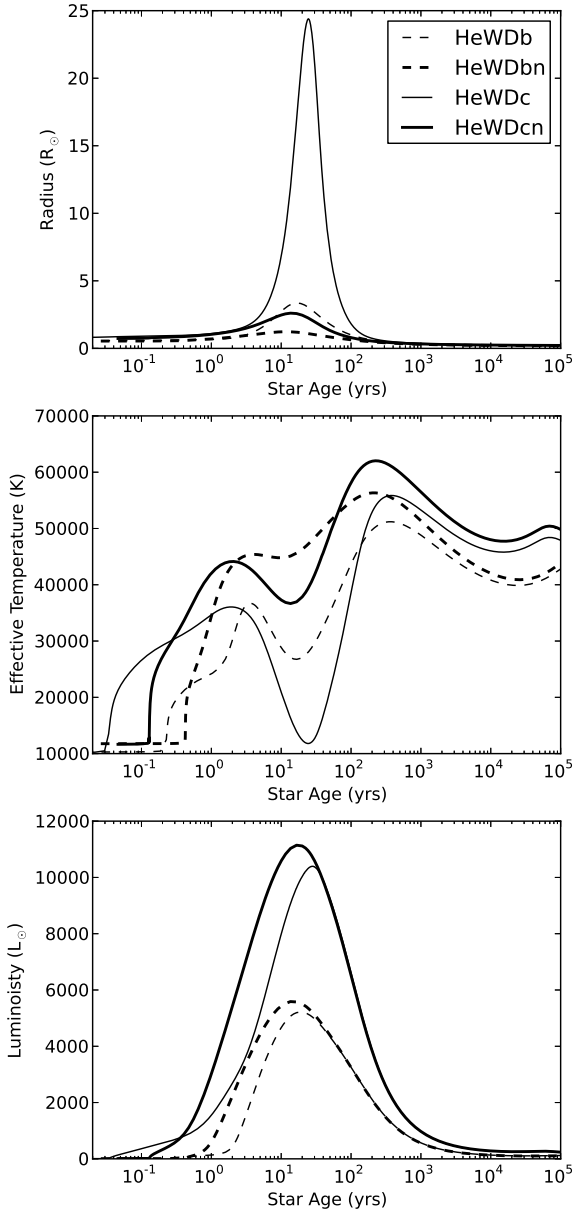

Figure 5.11: Similar to Figure 5.7, but for HeWDb and HeWDc with and without nickel contaminations. The letter "n" in He PIRS models represents the cases without nickel contamination.

short in the He-WD channel. After the SN impact, a He PIRS loses $\lesssim 10\%$ of its angular momentum and is no longer in a state of rigid-body rotation. Thus, an angle-averaged, post-impact radial angular velocity profile can be calculated by averaging different latitudes and longitudes in spherical coordinates in the FLASH output. The post-impact surface rotational speed can be calculated by assuming the specific angular momentum to be conserved after the SN impact. Figure 5.12 shows the post-impact evolution of the surface rotational speed versus evolution time. It is found that the angle-averaged angular velocity profiles exhibit some variations in the envelope region, and we estimate the uncertainty by using the standard deviation of the specific angular momentum within the envelope. Since He stars are more compact and are closer to the accreting WD at the time of the SN explosion, the surface rotational speed should be much higher than for MS-like companions in the MS-WD channel. The surface rotational speed at the time of the SN Ia explosion could be as high as ~ 200 km s^{-1} if the He star companion is close to co-rotation due to tidal locking. For He PIRSs, our calculations show that the surface rotational speed should decrease to $\lesssim 10$km s^{-1} when the star expands to its maximum size. However, because the radiative diffusion timescale is short, the surface rotational speed is slow only during the first hundred years and will eventually increase to ~ 100 km s^{-1} after a few hundred years. Therefore, if He PIRSs exist in historical Ia SNRs, their surface rotational speeds could be higher than 50 km s^{-1}, depending on the progenitor models and the ages of the SNR.

5.5.3 He PIRSs as hypervelocity stars?

During the past decade a number of HVSs have been observed in the halo of our Galaxy. They are subluminous O- or B-type stars or MS B stars with high radial velocities that could exceed the escape velocity of the Milky Way. The common explanation for their formation involves tidal ejection in binary stars (or triple stars) associated with either a massive black hole or binary black holes (Hills, 1988; Yu & Tremaine, 2003). Alternatively, Wang & Han (2009) suggest that the surviving He PIRSs in SNe Ia within the He-WD channel could be a source of HVSs. In our calculations, He PIRSs are sdO-like stars for $\sim 10^7$ yr and thereafter evolve to the helium red-giant phase. The final linear velocity (original orbital velocity plus kick velocity) of our He PIRSs is $\sim 400 - 800$ km s^{-1} (see Table **??**). He PIRSs could move to a distance of ~ 10 kpc within 10^7 years, becoming single sdO-like stars in the halo of our Galaxy, if the Ia SNRs have diffused away at that time. The HVS US 708 (or HVS2) has a radial velocity $v \sin i = 708 \pm 15$ km s^{-1}, $T_{\rm eff} = 44,500$ K, $\log g = 5.23$, and Galactic latitude $b = +47.05^\circ$ at a distance of 19 kpc (Hirsch et al., 2005), giving a displacement of 14 kpc from the Galactic plane. The effective temperature and surface gravity of US 708 are consistent with our He PIRS models, but they require a subdwarf lifetime longer than several

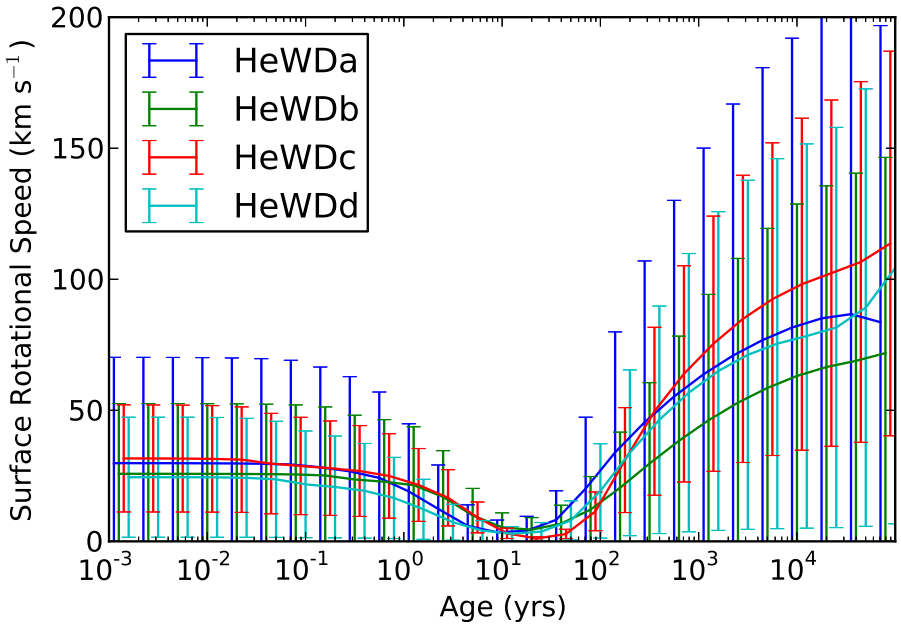

Figure 5.12: Evolution of surface rotational speed for all He-WD models in Table 5.2. The error is estimated using the variation of specific angular momentum within the envelope of initial hydrostatic solutions (see Section 5.5.2 for detailed description). The number of error bars is only chosen for visualization and does not represent the actual number of data points.

times 10^7 yr to reach such a distance, if the SN exploded in the Galactic plane. Therefore, a less massive model may better match US 708, since less massive models have higher linear speeds and longer subdwarf lifetimes.

5.6 Conclusions

We have investigated the post-impact evolution of He PIRSs within the SDS for SNe Ia via numerical simulations. Four helium star models from Wang et al. (2009) are considered in our calculations. We performed three-dimensional hydrodynamics simulations using the methods that were described in Paper II. The post-impact evolution of these stars has been studied by reconstructing hydrostatic models based upon the final output in the hydrodynamics simulations and then interpolating them into a one-dimensional stellar evolution code, MESA. It is found that He PIRSs expand dramatically and evolve to become luminous OB stars within about $\sim 10 - 30$ years after the SN Ia explosion. This phase is short (< 100 years), and therefore these luminous OB stars are not likely to be detected in historical Ia SNRs. After ~ 30 years, He PIRSs contract and evolve into hot blue-subdwarf-like (sdO-like) stars due to the release of gravitational energy. Therefore, we predict that most He PIRSs should be sdO-like stars and could be detectable in nearby

Ia SNRs.

We also predict that these He PIRSs should be rapidly rotating ($v_{\rm rot} \gtrsim 50$ km s^{-1}). Although a few fast rotating hot blue-subdwarfs have been observed recently (Geier et al., 2011, 2013), most single hot blue-subdwarfs (sdOs and sdBs) are slowly rotating (Geier & Heber, 2012). If single hot blue-subdwarfs originate from the merger of two He WDs (sdOs/sdBs; Heber, 2009), merger via a common envelope phase on the red giant branch (Politano et al., 2008), or the He-WD channel in SNe Ia (sdOs), the theoretical predictions cannot explain these observations, suggesting that other mechanisms operate to slow down the rotation, such as magnetic braking.

The He-WD binary channel is favored for the prompt DTD in the SDS and is expected to occur in star-forming regions. Since the orbital period immediately prior to the SN Ia explosion in the He-WD channel is extremely short ($\lesssim 1$ hour), the system is expected to be tidally locked. Thus, He stars should be rapidly rotating at the time of the SN Ia explosion. Although some angular momentum will be lost during the SN impact, He PIRSs are still expected to be rapidly rotating after ~ 30 years. The spatial velocity of He PIRSs is also expected to be high, reflecting the high orbital speed at the time of the SN Ia explosion and implying that He PIRSs could contribute to the HVS population (i.e. US 708).

Chapter 6

Search for Surviving Post-Impact Remnant Stars in Type Ia Supernova Remnants

Abstract

The nature of the progenitor systems of Type Ia supernovae is still unclear. One way to distinguish between the SDS and DDS is to search for the surviving Post-Impact Remnant Stars (PIRSs). Using our stellar evolution simulations of main-sequence- (MS-) and helium-rich- (He-) PIRSs, we predict the color and magnitude of MS- and He-PIRSs as functions of time. We also discuss PIRS candidates in Galactic Type Ia supernova remnants (Ia SNRs), including SN 185, SN 1006, SN 1574, SN 1604, and G1.9+0.3, and nearby extragalactic Ia SNRs. We find that the maximum detectable distance of MS PIRSs (He PIRSs) is $0.6-4$ Mpc ($0.4-16$ Mpc), if the apparent magnitude limit is 27 and we assume no extinction, suggesting the Large and Small Magellanic Clouds (LMC/SMC) and the Andromeda Galaxy (M31) are excellent environments in which to search for PIRSs.

6.1 Introduction

Type Ia supernovae (SNe Ia) are treated as "standardizable candles" for use in determining the values of key cosmological parameters (e.g. the Hubble constant H_0). However, these cosmological applications are based on the assumption that the homogeneity of low-redshift SNe Ia can be applied to high-redshift SNe Ia as well. This assumption is questionable until we fully understand the progenitor systems of SNe Ia and their intrinsic variations. Furthermore, recent *Planck* results show that the best-fit Hubble constant ($H_0 = 67 \pm 1.2$ km sec^{-1} Mpc^{-1}; Planck Collaboration et al. 2013) is notably lower than the value determined by WMAP9 ($H_0 = 69.7 \pm 2.4$ km sec^{-1} Mpc^{-1}; Hinshaw et al. 2012) , Cepheid variables ($H_0 = 74.3 \pm 1.5 \pm 2.1$ km sec^{-1} Mpc^{-1} by Freedman et al. 2012), and SNe Ia ($H_0 = 73.8 \pm 2.4$ km sec^{-1} Mpc^{-1} by Riess et al. 2011). The origin of this inconsistency of the Hubble constant from forward analysis (using SNe Ia and Cepheids) and backward analysis (using the Cosmic Microwave Background; CMB) is still unclear. Therefore, to improve cosmological constraints, it is crucial to examine the progenitors of SNe Ia.

It is generally believed that SNe Ia are the results of thermonuclear explosions of carbon-oxygen (CO) white dwarfs (WDs) with masses close to the Chandrasekhar mass ($M_{\rm WD} \sim 1.4 M_{\odot}$). These thermonuclear explosions could be triggered by either merger of two WDs with total mass greater than the Chandrasekhar mass (the double-degenerate scenario; DDS; Iben & Tutukov 1984; Webbink 1984) or by accretion from a normal non-degenerate star through Roche-lobe overflow (RLOF; the single-degenerate scenario; SDS; Whelan & Iben 1973; Nomoto 1982). Both scenarios have their own advantages and disadvantages. For instance, the exploding WDs in the SDS are all close to the Chandrasekhar mass, implying the homogeneity of SNe Ia is natural in this scenario, but the non-degenerate companions in the SDS are usually hydrogen- and helium-rich. On the other hand, the DDS naturally explains the absence of hydrogen and helium lines, but violent mergers of massive binary WDs may lead to accretion-induced collapses (AIC) instead of thermonuclear explosions, and low-mass WD mergers may not produce enough nickel to power SN Ia light curves. In the SDS, the binary companions could have many different stellar types, including main-sequence (MS) stars, red giants (RGs), and helium-rich (He) stars. However, it is still unclear which channel(s) in the SDS and DDS dominate(s) the SNe Ia (Hillebrandt et al., 2013).

Based on recent multi-dimensional hydrodynamics simulations (Marietta et al., 2000; Pakmor et al., 2008; Pan et al., 2010, 2012b; Liu et al., 2012, 2013), the non-degenerate companions in the SDS should survive the SN impact and could be detectable. Therefore, one of the simplest ways to distinguish between the SDS and DDS is to search for surviving Post-Impact Remnant Stars (PIRSs) in SN Ia remnants. In Pan et al. (2010) and Pan et al. (2012b), we have examined the effects of SN impact on the non-degenerate binary companions in the SDS for MS star, RGs, and He star binary companions via multi-dimensional hydrodynamics simulations. The evolution of surviving MS-like and helium-rich Post-Impact Remnant Stars (PIRSs) is also investigated in Pan et al. (2012a, 2013). In this Chapter, we extend these numerical simulations to observable quantities such as magnitudes and color, and further discuss the possibility of searching for PIRSs in nearby SN Ia remnants (Ia SNRs). In the next section, we present our numerical predictions and compare them with nearby Ia SNRs in our Galaxy (Section 6.3), the Large and Small Magellanic Clouds (LMC and SMC; Section 6.4), and other nearby galaxies (Section 6.5). In the final section, we summarize our numerical predictions and conclude.

6.2 Numerical predictions

In our stellar evolution simulations of MS- and He-PIRSs, the bolometric luminosity (L), effective temperature ($T_{\rm eff}$), and photospheric radius (R) are straightforward to compute and could be directly determined

in the stellar evolution code MESA[1] (Modules for Experiments in Stellar Astrophysics; Paxton et al. 2011, 2013). Therefore, converting the bolometric luminosity to broadband magnitudes is one of the simplest ways to make direct comparison with optical observations. Additional observable quantities such as the strength of absorption lines require more complicated stellar atmosphere models and detailed radiation transfer. Thus, we cannot predict these observational effects on the PIRSs at this moment but will instead consider them in future work.

Given the effective temperature and photospheric radius of a PIRS, the magnitude (m_S) of the PIRS can be calculated using Equation 6.1 with an assumption of blackbody radiation:

$$m_S = -2.5 \log_{10} \left[\frac{\int S_\lambda (\pi B_\lambda) d\lambda}{\int (f_\nu^0 c/\lambda^2) S_\lambda d\lambda} \left(\frac{R}{d} \right)^2 \right], \tag{6.1}$$

where S_λ is the sensitivity function of a given filter at wavelength λ, B_λ is the Planck function, d is the distance of the PIRS, and $f_\nu^0 = 3.631 \times 10^{-20}$ erg cm^{-2} s^{-1} Hz^{-1} is the zero-point value in the AB magnitude system. Figure 6.1 shows the sensitivity functions of several different filters we considered in this study, including the popular Johnson-Cousins-Glass UBVIR system (upper panel) and HST/WFC3 system (lower panel).

Figure 6.2 and Figure 6.3 show the Hertzsprung-Russell (H-R) diagram in different representations and different bands. He- PIRSs are sdO-like stars that show stronger emission in U and B bands, and MS-PIRSs show more emission in V and I bands. The absolute magnitudes of MS-PIRSs (He-PIRSs) span a range $3 < M_V \lesssim -1$ ($4 \lesssim M_B \lesssim -4$). The brightest phase of MS PIRSs is at ages of Ia SNRs around $500 - 3000$ yr, suggesting that most historic nearby Ia SNRs are in this phase (see Table 6.1 and Table 6.2). Therefore, if these Galactic Ia SNRs originated from the SDS, PIRSs should be detectable.

6.3 Galactic type Ia SNRs

The Galactic SN rate (including Type I and Type II) is about $2.5^{+0.8}_{-0.5}$ SNe per century, and around 15% of them are SNe Ia (Tammann et al., 1994; Mannucci et al., 2005), suggesting that there should be more than $2,500$ (300) SNRs (Ia SNRs) in our Galaxy, if SNRs are recognizable for ages less than 10^5 yrs. However, only 312+ Galactic SNRs have been identified so far (Ferrand & Safi-Harb, 2012), and only five of them are known as Ia SNRs ($< 2\%$). Therefore, searching for a PIRS in the central region of a SNR could be an alternative indirect method to identify Ia SNRs from the current known SNRs. Table 6.1 shows a summary of the five current known Galactic SNe Ia: SN 185, SN 1006, SN 1572, SN 1604, and G1.9+0.3.

[1] `http://mesa.sourceforge.net`

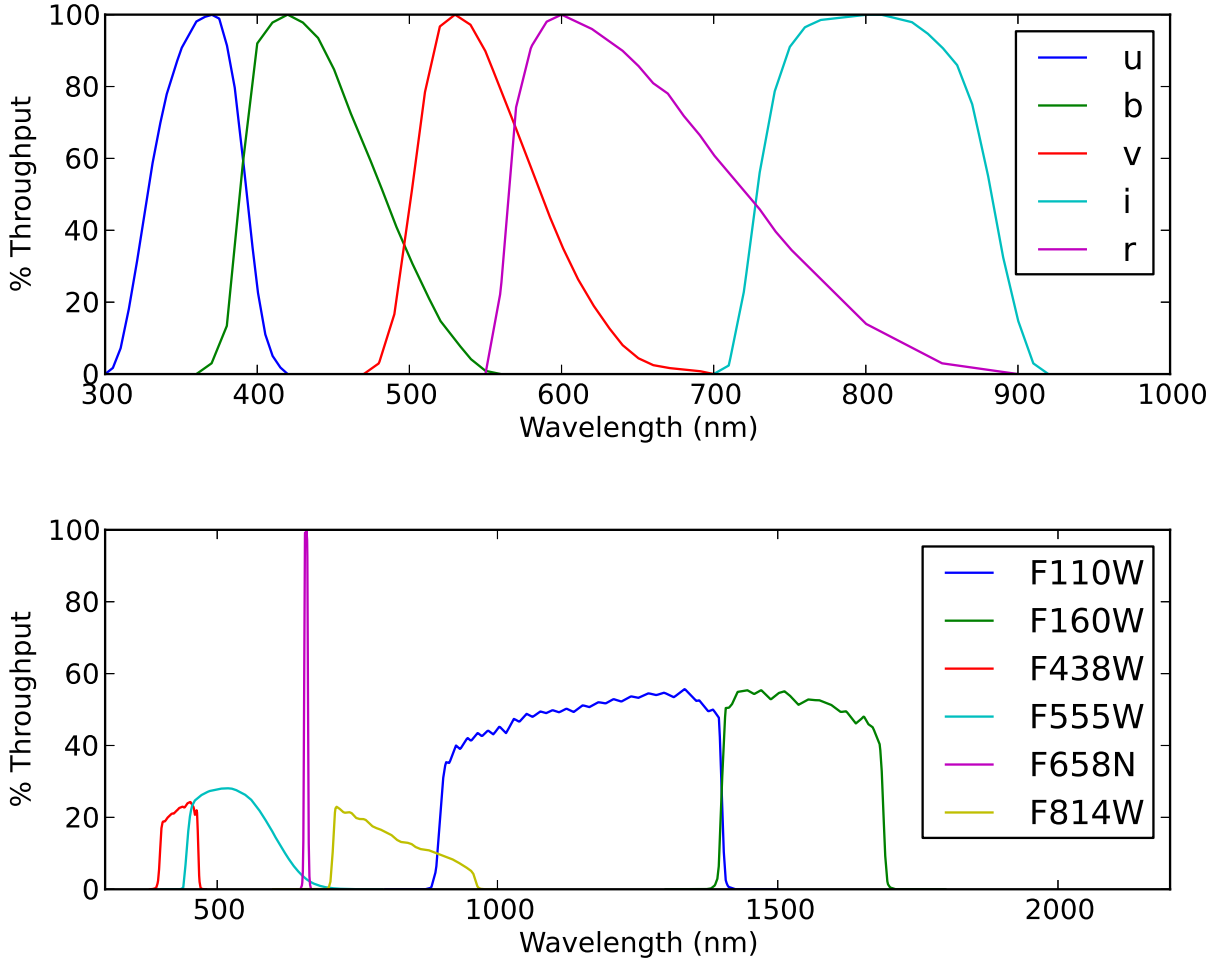

Figure 6.1: Sensitivity functions of different filters. The upper panel shows the UBVIR broadband filters in the Johnson-Cousins-Glass system. The lower panel represents the HST/WFC3 filters in F438W (B), F555W(V), F814(I), F110W(J), F160W(H), and F658N (H_α).

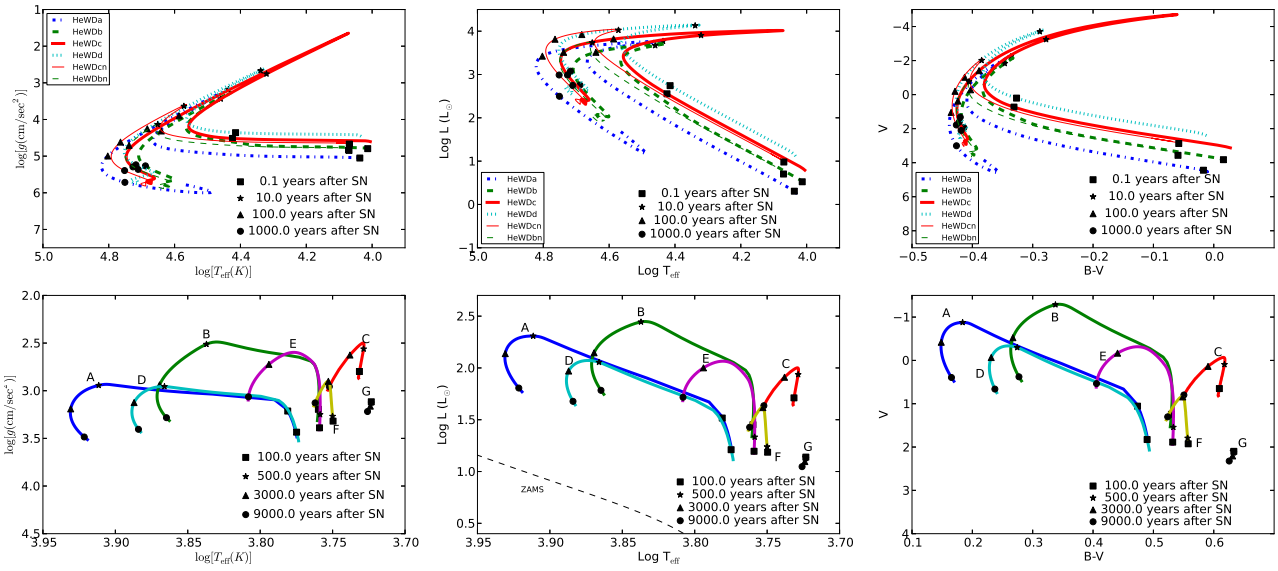

Figure 6.2: Evolutionary tracks in the Hertzsprung-Russell diagram for He- (upper panels) and MS- PIRSs (lower panels). The left column represent the H-R diagrams in effective temperature $T_{\rm eff}$ and surface gravity $\log(g)$ format; the middle and right columns show the same H-R diagrams but in effective temperature versus bolometric luminosity ($\log L$) and $B-V$ color versus V magnitude respectively.

6.3.1 SN 1572 (Tycho's SNR)

Although Tycho's SNR (SN 1572) has previously been suggested to be due to a subluminous SN Ia (van den Bergh, 1993), or an overluminous SN Ia (Ruiz-Lapuente, 2004), the most recent observation using the light echo suggests Tycho's SN was actually a normal SN Ia (Krause et al., 2008). The non-thermal X-ray arc inside Tycho's SNR could arise from the interaction between the SN ejecta and the loss of companion star's envelope in the impact of the explosion, giving support for the SDS as the progenitor of Tycho's SNR (Lu et al., 2011).

Ruiz-Lapuente et al. (2004) found a sub-giant, namely Tycho G, having an extraordinarily high radial speed $v \sin i \sim 108 \pm 6$ km s^{-1} that could come from the original orbital speed in the SDS, if Tycho G is a PIRS. Kerzendorf et al. (2012b) updated this radial velocity to $v \sin i \sim 79$ km s^{-1}, which is still abnormal. On the other hand, Ihara et al. (2007) show that the absence of an Fe I line at 372 nm in Tycho G disfavors it as a PIRS. Instead, Tycho E shows a strong Fe I absorption line, and its projected position is close to the center of Tycho's SNR, making it another PIRS candidate.

In the SDS, the non-degenerate companions are usually rapidly rotating due to tidal locking. However, Kerzendorf et al. (2009) found an upper limit for the rotational speed of Tycho G of 7.5 km s^{-1}, questioning Tycho G as a PIRS. Pan et al. (2012a) and Liu et al. (2013) studied the SN impact and post-impact conditions of MS-like binary companions and found that this problem can be solved because of the loss of

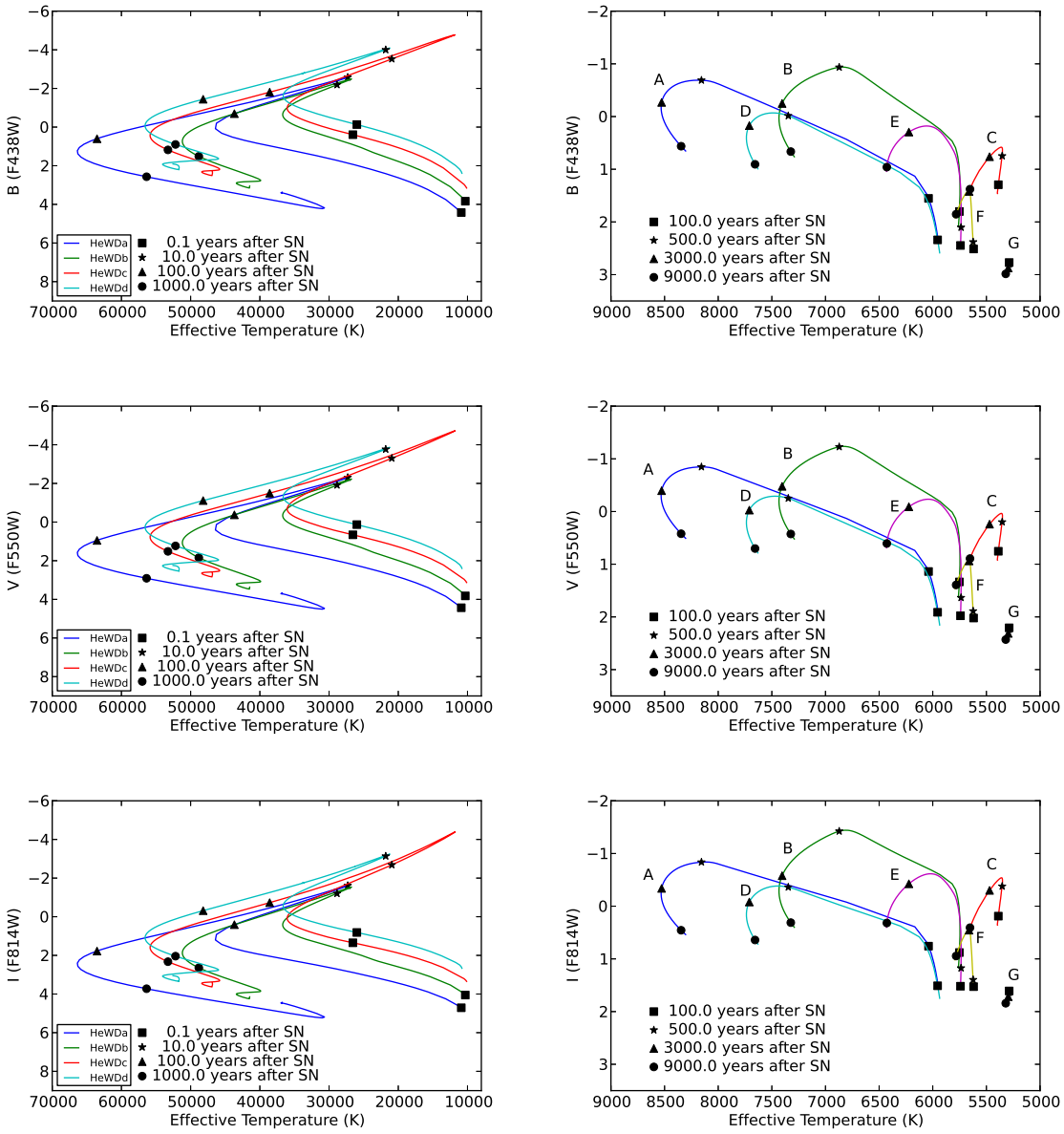

Figure 6.3: Evolutionary tracks in the H-R diagram for MS- and He- PIRSs in different HST/WFC3 bands.

Table 6.1: List of Galactic Type Ia SNRs

Name	Age (yrs)	Distance (kpc)	Radius (pc)	References
SN 185 (RCW 86)	1,828	~ 2.8	?	Ref a
SN 1006	1,007	2.2 ± 0.08	9.3	Ref b
SN 1572 (Tycho's)	441	2.8 ± 0.8	3.8	Ref c
SN 1604 (Kepler's)	409	6	3	Ref d
G1.9+0.3	$\lesssim 150$	~ 8.5	2	Ref e

[a] Westerlund (1969); Rosado et al. (1996)
[b] Winkler et al. (2003)
[c] Ruiz-Lapuente et al. (2004)
[e] Green et al. (2008); Reynolds et al. (2008); Carlton et al. (2011)

angular momentum during the SN impact and post-impact expansion. Therefore, further exploration of PIRS candidates in Tycho's SNR is necessary and crucial.

Figure 6.4 shows our predictions of post-impact conditions of MS-PIRSs compared with observations by González Hernández et al. (2009) and Kerzendorf et al. (2012b). In Pan et al. (2012a) we have shown that our model E has an effective temperature similar to that of Tycho G ($T_{\rm eff} = 6025$ K and $\log g = 4$ dex) but is about twice as bright. The recent observation of Tycho E gives an effective temperature $T_{\rm eff} = 5825$ K and surface gravity $\log g = 3.4$ dex, which is also consistent with our model E ($T_{\rm eff} = 5737$ K and $\log g = 3.3$ dex).

6.3.2 SN 1006

Two recent independent observations of SN 1006 by González Hernández et al. (2012) and Kerzendorf et al. (2012a) suggest that there is no surviving PIRS in the central region of SN 1006. However, we have noted that the stars B90474 ($\log g = 3.05 \pm 0.12$ cm s^{-2}, $T_{\rm eff} = 5051 \pm 38$ K) and B14707 ($\log g = 3.36 \pm 0.15$ cm s^{-2}, $T_{\rm eff} = 5065 \pm 47$ K) have surface gravities similar to our Model G ($\log g = 3.14$ dex, $T_{\rm eff} = 5288$ K) but have a lower effective temperature (see Figure 6.5). The problem is that B14707 lies much closer than the SNR and the distance uncertainty of B90474 is large.

In addition, the Schweizer-Middleditch star is a subdwarf OB (sdOB) star which is located at the center of SN 1006 and has strong Fe absorption lines (Schweizer & Middleditch, 1980; Burleigh et al., 2000). It is consistent with our He-PIRS models. However, the presence of redshifted absorption lines due to supernova ejecta suggests that it is more likely a background star (Wu et al., 1983; Burleigh et al., 2000).

6.3.3 SN 1604 (Kepler's SNR)

There is much evidence supporting the idea that SN 1604 (Kepler's SNR) exploded in the symbiotic channel (with an RG or AGB companion) in the SDS, such as strong circumstellar interaction and the bow shock

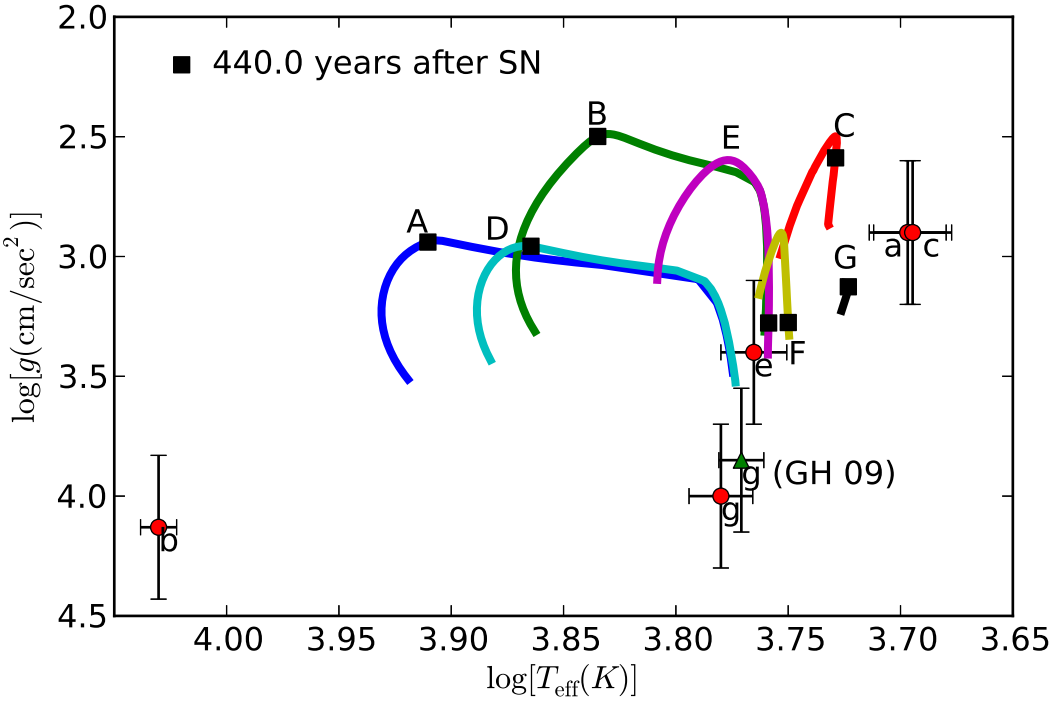

Figure 6.4: H-R diagram of PIRS candidates in SN 1572. Color lines indicate the simulated evolutionary tracks in our MS-PIRS models. Black squares represent the conditions at the age of SN 1572. The green triangle shows the condition of Tycho G from González Hernández et al. (2009), and red circles show the conditions of other PIRS candidates from Kerzendorf et al. (2012b).

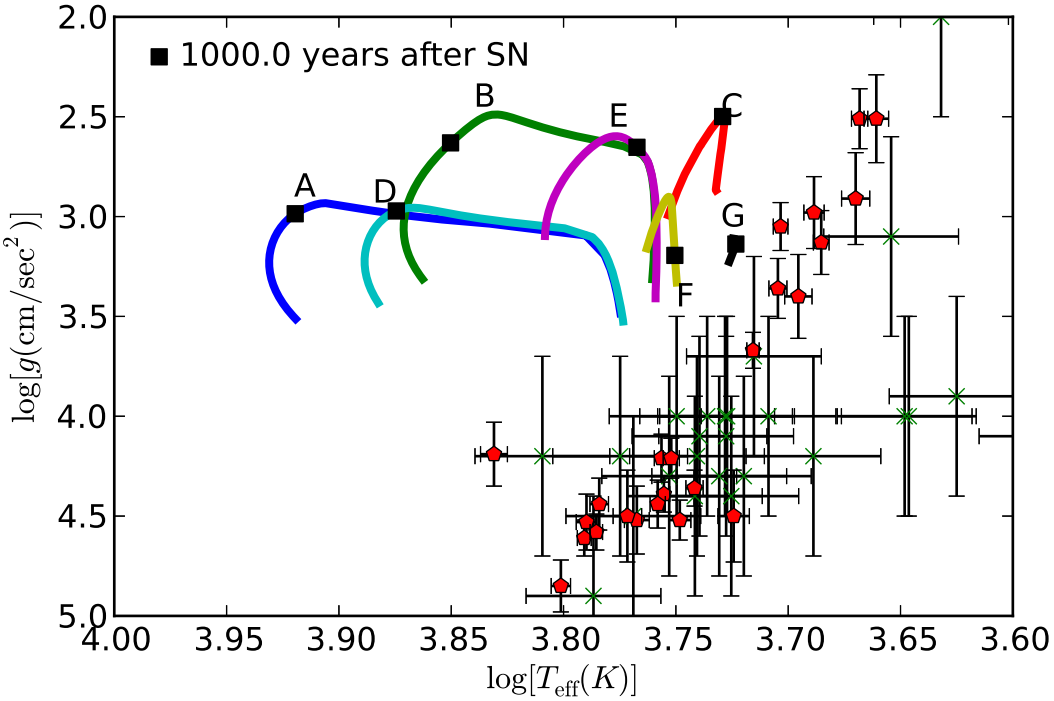

Figure 6.5: H-R diagram of PIRS candidates in SN 1006. Color lines indicate the simulated evolutionary tracks in our MS-PIRS models. Black squares represent the conditions at the age of SN 1006. Red pentagons show the observational data from González Hernández et al. (2012); green stars show the observational data from Kerzendorf et al. (2012a).

structure in the north. These structures are thought to originate from the motion of a mass-losing system through the interstellar medium prior to the SN (Patnaude et al., 2012; Burkey et al., 2013). However, observational searches for the PIRS in Kepler's SNR have not been undertaken.

Marietta et al. (2000) and Pan et al. (2012b) have shown that almost all the envelope of the RG in the RG-WD channel should be removed during the SN impact. Therefore, the PIRS in the RG-WD channel could be just a helium degenerate or non-degenerate core star with little hydrogen-rich envelope. However, a more detailed study of the evolution of RG-PIRSs using stellar evolution is necessary and will be considered in future work.

6.3.4 SN 185 (RCW 86)

SN 185 (also known as RCW 86) is the oldest known Galactic SN Ia. It was recently identified as a Ia SNR by Williams et al. (2011) and Yamaguchi et al. (2012), who estimate that the integrated Fe-K emission corresponds to a total Fe mass of about $1 M_{\odot}$. The derived ambient density (0.075 cm^{-3}) found by Yamaguchi et al. (2012) suggests an unusual low-density cavity surrounding the SNR. This can be explained by either a strong stellar wind from the progenitor itself, or the outflow from the nearby OB association discovered by Westerlund (1969). If SN 185 was a member of this group, the age of this group may place some constraints on the delay-time of this SN Ia. Figure 6.6 compares our He PIRS simulations with these OB stars. These OB stars have similar $B-V$ colors but are not subdwarfs (sdOB).

6.3.5 G1.9+0.3

G1.9+0.3 was discovered by Green & Gull (1984) about three decades ago but was only recently identified as a Ia SNR (Green et al., 2008). It is also the youngest Galactic SNR with an age of $\lesssim 150$ years (Green et al., 2008; Carlton et al., 2011). Its large distance (~ 8.5 kpc) and location near the Galactic center make it difficult to study and probably explain why there were no historic records of this SN. Its purely synchrotron radiation in X-ray makes G1.9+0.3 the fourth clear-cut X-ray-synchrotron-dominated Galactic SNR after SN 1006, G347.3-0.5, and G266.2-1.2 (Green et al., 2008). Its relatively young age makes it possible to detect the expansion speed ($\sim 14,000$ km s^{-1}) from its proper motion, making it possible to investigate the evolution of its SNR and its progenitor system.

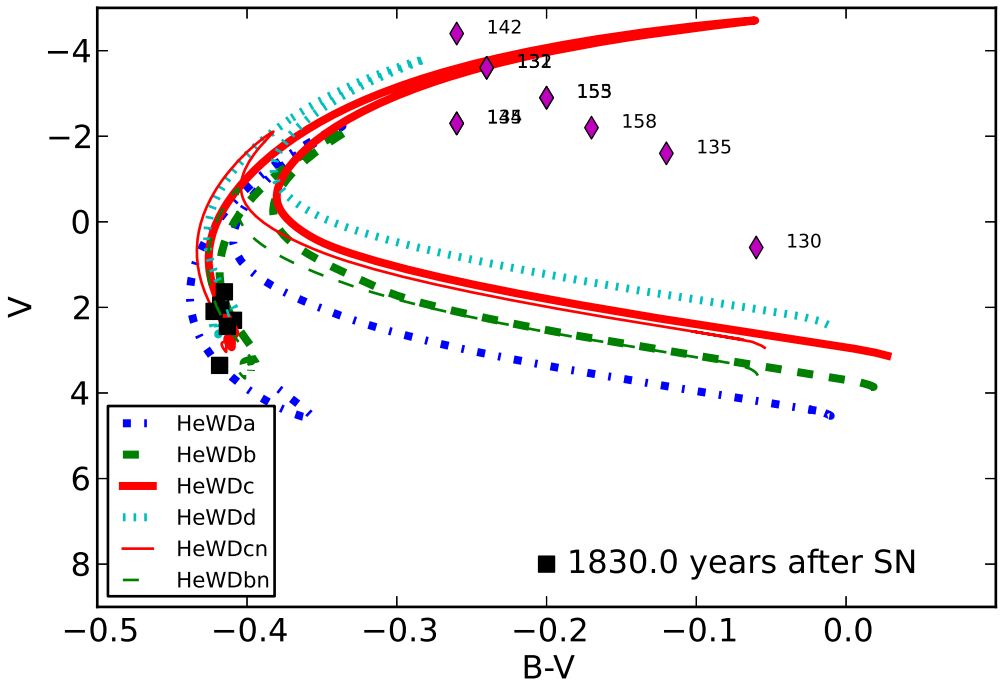

Figure 6.6: H-R diagram of PIRS candidates in SN 185. Color lines represent the evolutionary tracks of our He-PIRS simulations. Black squares indicate the condition of He PIRSs at the age of SN 185. Purple diamonds show a group of OB stars in the central region of SN 185 observed by Westerlund (1969).

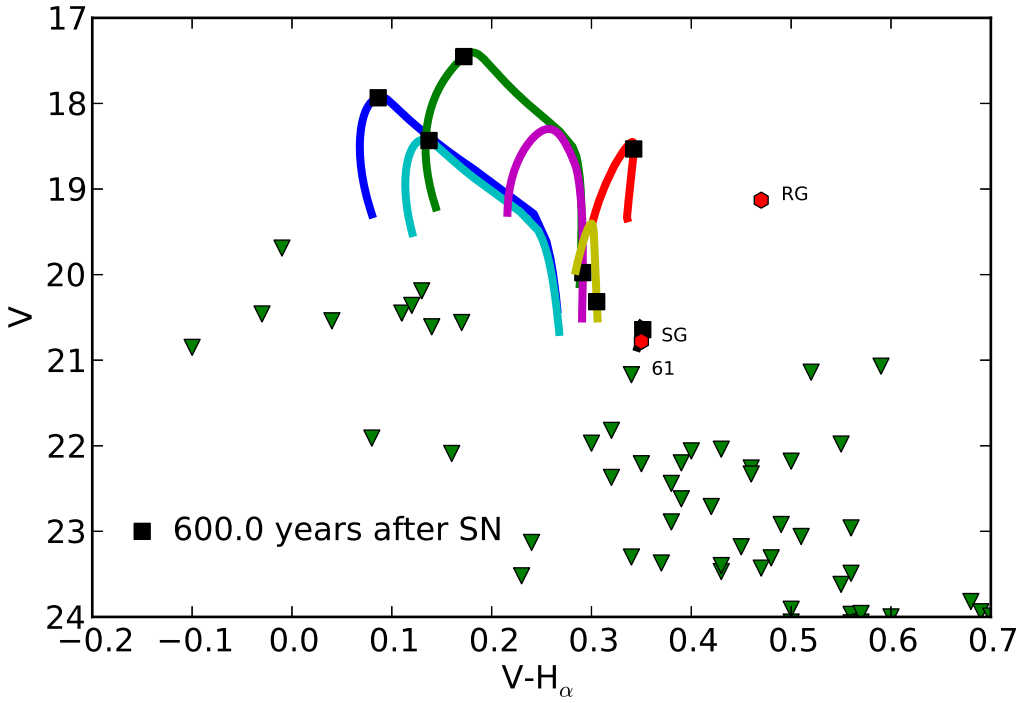

Figure 6.7: H-R diagram of PIRS candidates in SNR 0519-69.0. Color lines represent the evolutionary tracks of our MS-PIRS models. Black squares show the conditions of our models at the age of SNR 0519-69.0. Green triangles indicate the conditions of PIRS candidates observed by Edwards et al. (2012). Red circles are the sub giant and red giant closest to the geometric center of SNR 0519-69.0 as found by Edwards et al. (2012)

Table 6.2: List of Type Ia SNRs in LMC/SMC

Name	Age (yrs)	Distance (kpc)	Radius (pc)
B0509-67.5	400 ± 50	50 (LMC)	3.6
N103B	$1,000 - 2,000$	50 (LMC)	3.6
B0519-69.0	600 ± 200	50 (LMC)	3.9
DEM L71	$\sim 4,500$	50 (LMC)	8.6
B0548-70.4	$\sim 7,000$	50 (LMC)	12.5
DEM L316A	?	50 (LMC)	15
B0534-69.9	$\sim 10,000$	50 (LMC)	16
DEM L238	$10,000 - 15,000$	50 (LMC)	21
DEM L249	$10,000 - 15,000$	50 (LMC)	23
B0454-67.2	$\sim 30,000$	50 (LMC)	27
IKT 4	?	60 (SMC)	~ 12
IKT 5	?	60 (SMC)	15
IKT 25	?	60 (SMC)	18
DEM S128	?	60 (SMC)	26

* Fourteen Ia SNRs in the LMC and SMC (Vink, 2012).

6.4 Type Ia SNR in the Magellanic clouds

Ten Ia SNRs have been reported in the Large Magellanic Cloud (LMC) and four in the Small Magellanic Cloud (SMC; see Table 6.2). Since only five Galactic Ia SNRs have been identified, these fourteen Ia SNRs give a larger sample of Ia SNRs to search for PIRSs. In addition, the distances of Ia SNRs in the LMC and SMC are known more accurately than for Galactic Ia SNRs.

Edwards et al. (2012) studied the central sources within an error circle of 4.7" radius of the ~ 600 yr old Ia SNR 0519-69.0 using the HST F658N (H_α) and F550M(V) bands. They found 27 MS stars brighter than $m_V = 22.7$ magnitude. This result requires the progenitor of SNR 0519-69.0 to arise from either the DDS or the SDS with an M-dwarf companion. However, these observations only include the V and H_α images, where the H_α is a narrow filter that may confuse PIRS candidates with other line emission. Therefore, it is still worth studying this SNR in different broad bands, e.g. I or B. Edwards et al. (2012) also found a sub-giant star consistent with our model G star (the red line in Figure 6.7). However, this SG is close to the edge of the possible error circle, suggesting that this star may not be the PIRS of SNR 0519-69.0 unless the explosion was asymmetric.

Candidate PIRSs in another Ia SNR in LMC, SNR 0509-67.5, have been studied by Schaefer & Pagnotta (2012). SNR 0509-67.5 has an age of ~ 400 yrs. A search for PIRSs within a radius of 1.43", corresponding to a distance of 0.36 pc from the center of SNR 0509-67.5, shows that no star brighter than $M_V = 8.4$ is detected. However, a patch of diffuse emission at the center is seen in the continuum bands. The possibility that it is associated with the SNR cannot be excluded, although it may be a projected background galaxy.

Since only two Ia SNRs in the LMC have been searched for PIRSs, more PIRS searches in the LMC are

expected to show up in the near future for several reasons: (1) Ia SNRs in the LMC are at a known distance, 50 kpc, that is near enough to detect PIRSs with HST from our predictions. (2) LMC is a face-on galaxy that minimizes the confusion along the line of sight, and (3) the foreground Galactic extinction is low and the internal extinction of the LMC is modest.

In addition to the LMC, four Ia SNRs in the SMC also provide a good environment for searching for PIRSs (see Table 6.2). The SMC also has a known distance of 60 kpc and is close enough to search for PIRSs. It is believed to be a spiral galaxy that was disrupted by the LMC and then became an irregular galaxy. Therefore, the star formation history (SFH) and delay time distribution (DTD) in the SMC may be very different than those of the LMC and Milky Way. Furthermore, the extinction curve is also well studied in the SMC.

6.5 Other nearby galaxies

Besides the LMC and SMC, other nearby galaxies could be an additional environment for studying PIRSs, since the farther we look, the more SNRs we have. Furthermore, metallicities and SFH in other nearby galaxies are different from the Milky Way and Magellanic Clouds, which could affect pre-SN conditions, SN Ia explosions, and potentially also the post-impact evolution.

In Section 6.2, we have shown that our predicted MS-PIRSs (He PIRSs) spanned a range of absolute magnitude $3 < M_V \lesssim -1$ ($4 \lesssim M_B \lesssim -4$). By using HST/WFC3, the magnitude limit for point sources is ~ 27 with a one hour exposure, and ~ 29 for 10 hours' exposure, giving a maximum distance modulus of $24-28$ ($23-31$) for a one hour exposure. This corresponds to a maximum detectable distance of $0.6-4$ Mpc ($0.4-16$ Mpc) if there is no extinction.

However, the angular size of a SNR needs to be large enough to be detected in X-ray. Figure 6.8 shows the angular size of a young SNR in the free-expanding phase versus its distance for different ages. Assuming the ejecta speed $v_{\rm ej} = 10^4$ km sec^{-1} is a constant and the SNR is in the free-expanding phase for the first few thousand years, a minimum age of $\gtrsim 1,000$ yr is required for a clear detection by Chandra ($\theta_{\rm min} = 0.5$") and XMM-Newton ($\theta_{\rm min} = 14$"). Therefore, we predict that MS-PIRSs are detectable in extragalactic SNRs with ages $t_{\rm SNR} \gtrsim 1,000$ yr and distance $d_{\rm max} < 1.6$ Mpc.

In addition, He-PIRSs reach their maximum brightness at $10-30$ yrs after SN explosions and then fade within ~ 100 yrs (Pan et al., 2013). Their B magnitudes therefore are more likely less than 1 for historic Ia SNRs, giving a distance limit of $d_{\rm SN,max} \lesssim 0.4$ Mpc. However, the short timescale ($10-30$ yrs) of their luminous phase indicates a possibility to detect slow transitions of brightness at the locations of recent

nearby SNe Ia with $d_{\rm SN,max} < 16$ Mpc.

Nearby galaxies include NGC 6822, NGC 185, NGC 147, NGC 300, NGC 4124, M31, M32, M33, and M110. SNRs in M31 (Blair et al., 1981; Sasaki et al., 2012) , NGC 300 (Millar et al., 2012), and NGC 4214 (Dopita et al., 2010) have been studied recently. However, it is still unclear whether these SNRs are Ia SNRs or not. On the other hand, for recent nearby SNe Ia (e.g. SN 1885A, SN 1895B, SN 1937C, SN 1937E, and SN 1986G), we may not be able to resolve their SNRs, but the locations of these SNe Ia are well known, and we may be able to detect He PIRSs at those locations.

6.5.1 Andromeda Galaxy (M31)

More than 26 SNRs (including Type I and Type II) have been identified in the Andromeda Galaxy (M31 or NGC224) at 0.79 Mpc by Blair et al. (1981) and Sasaki et al. (2012). M31 has a distance modulus of 24.5, which makes it possible to detect all of our MS-PIRSs and most He PIRSs using HST/WFC3. The Panchromatic Hubble Andromeda Treasury (PHAT) multi-cycle program has observed about one third of M31 using HST. Its UVIS data reach a magnitude limit of 25 in F275W and F336W; ACS data reach maximum depths of 28 magnitudes in F475W and 27 magnitudes in F814W in the uncrowded outer disk. In these same regions, WFC3/IR data reach maximum depths of 26.5 and 25.5 in F110W and F160W, respectively.

Sasaki et al. (2012) have listed 26 X-ray SNRs and 20 X-ray SNR candidates in M31 based on their X-ray, optical, and radio emission, which is the most recent complete list of X-ray SNRs in M31. Therefore, using their list together with PHAT's data, it is possible to find PIRS candidates.

6.6 Conclusions

We have investigated the colors and magnitudes of seven MS- and four He-PIRSs based on our stellar evolution simulations (Pan et al., 2012a, 2013). Comparisons of predicted PIRSs with Galactic SN 1572 and SN 1006 are also presented. It is found that both Tycho E and Tycho G are consistent with our predicted MS PIRS Model E, although they are not perfect matches (Kerzendorf et al., 2012b). Furthermore, two sub-giants in the error circle of SN 1006 are also consistent with our MS PIRS Model G but have lower effective temperatures (González Hernández et al., 2012). In addition to Galactic Ia SNRs, a sub-giant in the SNR 0519-69.0 is also consistent with our Model G, but the projected position in the SNR is too far from the center (Edwards et al., 2012). However, at the current stage, only two Galactic Ia SNRs and two LMC Ia SNRs have been studied. Therefore, we encourage astronomers to further study PIRSs in other

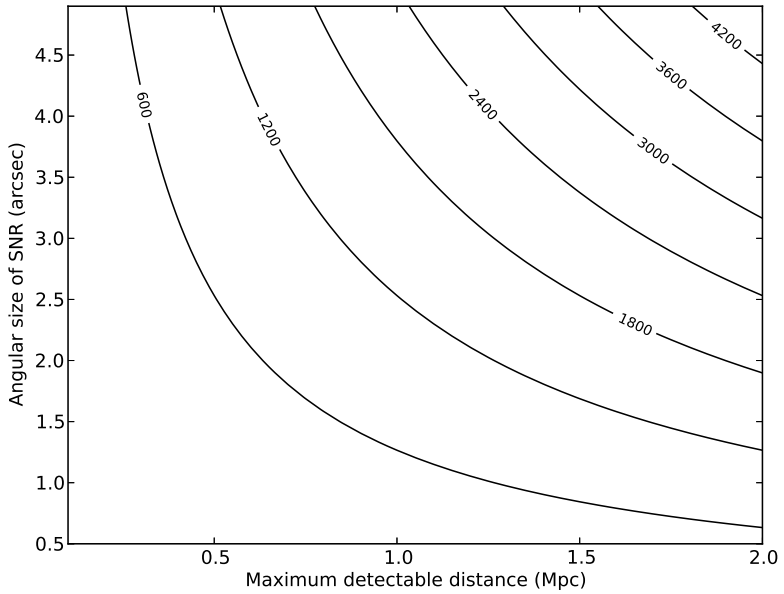

Figure 6.8: Angular size of a free expanding SNR versus its distance, assuming a constant ejecta speed $v_{\rm ej} = 10^9$ km s^{-1}. Different lines indicate the relationship between the angular size and distance for a given SNR age in years.

Galactic or nearby extragalactic Ia SNRs. Unlike Galactic Ia SNRs having large distance uncertainties, the distances of extragalactic Ia SNRs are relatively well known. We predict that the maximum detectable distance of MS PIRSs (He PIRSs) is $0.6 - 4$ Mpc ($0.4 - 16$ Mpc), if the apparent magnitude limit is 27 with no extinction, suggesting the LMC, SMC, and M31 are excellent environments in which to search for PIRSs.

Chapter 7

Conclusions

Examining the impact of supernova ejecta on the binary companions within the SDS provides quantitative and qualitative descriptions of the post-impact companions and subsequent evolution of Ia SNRs. In addition, investigating the evolution of post-impact remnant stars further provides observables to use in searching for the surviving PIRSs in Ia SNRs.

In this dissertation, we have first examined the impact of SN Ia ejecta on a companion star in the single-degenerate helium-star channel for the short-delay-time population of SN Ia via two-dimensional hydrodynamical simulations using a range of helium-star models and binary orbital separations. Although the general behavior of the temporal evolution is similar to that in previous studies by Marietta et al. (2000) and Pakmor et al. (2008) for MS and RG companions, the amount of matter unbound from the helium stars is less than for hydrogen-rich companions. Due to the shorter orbital periods of helium-star progenitor systems, the space motion of the companion star after the explosion is found to be higher. We find a power law relation between the unbound mass and initial binary separation that is consistent with the previous studies, suggesting that the power law behavior is not strongly sensitive to the nature of the companion. The kick velocity can also fitted by a power law, and we conclude that the power-law index may reflect the relative importance of the effect of ablation. An upper limit on the amount of nickel captured by the helium star is found to be $\sim 5 \times 10^{-4}\ M_{\odot}$. The ratio of nickel to helium abundance may be useful as a diagnostic of such events in future observational studies of SN Ia stellar remnants.

We then extended the study to three dimensions and considered multiple SDS progenitor channels including a MS star, a RG, and a He star, and considered the effects of asymmetry introduced by orbital motion and spin. A detailed setup of the sub-grid SN Ia explosion using the W7 model in Nomoto et al. (1984) also was described. It is found that the orbital motion and spin lead to $\sim 16\%$ more unbound mass in the MS star companion channel but do not significantly affect the kick velocity. Furthermore, the orbital motion and spin play an important role in determining the morphology of the SNR. A power law relation between the unbound mass and initial binary separation is found for all companion channels and is consistent with previous studies. Similarly, the kick velocity can be fitted by a power law for the MS and He star binary

companions. For the RG companion, we can only report a 40 km s^{-1} kick as an upper limit due to numerical uncertainty. By using passive particles, we find that the unbound mass is dominated by ablation instead of stripping. This result is in conflict with previous understanding, in which ablation was ignored in previous analytical studies. In addition, a hole shadowed by the ejecta is found to break the symmetry of the SNR. The amount of nickel contamination of the companion star is found to be $\sim 10^{-5} M_{\odot}$ for the MS star companion, $\sim 10^{-8} M_{\odot}$ for the RG companion, and $\sim 10^{-4} M_{\odot}$ for the He star companion. The corresponding nickel/iron to hydrogen plus helium abundance ratio may be useful for identifying the progenitor candidate in SN Ia remnants in future observations. We also find that the post-impact companion star loses about half of its initial angular momentum for the MS-WD scenario with the rotational velocity decreasing to 23% of its initial rotational velocity, providing added support for the SDS model for the Tycho SN.

In Chapter 4, we have investigated the post-impact evolution of remnant stars in the SDS for SNe Ia via stellar evolution calculations. We examined six possible binary companion models in the mass-orbital-period space from Hachisu et al. (2008b) and one companion model in Pan et al. (2012b), and we performed three-dimensional hydrodynamics simulations using the setup in Pan et al. (2012b). The post-impact evolution of the surviving stars was studied using the stellar evolution code MESA, together with the reconstructed hydrostatic remnant star models. It is found that the luminosity of post-impact remnant stars increases to $10 - 50 L_{\odot}$ after the supernova impact and increases to $\sim 100 L_{\odot}$ within a few thousand years, depending on the progenitor model. Due to the energy deposition from the SN ejecta, the envelope of the post-impact remnant expands on its local thermal timescale ($\sim 10^2 - 10^4$ yrs). After this expansion, stars start to contract and release gravitational energy. The post-impact evolution is directly affected by the explosion energy since it is related to the amount of unbound mass after the SN impact and the amount and depth of energy deposited in the remnant star. Among the calculated models, the companion E in our simulation (see Table 4.1), which has a mass $M = 1.44 M_{\odot}$, radius $R = 4.57 R_{\odot}$, effective temperature $T_{\rm eff} = 5,737$ K, and luminosity $L = 20.3 L_{\odot}$ at 440 years after the SN Ia explosion, is closest to the observed properties of Tycho G as determined by González Hernández et al. (2009). Although the fits are promising, the luminosity is twice as large as the value given by González Hernández et al. (2009). Finally, by comparing the observed radial velocity to the linear speed in our progenitor models, an inclination angle $\sin i \sim 0.4$ can be inferred. The surface rotational speed thus implied ($\sim 10 - 20$ km s^{-1}) approaches the low upper limit on the rotational speed of Tycho G found by Kerzendorf et al. (2009). Our results provide some support for Tycho G as a possible progenitor candidate in the SDS and point to the need for further detailed studies of the SDS binary evolutionary channel.

In Chapter 5, we investigated the post-impact evolution of He PIRSs within the SDS for SNe Ia via

numerical simulations. Four helium star models from Wang et al. (2009) are considered in our calculations. We performed three-dimensional hydrodynamics simulations using the methods that were described in Paper II. The post-impact evolution of these stars has been studied by reconstructing hydrostatic models based upon the final output in the hydrodynamics simulations and then interpolating them into a one-dimensional stellar evolution code, MESA. It is found that He PIRSs expand dramatically and evolve to become luminous OB stars within about $\sim 10-30$ years after the SN Ia explosion. This phase is short (< 100 years), and therefore these luminous OB stars are not likely to be detected in historical Ia SNRs. After ~ 30 years, He PIRSs contract and evolve into hot blue-subdwarf-like (sdO-like) stars due to the release of gravitational energy. Therefore, we predict that most He PIRSs should be sdO-like stars and could be detectable in nearby Ia SNRs.

We also predict that these He PIRSs should be rapidly rotating ($v_{\rm rot} \gtrsim 50$ km s^{-1}). Although a few fast rotating hot blue-subdwarfs have been observed recently (Geier et al., 2011, 2013), most single hot blue subdwarfs (sdOs and sdBs) are slowly rotating (Geier & Heber, 2012). If single hot blue subdwarfs originate from the merger of two He WDs (sdOs/sdBs; Heber, 2009), merger via a common envelope phase on the red giant branch (Politano et al., 2008), or the He-WD channel in SNe Ia (sdOs), the theoretical predictions cannot explain these observations, suggesting that other mechanisms operate to slow down the rotation, such as magnetic braking.

The He-WD binary channel is favored for the prompt DTD in the SDS and is expected to occur in star-forming regions. Since the orbital period immediately prior to the SN Ia explosion in the He-WD channel is extremely short ($\lesssim 1$ hour), the system is expected to be tidally locked. Thus, He stars should be rapidly rotating at the time of the SN Ia explosion. Although some angular momentum will be lost during the SN impact, He PIRSs are still expected to be rapidly rotating after ~ 30 years. The spatial velocity of He PIRSs is also expected to be high, reflecting the high orbital speed at the time of the SN Ia explosion and implying that He PIRSs could contribute to the HVS population (e.g. US 708).

Finally, we compared our PIRS predictions with known Galactic Ia SNRs and two Ia SNRs in the LMC. It is found that both Tycho E and Tycho G are consistent with our predicted MS PIRS Model E, although not perfectly matching (Kerzendorf et al., 2012b). Furthermore, two sub-giants in the error circle of SN 1006 are also consistent with our MS PIRS Model G, but have lower effective temperature (González Hernández et al., 2012). In addition to Galactic Ia SNRs, a sub-giant in the SNR 0519-69.0 is also consistent with our model G, but the projected position in the SNR is too far from the center (Edwards et al., 2012). However, at the current stage, only two Galactic Ia SNRs and two LMC Ia SNRs have been studied. Therefore, we encourage observers to further study PIRSs in other Galactic or nearby extragalactic Ia SNRs. Unlike

Galactic Ia SNRs having large distance uncertainties, the distances of extragalactic Ia SNRs are relatively well known. We predict that the maximum detectable distance of MS PIRSs (He PIRSs) is $0.6 - 4$ Mpc ($0.4 - 16$ Mpc), if the apparent magnitude limit is 27 and no extinction is assumed, suggesting the LMC, SMC, and M31 are excellent environments in which to search for PIRSs.

References

Anders, E. & Grevesse, N. 1989, Geochim. Cosmochim. Acta, 53, 197

Arnett, W. D. 1982, ApJ, 253, 785

Aubourg, É., Tojeiro, R., Jimenez, R., Heavens, A., Strauss, M. A., & Spergel, D. N. 2008, A&A, 492, 631

Baade, W. & Zwicky, F. 1934, Physical Review, 46, 76

Badenes, C. & Maoz, D. 2012, arXiv:1202.5472

Blair, W. P., Kirshner, R. P., & Chevalier, R. A. 1981, ApJ, 247, 879

Blondin, S., Kasen, D., Röpke, F. K., Kirshner, R. P., & Mandel, K. S. 2011, MNRAS, 417, 1280

Bloom, J. S., Kasen, D., Shen, K. J., Nugent, P. E., Butler, N. R., Graham, M. L., Howell, D. A., Kolb, U., Holmes, S., Haswell, C. A., Burwitz, V., Rodriguez, J., & Sullivan, M. 2012, ApJL, 744, L17

Branch, D. 1998, ARAA, 36, 17

Branch, D., Livio, M., Yungelson, L. R., Boffi, F. R., & Baron, E. 1995, PASP, 107, 1019

Branch, D. & Tammann, G. A. 1992, ARAA, 30, 359

Brandt, T. D., Tojeiro, R., Aubourg, É., Heavens, A., Jimenez, R., & Strauss, M. A. 2010, AJ, 140, 804

Brown, P. J., Dawson, K. S., Harris, D. W., Olmstead, M., Milne, P., & Roming, P. W. A. 2012, ApJ, 749, 18

Burkey, M. T., Reynolds, S. P., Borkowski, K. J., & Blondin, J. M. 2013, ApJ, 764, 63

Burleigh, M. R., Heber, U., O'Donoghue, D., & Barstow, M. A. 2000, A&A, 356, 585

Carlton, A. K., Borkowski, K. J., Reynolds, S. P., Hwang, U., Petre, R., Green, D. A., Krishnamurthy, K., & Willett, R. 2011, ApJL, 737, L22

Chomiuk, L., Soderberg, A. M., Moe, M., Chevalier, R. A., Rupen, M. P., Badenes, C., Margutti, R., Fransson, C., Fong, W.-f., & Dittmann, J. A. 2012, ApJ, 750, 164

Colella, P. & Glaz, H. M. 1985, Journal of Computational Physics, 59, 264

Colella, P. & Woodward, P. R. 1984, Journal of Computational Physics, 54, 174

Dessart, L., Burrows, A., Ott, C. D., Livne, E., Yoon, S.-C., & Langer, N. 2006, ApJ, 644, 1063

Dilday, B., Howell, D. A., Cenko, S. B., Silverman, J. M., Nugent, P. E., Sullivan, M., Ben-Ami, S., Bildsten, L., Bolte, M., Endl, M., Filippenko, A. V., Gnat, O., Horesh, A., Hsiao, E., Kasliwal, M. M., Kirkman, D., Maguire, K., Marcy, G. W., Moore, K., Pan, Y., Parrent, J. T., Podsiadlowski, P., Quimby, R. M., Sternberg, A., Suzuki, N., Tytler, D. R., Xu, D., Bloom, J. S., Gal-Yam, A., Hook, I. M., Kulkarni, S. R., Law, N. M., Ofek, E. O., Polishook, D., & Poznanski, D. 2012, Science, 337, 942

Domínguez, I., Höflich, P., & Straniero, O. 2001, ApJ, 557, 279

Dopita, M. A., Calzetti, D., Maíz Apellániz, J., Blair, W. P., Long, K. S., Mutchler, M., Whitmore, B. C., Bond, H. E., MacKenty, J., Balick, B., Carollo, M., Disney, M., Frogel, J. A., O'Connell, R., Hall, D., Holtzman, J. A., Kimble, R. A., McCarthy, P., Paresce, F., Saha, A., Walker, A. R., Silk, J., Sirianni, M., Trauger, J., Windhorst, R., & Young, E. 2010, Ap&SS, 330, 123

Dubey, A., Reid, L. B., & Fisher, R. 2008, Physica Scripta Volume T, 132, 014046

Dwarkadas, V. V. 2000, ApJ, 541, 418

Dwarkadas, V. V. & Chevalier, R. A. 1998, ApJ, 497, 807

Edwards, Z. I., Pagnotta, A., & Schaefer, B. E. 2012, ApJL, 747, L19

Eggleton, P. P. 1971, MNRAS, 151, 351

—. 1972, MNRAS, 156, 361

—. 1973, MNRAS, 163, 279

Eggleton, P. P. 1983, ApJ, 268, 368

Ferrand, G. & Safi-Harb, S. 2012, Advances in Space Research, 49, 1313

Filippenko, A. V. 1997, ARAA, 35, 309

Foley, R. J., Challis, P. J., Chornock, R., Ganeshalingam, M., Li, W., Marion, G. H., Morrell, N. I., Pignata, G., Stritzinger, M. D., Silverman, J. M., Wang, X., Anderson, J. P., Filippenko, A. V., Freedman, W. L., Hamuy, M., Jha, S. W., Kirshner, R. P., McCully, C., Persson, S. E., Phillips, M. M., Reichart, D. E., & Soderberg, A. M. 2012a, ArXiv:1212.2209

Foley, R. J., Simon, J. D., Burns, C. R., Gal-Yam, A., Hamuy, M., Kirshner, R. P., Morrell, N. I., Phillips, M. M., Shields, G. A., & Sternberg, A. 2012b, ApJ, 752, 101

Freedman, W. L., Madore, B. F., Scowcroft, V., Burns, C., Monson, A., Persson, S. E., Seibert, M., & Rigby, J. 2012, ApJ, 758, 24

Fryxell, B., Olson, K., Ricker, P., Timmes, F. X., Zingale, M., Lamb, D. Q., MacNeice, P., Rosner, R., Truran, J. W., & Tufo, H. 2000, ApJS, 131, 273

García-Senz, D., Badenes, C., & Serichol, N. 2012, ApJ, 745, 75

Geier, S., Classen, L., & Heber, U. 2011, ApJL, 733, L13

Geier, S. & Heber, U. 2012, A&A, 543, A149

Geier, S., Heber, U., Heuser, C., Classen, L., O'Toole, S. J., & Edelmann, H. 2013, ArXiv:1301.4129

Geier, S., Marsh, T. R., Dunlap, B. H., Barlow, B. N., Schaffenroth, V., Ziegerer, E., Heber, U., Kupfer, T., Maxted, P. F. L., Miszalski, B., Shporer, A., Telting, J. H., Oestensen, R. H., O'Toole, S. J., Gaensicke, B. T., & Napiwotzki, R. 2012, ArXiv:1209.4740

Geier, S., Nesslinger, S., Heber, U., Przybilla, N., Napiwotzki, R., & Kudritzki, R.-P. 2007, A&A, 464, 299

Goldhaber, G. et al. 2001, ApJ, 558, 359

González Hernández, J. I., Ruiz-Lapuente, P., Filippenko, A. V., Foley, R. J., Gal-Yam, A., & Simon, J. D. 2009, ApJ, 691, 1

González Hernández, J. I., Ruiz-Lapuente, P., Tabernero, H. M., Montes, D., Canal, R., Méndez, J., & Bedin, L. R. 2012, Nature, 489, 533

Green, D. A. & Gull, S. F. 1984, Nature, 312, 527

Green, D. A., Reynolds, S. P., Borkowski, K. J., Hwang, U., Harrus, I., & Petre, R. 2008, MNRAS, 387, L54

Hachisu, I., Kato, M., & Nomoto, K. 1996, ApJL, 470, L97

Hachisu, I., Kato, M., & Nomoto, K. 1999, ApJ, 522, 487

—. 2008a, ApJL, 683, L127

—. 2008b, ApJ, 679, 1390

Hachisu, I., Kato, M., Nomoto, K., & Umeda, H. 1999, ApJ, 519, 314

Hachisu, I., Kato, M., Saio, H., & Nomoto, K. 2012, ApJ, 744, 69

Hamuy, M., Phillips, M. M., Suntzeff, N. B., Schommer, R. A., Maza, J., Smith, R. C., Lira, P., & Aviles, R. 1996, AJ, 112, 2438

Han, Z. 2008, ApJL, 677, L109

Han, Z. & Podsiadlowski, P. 2003, in IAU Symposium, Vol. 214, High Energy Processes and Phenomena in Astrophysics, ed. X. D. Li, V. Trimble, & Z. R. Wang, 109

Han, Z. & Podsiadlowski, P. 2004, MNRAS, 350, 1301

Heber, U. 2009, ARAA, 47, 211

Hellemans, A. & Bunch, B. 1991, The Timetables of Science

Henyey, L. & L'Ecuyer, J. 1969, ApJ, 156, 549

Henyey, L., Vardya, M. S., & Bodenheimer, P. 1965, ApJ, 142, 841

Hillebrandt, W., Kromer, M., Röpke, F. K., & Ruiter, A. J. 2013, ArXiv e-prints

Hillebrandt, W. & Niemeyer, J. C. 2000, ARAA, 38, 191

Hills, J. G. 1988, Nature, 331, 687

Hinshaw, G., Larson, D., Komatsu, E., Spergel, D. N., Bennett, C. L., Dunkley, J., Nolta, M. R., Halpern, M., Hill, R. S., Odegard, N., Page, L., Smith, K. M., Weiland, J. L., Gold, B., Jarosik, N., Kogut, A., Limon, M., Meyer, S. S., Tucker, G. S., Wollack, E., & Wright, E. L. 2012, ArXiv e-prints

Hirsch, H. A., Heber, U., O'Toole, S. J., & Bresolin, F. 2005, A&A, 444, L61

Howell, D. A., Höflich, P., Wang, L., & Wheeler, J. C. 2001, ApJ, 556, 302

Howell, D. A., Sullivan, M., Conley, A., & Carlberg, R. 2007, ApJ, 667, L37

Howell, D. A., Sullivan, M., Nugent, P. E., Ellis, R. S., Conley, A. J., Le Borgne, D., Carlberg, R. G., Guy, J., Balam, D., Basa, S., Fouchez, D., Hook, I. M., Hsiao, E. Y., Neill, J. D., Pain, R., Perrett, K. M., & Pritchet, C. J. 2006, Nature, 443, 308

Hoyle, F. & Fowler, W. A. 1960, ApJ, 132, 565

Iben, Jr., I., Nomoto, K., Tornambe, A., & Tutukov, A. V. 1987, ApJ, 317, 717

Iben, Jr., I. & Tutukov, A. V. 1984, ApJS, 54, 335

Ihara, Y., Ozaki, J., Doi, M., Shigeyama, T., Kashikawa, N., Komiyama, K., & Hattori, T. 2007, PASJ, 59, 811

Ivanova, N. & Taam, R. E. 2004, ApJ, 601, 1058

Kasen, D. 2010, ApJ, 708, 1025

Kasen, D., Nugent, P., Thomas, R. C., & Wang, L. 2004, ApJ, 610, 876

Kato, M., Hachisu, I., Kiyota, S., & Saio, H. 2008, ApJ, 684, 1366

Kerzendorf, W. E., Schmidt, B. P., Asplund, M., Nomoto, K., Podsiadlowski, P., Frebel, A., Fesen, R. A., & Yong, D. 2009, ApJ, 701, 1665

Kerzendorf, W. E., Schmidt, B. P., Laird, J. B., Podsiadlowski, P., & Bessell, M. S. 2012a, ApJ, 759, 7

Kerzendorf, W. E., Yong, D., Schmidt, B. P., Simon, J. D., Jeffery, C. S., Anderson, J., Podsiadlowski, P., Gal-Yam, A., Silverman, J. M., Filippenko, A. V., Nomoto, K., Murphy, S. J., Bessell, M. S., Venn, K. A., & Foley, R. J. 2012b, ArXiv:1210.2713

Knop, R. A. et al. 2003, ApJ, 598, 102

Krause, O., Tanaka, M., Usuda, T., Hattori, T., Goto, M., Birkmann, S., & Nomoto, K. 2008, Nature, 456, 617

Leonard, D. C. 2007, ApJ, 670, 1275

Li, W., Bloom, J. S., Podsiadlowski, P., Miller, A. A., Cenko, S. B., Jha, S. W., Sullivan, M., Howell, D. A., Nugent, P. E., Butler, N. R., Ofek, E. O., Kasliwal, M. M., Richards, J. W., Stockton, A., Shih, H.-Y., Bildsten, L., Shara, M. M., Bibby, J., Filippenko, A. V., Ganeshalingam, M., Silverman, J. M., Kulkarni, S. R., Law, N. M., Poznanski, D., Quimby, R. M., McCully, C., Patel, B., Maguire, K., & Shen, K. J. 2011a, Nature, 480, 348

Li, W., Leaman, J., Chornock, R., Filippenko, A. V., Poznanski, D., Ganeshalingam, M., Wang, X., Modjaz, M., Jha, S., Foley, R. J., & Smith, N. 2011b, MNRAS, 412, 1441

Liu, Z.-W., Pakmor, R., Roepke, F. K., Edelmann, P., Hillebrandt, W., Kerzendorf, W. E., Wang, B., & Han, Z.-W. 2013, ArXiv e-prints

Liu, Z. W., Pakmor, R., Röpke, F. K., Edelmann, P., Wang, B., Kromer, M., Hillebrandt, W., & Han, Z. W. 2012, A&A, 548, A2

Livio, M. 2000, in Type Ia Supernovae, Theory and Cosmology, ed. J. C. Niemeyer & J. W. Truran, 33

Lu, F. J., Wang, Q. D., Ge, M. Y., Qu, J. L., Yang, X. J., Zheng, S. J., & Chen, Y. 2011, ApJ, 732, 11

Maeda, K., Benetti, S., Stritzinger, M., Röpke, F. K., Folatelli, G., Sollerman, J., Taubenberger, S., Nomoto, K., Leloudas, G., Hamuy, M., Tanaka, M., Mazzali, P. A., & Elias-Rosa, N. 2010, Nature, 466, 82

Mannucci, F. 2005, in Astronomical Society of the Pacific Conference Series, Vol. 342, 1604-2004: Supernovae as Cosmological Lighthouses, ed. M. Turatto, S. Benetti, L. Zampieri, & W. Shea, 140

Mannucci, F., Della Valle, M., & Panagia, N. 2006, MNRAS, 370, 773

Mannucci, F., Della Valle, M., Panagia, N., Cappellaro, E., Cresci, G., Maiolino, R., Petrosian, A., & Turatto, M. 2005, A&A, 433, 807

Maoz, D. 2008, MNRAS, 384, 267

Maoz, D. & Mannucci, F. 2011, ArXiv e-prints

Maoz, D., Mannucci, F., & Brandt, T. D. 2012, MNRAS, 426, 3282

Maoz, D., Mannucci, F., Li, W., Filippenko, A. V., Della Valle, M., & Panagia, N. 2011, MNRAS, 412, 1508

Marietta, E., Burrows, A., & Fryxell, B. 2000, ApJS, 128, 615

Mattila, S., Lundqvist, P., Sollerman, J., Kozma, C., Baron, E., Fransson, C., Leibundgut, B., & Nomoto, K. 2005, A&A, 443, 649

Maund, J. R., Höflich, P., Patat, F., Wheeler, J. C., Zelaya, P., Baade, D., Wang, L., Clocchiatti, A., & Quinn, J. 2010, ApJL, 725, L167

Maxted, P. F. L., Marsh, T. R., & North, R. C. 2000, MNRAS, 317, L41

Meng, X., Chen, X., & Han, Z. 2007, PASJ, 59, 835

—. 2009, MNRAS, 395, 2103

Meng, X. & Yang, W. 2010, ApJ, 710, 1310

—. 2011, Science in China G: Physics and Astronomy, 54, 2296

Mereghetti, S., Tiengo, A., Esposito, P., La Palombara, N., Israel, G. L., & Stella, L. 2009, Science, 325, 1222

Millar, W. C., White, G. L., & Filipovic, M. D. 2012, Serbian Astronomical Journal, 184, 19

Minkowski, R. 1941, PASP, 53, 224

Napiwotzki, R. et al. 2001, Astronomische Nachrichten, 322, 411

—. 2002, A&A, 386, 957

Nelemans, G., Yungelson, L. R., Zwart, S. F. P., & Verbunt, F. 2001, A&A, 365, 491

Nomoto, K. 1982, ApJ, 257, 780

Nomoto, K. & Iben, Jr., I. 1985, ApJ, 297, 531

Nomoto, K., Thielemann, F.-K., & Yokoi, K. 1984, ApJ, 286, 644

Nugent, P. E., Sullivan, M., Cenko, S. B., Thomas, R. C., Kasen, D., Howell, D. A., Bersier, D., Bloom, J. S., Kulkarni, S. R., Kandrashoff, M. T., Filippenko, A. V., Silverman, J. M., Marcy, G. W., Howard, A. W., Isaacson, H. T., Maguire, K., Suzuki, N., Tarlton, J. E., Pan, Y.-C., Bildsten, L., Fulton, B. J., Parrent, J. T., Sand, D., Podsiadlowski, P., Bianco, F. B., Dilday, B., Graham, M. L., Lyman, J., James, P., Kasliwal, M. M., Law, N. M., Quimby, R. M., Hook, I. M., Walker, E. S., Mazzali, P., Pian, E., Ofek, E. O., Gal-Yam, A., & Poznanski, D. 2011, Nature, 480, 344

Pakmor, R., Röpke, F. K., Weiss, A., & Hillebrandt, W. 2008, A&A, 489, 943

Pan, K.-C., Ricker, P., & Taam, R. 2013, ArXiv e-prints

Pan, K.-C., Ricker, P. M., & Taam, R. E. 2010, ApJ, 715, 78

—. 2012a, ApJ, 760, 21

—. 2012b, ApJ, 750, 151

Patnaude, D. J., Badenes, C., Park, S., & Laming, J. M. 2012, ApJ, 756, 6

Paxton, B., Bildsten, L., Dotter, A., Herwig, F., Lesaffre, P., & Timmes, F. 2011, ApJS, 192, 3

Paxton, B., Cantiello, M., Arras, P., Bildsten, L., Brown, E. F., Dotter, A., Mankovich, C., Montgomery, M. H., Stello, D., Timmes, F. X., & Townsend, R. 2013, ArXiv:1301.0319

Perlmutter, S., Aldering, G., Goldhaber, G., Knop, R. A., Nugent, P., Castro, P. G., Deustua, S., Fabbro, S., Goobar, A., Groom, D. E., Hook, I. M., Kim, A. G., Kim, M. Y., Lee, J. C., Nunes, N. J., Pain, R., Pennypacker, C. R., Quimby, R., Lidman, C., Ellis, R. S., Irwin, M., McMahon, R. G., Ruiz-Lapuente, P., Walton, N., Schaefer, B., Boyle, B. J., Filippenko, A. V., Matheson, T., Fruchter, A. S., Panagia, N., Newberg, H. J. M., Couch, W. J., & The Supernova Cosmology Project. 1999, ApJ, 517, 565

Perlmutter, S., Gabi, S., Goldhaber, G., Goobar, A., Groom, D. E., Hook, I. M., Kim, A. G., Kim, M. Y., Lee, J. C., Pain, R., Pennypacker, C. R., Small, I. A., Ellis, R. S., McMahon, R. G., Boyle, B. J., Bunclark, P. S., Carter, D., Irwin, M. J., Glazebrook, K., Newberg, H. J. M., Filippenko, A. V., Matheson, T., Dopita, M., Couch, W. J., & Supernova Cosmology Project. 1997, ApJ, 483, 565

Phillips, M. M. 1993, ApJL, 413, L105

Planck Collaboration, Ade, P. A. R., Aghanim, N., Armitage-Caplan, C., Arnaud, M., Ashdown, M., Atrio-Barandela, F., Aumont, J., Baccigalupi, C., Banday, A. J., & et al. 2013, ArXiv e-prints

Podsiadlowski, P. 2003, ArXiv:0303.660

Politano, M., Taam, R. E., van der Sluys, M., & Willems, B. 2008, ApJL, 687, L99

Pritchet, C. J., Howell, D. A., & Sullivan, M. 2008, ApJL, 683, L25

Reynolds, S. P., Borkowski, K. J., Green, D. A., Hwang, U., Harrus, I., & Petre, R. 2008, ApJL, 680, L41

Ricker, P. M. 2008, ApJS, 176, 293

Ricker, P. M. & Taam, R. E. 2008, ApJL, 672, L41

Riess, A. G. 1996, Ph.D. thesis, Harvard University

Riess, A. G., Filippenko, A. V., Challis, P., Clocchiatti, A., Diercks, A., Garnavich, P. M., Gilliland, R. L., Hogan, C. J., Jha, S., Kirshner, R. P., Leibundgut, B., Phillips, M. M., Reiss, D., Schmidt, B. P., Schommer, R. A., Smith, R. C., Spyromilio, J., Stubbs, C., Suntzeff, N. B., & Tonry, J. 1998, AJ, 116, 1009

Riess, A. G., Macri, L., Casertano, S., Lampeitl, H., Ferguson, H. C., Filippenko, A. V., Jha, S. W., Li, W., & Chornock, R. 2011, ApJ, 730, 119

Riess, A. G., Press, W. H., & Kirshner, R. P. 1996, ApJ, 473, 88

Rosado, M., Ambrocio-Cruz, P., Le Coarer, E., & Marcelin, M. 1996, A&A, 315, 243

Ruiter, A. J., Belczynski, K., & Fryer, C. 2009, ApJ, 699, 2026

Ruiz-Lapuente, P. 2004, ApJ, 612, 357

—. 2012, Nature, 481, 149

Ruiz-Lapuente, P., Comeron, F., Méndez, J., Canal, R., Smartt, S. J., Filippenko, A. V., Kurucz, R. L., Chornock, R., Foley, R. J., Stanishev, V., & Ibata, R. 2004, Nature, 431, 1069

Sasaki, M., Pietsch, W., Haberl, F., Hatzidimitriou, D., Stiele, H., Williams, B., Kong, A., & Kolb, U. 2012, A&A, 544, A144

Scannapieco, E. & Bildsten, L. 2005, ApJL, 629, L85

Schaefer, B. E. & Pagnotta, A. 2012, Nature, 481, 164

Schmidt, B. P., Suntzeff, N. B., Phillips, M. M., Schommer, R. A., Clocchiatti, A., Kirshner, R. P., Garnavich, P., Challis, P., Leibundgut, B., Spyromilio, J., Riess, A. G., Filippenko, A. V., Hamuy, M., Smith, R. C., Hogan, C., Stubbs, C., Diercks, A., Reiss, D., Gilliland, R., Tonry, J., Maza, J., Dressler, A., Walsh, J., & Ciardullo, R. 1998, ApJ, 507, 46

Schweizer, F. & Middleditch, J. 1980, ApJ, 241, 1039

Shappee, B. J., Kochanek, C. S., & Stanek, K. Z. 2012, ArXiv:1205.5028

—. 2013a, ApJ, 765, 150

Shappee, B. J., Stanek, K. Z., Pogge, R. W., & Garnavich, P. M. 2013b, ApJL, 762, L5

Sternberg, A., Gal-Yam, A., Simon, J. D., Leonard, D. C., Quimby, R. M., Phillips, M. M., Morrell, N., Thompson, I. B., Ivans, I., Marshall, J. L., Filippenko, A. V., Marcy, G. W., Bloom, J. S., Patat, F., Foley, R. J., Yong, D., Penprase, B. E., Beeler, D. J., Allende Prieto, C., & Stringfellow, G. S. 2011, Science, 333, 856

Tammann, G. A., Loeffler, W., & Schroeder, A. 1994, ApJS, 92, 487

Timmes, F. X. & Swesty, F. D. 2000, ApJS, 126, 501

Truran, J. W., Arnett, W. D., & Cameron, A. G. W. 1967, Canadian Journal of Physics, 45, 2315

van den Bergh, S. 1993, ApJ, 413, 67

Vennes, S., Kawka, A., O'Toole, S. J., Németh, P., & Burton, D. 2012, ApJL, 759, L25

Vink, J. 2012, , 20, 49

Waldman, R., Yungelson, L. R., & Barkat, Z. 2008, in Astronomical Society of the Pacific Conference Series, Vol. 391, Hydrogen-Deficient Stars, ed. A. Werner & T. Rauch, 359

Wang, B., Chen, X., Meng, X., & Han, Z. 2009, ApJ, 701, 1540

Wang, B. & Han, Z. 2009, A&A, 508, L27

Wang, B. & Han, Z. 2009, Ap&SS, 254

Wang, B. & Han, Z. 2010a, MNRAS, 404, L84

—. 2010b, A&A, 515, A88

—. 2010c, Ap&SS, 329, 293

—. 2012, New Astron. Rev., 56, 122

Wang, B., Justham, S., & Han, Z. 2013, ArXiv:1301.1047

Wang, B., Li, X.-D., & Han, Z.-W. 2010, MNRAS, 401, 2729

Wang, B., Meng, X., Chen, X., & Han, Z. 2009, MNRAS, 395, 847

Wang, L. & Wheeler, J. C. 2008, ARAA, 46, 433

Webbink, R. F. 1984, ApJ, 277, 355

Westerlund, B. E. 1969, AJ, 74, 879

Wheeler, J. C. 2012, ApJ, 758, 123

Wheeler, J. C. & Harkness, R. P. 1990, Reports on Progress in Physics, 53, 1467

Whelan, J. & Iben, Jr., I. 1973, ApJ, 186, 1007

Wickramasinghe, D. T., Hurley, J. R., Ferrario, L., Tout, C. A., & Kiel, P. D. 2009, Journal of Physics Conference Series, 172, 012037

Williams, B. J., Blair, W. P., Blondin, J. M., Borkowski, K. J., Ghavamian, P., Long, K. S., Raymond, J. C., Reynolds, S. P., Rho, J., & Winkler, P. F. 2011, ApJ, 741, 96

Wilson, O. C. 1939, ApJ, 90, 634

Winkler, P. F., Gupta, G., & Long, K. S. 2003, ApJ, 585, 324

Wu, C.-C., Leventhal, M., Sarazin, C. L., & Gull, T. R. 1983, ApJL, 269, L5

Yamaguchi, H., Koyama, K., & Uchida, H. 2012, ArXiv e-prints

Yu, Q. & Tremaine, S. 2003, ApJ, 599, 1129

Zahn, J.-P. 1977, A&A, 57, 383

Zwicky, F. 1938, ApJ, 88, 522

—. 1939, Physical Review, 55, 726